Plasma Sources in Planetary Magnetospheres: Mercury

J.M. Raines(1), *G.A. DiBraccio*(1,2), *T.A. Cassidy*(3), *D.C. Delcourt*(4), *M. Fujimoto*(5), *X. Jia(1), V. Mangano*(6), *A. Milillo*(6), *M. Sarantos*(7), *J.A. Slavin(1), P. Wurz*(8)

(1) Department of Atmospheric, Oceanic and Space Sciences, University of Michigan, Ann Arbor, MI, 48109, USA.
(2) Solar System Exploration Divison, NASA Goddard Space Flight Center, Greenbelt, MD, 20771, USA.
(3) Laboratory for Atmospheric and Space Physics, University of Colorado, Boulder, CO, 80303, USA.
(4) LPP, Ecole Polytechnique-CNRS, Université Pierre et Marie Curie, 4 Place Jussieu, 75252 Paris, France.
(5) ISAS, Kanagawa, Japan
(6) Institute of Space Astrophysics and Planetology, INAF, Rome, Italy.
(7) Heliophysics Science Division, NASA Goddard Space Flight Center, Greenbelt, MD, USA.
(8) Physics Institute, University of Bern, CH-3012 Bern, Switzerland.

1 Introduction

The proximity of Mercury to the Sun makes this planet a particularly interesting subject because of the extreme environmental conditions that led to its unique evolutionary history. Mercury's present plasma environment has its foundation in a weak intrinsic global magnetic field that supports a small, but dynamic, magnetosphere. The plasma in Mercury's space environment coexists with the planet's exosphere and strongly interacts with the surface. In fact, Mercury's environment is a complex and tightly coupled system where the magnetosphere, exosphere, and surface are linked by interaction processes that facilitate material production and energy exchange [*Killen and Ip*, 1999; *Killen et al.*, 2007; *Milillo et al.*, 2010]. Investigations regarding the coupling of Mercury's magnetosphere with the interplanetary magnetic field (IMF) of the Sun, as well as the planet's interaction with solar radiation (both electromagnetic and particle) and with interplanetary dust, can provide important clues to the process of planetary evolution [*Orsini et al.*, 2014]. The study of Mercury may reveal processes fundamental to the interpretation of exoplanet observations: In fact, many discovered exoplanets are located only a few stellar radii away from their parent star, even closer than Mercury is to the Sun. The resulting effects and type of interactions in these particular situations are among the key questions to be answered in the future.

The first in situ measurements provided by three flybys of Mariner 10 [*Vilas et al.*, 1988] in 1974–1975 revealed the weak, intrinsic magnetic field of Mercury that gives rise to its small magnetosphere [for a review, see *Russell et al.*, 1988; *Wurz and Blomberg*, 2001; *Slavin et al.*, 2007]. Plasma sheet electrons were measured during the first flyby, though no ion measurements were made due to a hardware failure

[*Ogilvie et al.*, 1974]. After those measurements, the scientific community had to wait almost 40 years until MErcury Surface, Space ENvironment, GEochemistry, and Ranging (MESSENGER) was launched in August 2004 [*Solomon et al.*, 2007] and became the first spacecraft to obtain systematic measurements by orbiting Mercury. The MESSENGER magnetic field measurements indicate that Mercury's magnetic dipole moment is offset northward from the planet's center by 0.2 R_M (where R_M is Mercury's radius, or 2440 km) [*Alexeev et al.*, 2010; *Anderson et al.*, 2011]. Now we know that Mercury's magnetosphere is highly dynamic [e.g., *Slavin et al.*, 2009, 2010; *DiBraccio et al.*, 2013], so it cannot be considered as a stable structure where plasma distributes according to well-characterized populations, like in the Earth's magnetosphere. At Mercury, no stable ring current is observed and magnetic storms driven by adiabatic convection cannot develop. On the contrary, fast (few seconds) events like Flux Transfer Events (FTEs) [*Slavin et al.*, 2012b], dipolarizations [*Sundberg et al.*, 2012], plasmoids [*Slavin et al.*, 2012a; *DiBraccio et al.*, 2014] are observed. Further, bursts of low- and moderate energy (tens to hundreds keV) electrons [*Ho et al.*, 2012] are often recorded.

Together with the protons and He^{2+} of solar wind origin, MESSENGER's Fast Imaging Plasma Spectrometer (FIPS) detected ions of planetary origin like He^+, Na^+-Mg^+ and several other heavy ion species [*Zurbuchen et al.*, 2008] while Mercury Atmospheric and Surface Composition Spectrometer (MASCS) UltraViolet and Visible Spectrometer (UVVS) [*McClintock et al.,* 2007] mapped the Ca^+ tail on the nightside [*Vervack et al.*, 2010]. In particular, on the dayside, a solar wind-originating plasma population mixed with heavy planetary ions (Na^+ group) was observed in the region of the magnetospheric cusp. On the nightside, plasma ions were observed near the equator, in the central plasma sheet [*Raines et al.*, 2013]. Finally, increased plasma fluxes were observed in the magnetosheath as well as sparsely distributed planetary ions that span the magnetopause boundary (as identified in magnetic field measurements [*Anderson et al.*, 2012; *Winslow et al.*, 2013]). These features are observed on nearly every orbit, despite highly variable solar wind and IMF conditions [*Gershman et al.*, 2012; *Baker et al.*, 2013].

The solar wind and planetary ions interact with the surface to produce ion sputtering, backscattering, and internal structure alteration via chemical sputtering and/or enhanced diffusion [*Mura et al.*, 2009; *Sarantos et al.*, 2009]. The surface-released material populates the neutral gas environment of Mercury as a tenuous and non-collisional regime, constituting the exosphere.

The presence of neutral atoms in Mercury's environment was also discovered during the Mariner 10 flybys; H, He, and O were detected in the atmosphere by the onboard UV spectrometer [*Broadfoot et al.*, 1974]. Later, Na, K, and Ca were detected through ground-based Earth observations [*Potter and Morgan*, 1985, 1986; *Bida et al.*, 2000]. *Doressoundiram et al.* [2009] defined an upper limit for Al, Fe, and Si by ground-based observations. Finally, MESSENGER UVVS provided a systematic in situ detection of Na, Ca and Mg [*McClintock et al.*, 2009; *Domingue et al.*, 2007]. New ground-based observations and new methods and technologies [e.g., *Leblanc et al.*, 2008; *Mangano et al.*, 2013], coupled with simulations [e.g., *Schmidt*, 2013] permit the investigation of spatial and temporal variations in the exosphere, providing insight to magnetospheric and solar activity variation dependencies. UVVS measurements, surprisingly, have shown little exospheric response to magnetospheric activity.

The most globally and systematically observed element at Mercury is Na, since its doublet is relatively easy to detect through the Earth's atmosphere and its

abundance is high in Mercury's exosphere. A clear relation of Na distribution and its variability has been observed throughout the exosphere. The Na exosphere peaks frequently at mid-latitudes in the dayside, corresponding to the magnetic cusp regions where solar wind plasma is able to access the planetary surface [e.g., *Killen et al.*, 2001]. Nevertheless, experimental results exclude that the yield of direct sputtering can account for the observed Na intensity [*McGrath et al.*, 1986; *Johnson and Baragiola*, 1991]. Modeling and recent Na temperature obtained by MESSENGER show that Photon Stimulated Desorption (PSD) is by far the most efficient process to release Na into the exosphere on the day side of Mercury [*Wurz et al.*, 2010; *Mura et al.*, 2009; *Cassidy et al.*, 2015; *Sarantos et al.*, 2009], indicating that the processes are independent from each other [*Leblanc et al.*, 2010; *Mura et al.*, 2009]. Also, the measurements by MESSENGER UVVS have shown evidence that variation of global intensity are well reproduced year by year [*Cassidy et al.*, 2015], showing that solar wind action could account only for variation in the distribution, not in the global exosphere density..

Mercury's exosphere is continuously emptied and filled through a variety of chemical and physical processes acting on the planet's surface and environment [*Killen et al., 2007; Leblanc et al.*, 2007]. The neutral environment of the planet is not only generated by plasma-surface interactions, but it also interacts with the circulating plasma via charge exchange, and it also undergoes electron-impact and photo-ionization, creating a population of low-energy ions. These newly generated ions are accelerated [*Delcourt et al.*, 2003; *Seki et al.*, 2013] and contribute to the mini-magnetosphere. At a further step, the ions are either lost into the solar wind or impact again onto the surface.

Finally, we can conclude that the sources of the magnetospheric ions are mostly solar wind plasma entering the magnetosphere, ionization of exospheric species, and planetary ions from the surface. On the other hand, sinks of the ion populations are the surface, where plasma directly impacts, and the solar wind, that picks up ions as it flows past the planet. To evaluate the source and sink balance in the Mercury environment, this global complex system should be investigated as a whole.

The forthcoming ESA - JAXA BepiColombo mission to Mercury (to be launched in 2016) [*Benkhoff et al.*, 2010], consists of two Mercury-orbiting spacecraft to provide the opportunity for simultaneous two-point measurements. Thanks to this, the BepiColombo mission will offer an unprecedented opportunity to deeply investigate magnetospheric and exospheric dynamics at Mercury as well as their interactions with solar radiation and interplanetary dust [*Milillo et al.*, 2010].

In the following sections of this chapter, the structure and dynamics of Mercury's magnetosphere are reviewed, with an emphasis on its local plasma environment. We examine both global and kinetic features that have been identified through magnetic field and plasma observations, organized into plasma sources and losses, as well as the exosphere and the surface processes that generate it. Finally, we discuss the contribution that modeling has made to our understanding of Mercury's magnetosphere and of the behavior of its plasma populations.

2 Magnetospheric Structure and Dynamics

2.1 Global Magnetosphere Configuration

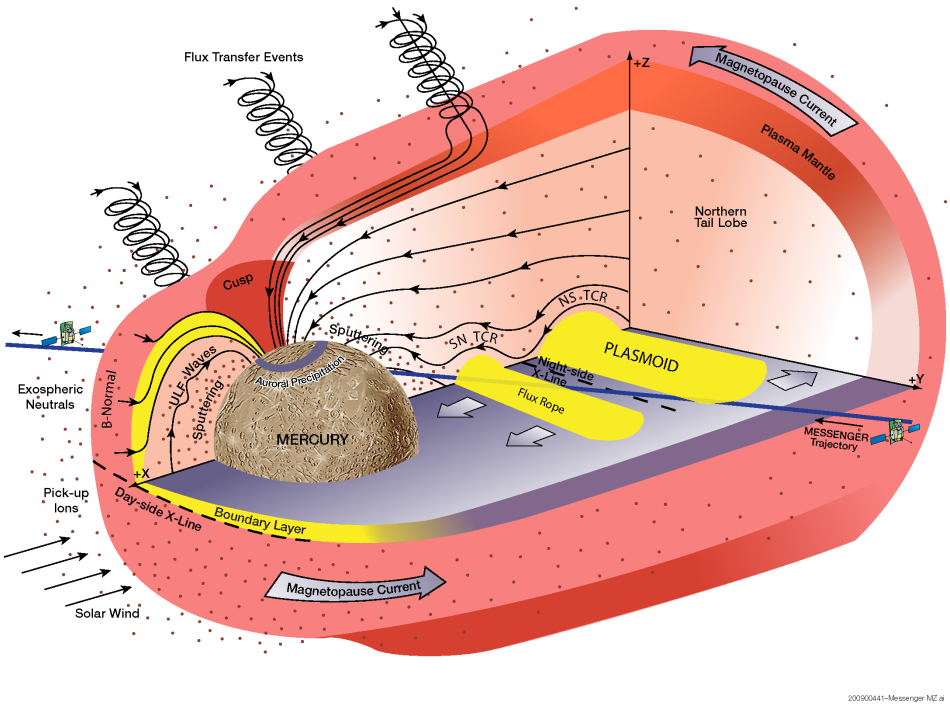

Figure 1. Schematic of Mercury's Dungey cycle. This large-scale magnetospheric convection, responsible for the circulation of plasma and magnetic flux, is driven by steady and impulsive reconnection. Note the strong magnetic field normal to the dayside magnetopause, the large FTEs, and the reconnection line in the near-tail region. Figure from *Slavin et al.* [2009].

The magnetosphere of Mercury is of interest in many respects. It is characterized by spatial and temporal scales much smaller than those at Earth (by a factor of 8 and 30, respectively [e.g., *Russell and Walker*, 1985]). Boundary conditions also are quite different as compared to those at Earth with a dense solar wind and B_X dominated IMF at the outer boundary as well as a tenuous atmosphere at the inner boundary. Mercury's intrinsic magnetic field has a dipole moment of 195 nT-R_M^3, that is aligned to within 3 deg of the planet's spin-axis but has a northward offset of 484 km [*Anderson et al.*, 2011]. As the supersonic, super-Alfvénic solar wind interacts with Mercury's intrinsic magnetic field, a planetary magnetosphere with an elongated magnetotail is formed. There are, however, notable differences between Mercury's magnetosphere and those of other planets with intrinsic magnetic field: Mercury possesses only a very tenuous exosphere consisting of planetary atoms, with some of them being ionized from the high solar radiation at Mercury's

orbit [*Zurbuchen et al.*, 2008, 2011; *Raines et al.*, 2011, 2013]. The lack of a conducting ionosphere implies that any field-aligned currents must close through the planet's regolith [*Anderson et al.*, 2014]. The solar wind is much more intense at Mercury's orbit than at any other planet of the solar system [*Burlaga*, 2001]. Although the solar wind velocity remains relatively constant throughout the heliosphere, its density at Mercury's orbit is 5–10 times larger than typical values at Earth. Additionally, the strength of the IMF is, on average, about 30 nT, increasing the solar wind Alfven speed and enhancing the rate of reconnection with Mercury's magnetic field [*Slavin and Holzer*, 1979].

The combination of Mercury's small dipole moment with the extreme solar parameters results in a small but dynamic magnetosphere (Figure 1). In terms of planetary radii, the planet Mercury accounts for a much larger volume of its magnetosphere than Earth. At Mercury, the average subsolar magnetopause standoff distance is ~1.45 R_M [*Winslow et al.*, 2013] where the typical standoff distance is ~10 R_E at Earth [*Fairfield*, 1971]. Upstream of the magnetosphere, Mercury's bow shock is located at an average distance of 1.96 R_M away from the planet [*Winslow et al.*, 2013]. Due to the low Alfvénic Mach number (M_A) and low β, the ratio of plasma pressure to magnetic pressure, solar wind conditions at Mercury's orbit, the bow shock is weaker and exhibits smaller magnetic overshoots compared to the outer planets [*Masters et al.*, 2013].

Like Earth, the open-closed field line boundaries of Mercury's magnetosphere map to high latitude, dayside magnetospheric cusps. The northern cusp is evident in both MESSENGER plasma and magnetic field data in the vast majority of orbits that cross the region. MESSENGER's passages over southern cusp were at much larger altitudes and can only be indirectly inferred from measurements. The cusp appears as a strong enhancement in plasma flux, composed of solar wind and planetary ions [*Zurbuchen et al.*, 2011; *Raines et al.*, 2013] standing between two regions of much lower plasma density. These enhancements span Mercury latitudes ~30°–80°N and local times 6–14 h. The cusp is manifested in magnetic field data mainly as depressions in the field, attributed to the diamagnetic influence of the plasma present there. *Winslow et al.* [2012] performed a statistical analysis of these depressions. Their analysis showed that the cusp is a broad, highly variable region located around 56°–84°N magnetic latitude and 7–16 h local time, marking a similar region on Mercury's dayside as the plasma enhancements inferred from diamagnetic depressions. This spatial extent is more similar to the V-shaped outer cusp at Earth than the narrow cleft found at lower altitudes [*Smith and Lockwood*, 1996; *Lavraud et al.*, 2005].

Ion measurements from MESSENGER's first Mercury flyby confirmed that Mercury's magnetosphere has an Earth-like central plasma sheet [*Raines et al.*, 2011]. The trajectory of this flyby was unique in that it passed nearby and almost parallel to Mercury's equatorial plane, providing an opportunity to observe across the plasma sheet not available in the orthogonal passes provided throughout the orbital phase. Those authors compared measurements at Mercury to a long baseline study of the plasma sheet at Earth [*Baumjohann and Paschmann*, 1989]. Accounting for the expected 5-10 fold higher solar wind densities at Mercury's orbit in the heliosphere, the measured proton density in Mercury's plasma sheet of 1-12 cm^{-3}, was comparable with those at Earth (0.2-0.5 cm^{-3}) during similarly quiet magnetospheric conditions. Proton temperature was much lower than the average at Earth, 2 MK versus 30-56 MK, respectively. Plasma beta, the ratio of magnetic to plasma pressure, was also found to be lower and more steady at ~2 in Mercury's central plasma sheet. At the

Earth, plasma beta varies from ~0.3 near the edges of the plasma sheet, to ~30 in the center. More details concerning plasma sheet observations are included in Section 3 below.

2.1.1 Plasma depletion layers

The low-β conditions in Mercury's magnetosheath are further exacerbated by the frequent presence of plasma depletion layers (PDLs), caused by the draping and compression of the IMF as it encounters the magnetopause boundary (Figure 2). This concept of PDLs was initially introduced by *Zwan and Wolf* [1976], who predicted that the natural draping of the IMF would lead to the formation of low-β layers adjacent to the dayside magnetopause which they termed plasma depletion layers. It was also predicted that the PDL thickness would be larger for low M_A and β conditions, when magnetic pressure is dominating the magnetosheath, as is the case at Mercury [*Zwan and Wolf*, 1976]. Consistent with this prediction, *Gershman et al.* [2013] analyzed MESSENGER MAG and FIPS measurements to determine that lower upstream M_A (M_A ~3–5) values led to stronger depletion effects in the PDLs at Mercury. In this study, *Gershman et al.* [2013] identified 40 orbits where a PDL, adjacent to the dayside magnetopause, was observed as MESSENGER crossed through the magnetosheath. A typical PDL thickness was determined to be ~300 km, or ~0.12 R_M. The PDLs were observed for both quasi-perpendicular and quasi-parallel shock geometries as well as for all IMF orientations. Despite the high frequency of reconnection occurring at Mercury's dayside magnetopause due to the low-β environment [*DiBraccio et al.*, 2013], this substantial reconnection is not sufficient enough to transport all of the magnetic flux pileup and therefore the PDLs are a persistent feature of Mercury's magnetosheath. However, *Gershman et al.* [2013] also concluded that plasma depletion does not appear to exist during times of extended northward IMF.

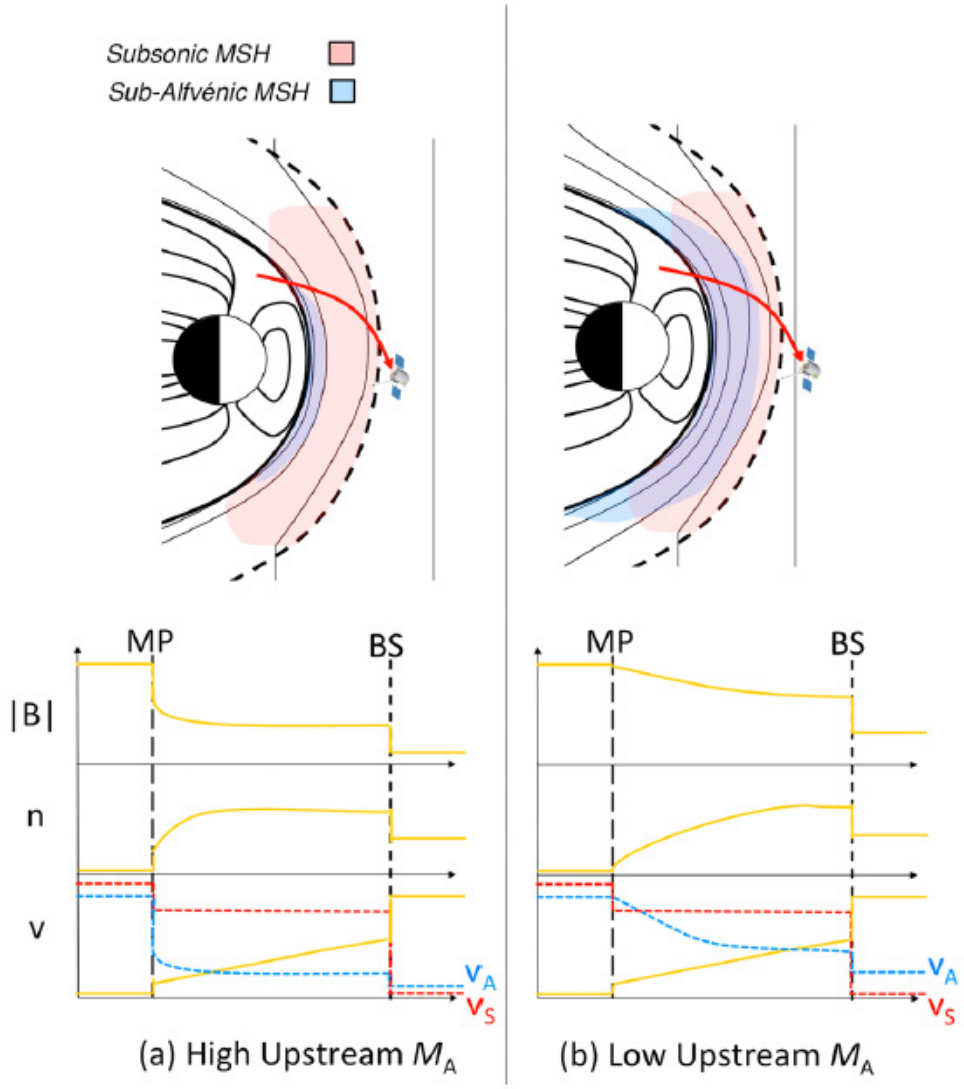

Figure 2. Illustration of a spacecraft pass through the subsolar magnetosheath (MSH) for (a) high solar wind Mach number (M_A) and (b) low solar wind M_A. The MSH plasma is subsonic equatorward of the approximately ±45° latitude. With decreasing M_A, a larger fraction of the subsolar magnetosheath is sub-Alfvenic, as indicated by the blue shaded region. In addition, a thicker region of magnetic flux pileup is evident by an increase in |**B**| and a decrease in plasma density, n. The Alfven speed (V_A) and sound speed (V_S) are also shown for both cases. *Adapted from Gershman et al.,* 2013.

2.1.2 Observations of induction effects

Given the mean subsolar magnetopause distance of only 1.45 R_M from the center of the planet [*Winslow et al.*, 2013] and the high magnetopause reconnection rate [*Slavin et al.*, 2009; *DiBraccio et al.*, 2013], it seems reasonable to conclude that Mercury's surface may become directly exposed to the solar wind. *Slavin and Holzer* [1979] predicted that the low-M_A nature of Mercury's space environment, especially during periods of high solar wind pressure, would allow reconnection to erode the magnetopause down to the planetary surface. However, at the same time *Hood and Schubert* [1979] and *Suess and Goldstein* [1979] predicted that induction effects at Mercury would cause the subsolar magnetopause to remain at or above 1.2 R_M.

Mercury's 2000 km radius, iron-rich, highly electrically conducting core [*Smith et al.,* 2012] gives rise an interaction that sets it apart from all other planetary magnetospheres. In the presence of this electrically conducting sphere, changes in upstream solar wind pressure will create changes in the magnetic field normal to the planetary surface. According to Faraday's law, these time-dependent changes will generate currents in the conducting core, which will serve to oppose this change in magnetic field and temporarily increase Mercury's magnetic moment, therefore limiting how far the magnetopause will be compressed [*Hood and Schubert*, 1979; *Suess and Goldstein*, 1979; *Glassmeier et al.,* 2007].

To test these predictions and assess the roles of reconnection erosion and induction effects at Mercury, *Slavin et al.* [2014] analyzed three extreme solar wind dynamic pressure events using MESSENGER magnetic field and plasma measurements. Two of these events were due to coronal mass ejections (CMEs) and the third one was due to a high-speed stream. During these orbits, the magnetic field just inside the dayside magnetopause exceeded 300 nT with inferred solar wind pressures of ~ 45–65 nPa. This field magnitude is double the typical strength of ~ 150 nT just inside the magnetopause [*DiBraccio et al.,* 2013; *Winslow et al.,* 2013], which corresponds to solar wind ram pressures of ~ 10 nPa. During these events, intense reconnection was observed in the form of frequent Flux Transfer Events (FTEs) and steady reconnection rates derived from the normal magnetic field component to the magnetopause of 0.03 - 0.20..

In Figure 3, the thin dashed curve illustrates the observed sixth-root relationship between solar wind dynamic pressure and magnetopause standoff distance determined by *Winslow et al*. [2013]. The thick dashed line shows the predicted relationship between solar wind ram pressure and magnetopause standoff distance when induction effects are included. As evident in the figure, induction effect models predict that the magnetopause standoff distance will only be compressed below ~1.2 R_M for solar wind pressures larger than ~60 nT. The points on this plot indicate the magnetopause standoff distances, extrapolated to the subsolar point, for the boundary crossings observed during the three extreme solar wind events. The subsolar magnetopause was observed at much lower altitudes than predicted during these extreme solar wind intervals [*Hood and Schubert*, 1979; Glassmeier et al., 2007] due to reconnection, which appears to be opposing the shielding effects of the induction currents. Therefore, during these days of extreme solar wind pressure, Mercury's magnetopause remains close to the surface due to the strong effect of dayside reconnection, which transfers magnetic flux into the magnetotail [*Slavin and Holzer*, 1979]. This result confirms that magnetic reconnection at Mercury is very intense and that both high-intensity reconnection as well as magnetosphere-core coupling must be included in global models of Mercury's magnetosphere during extreme solar wind pressure conditions.

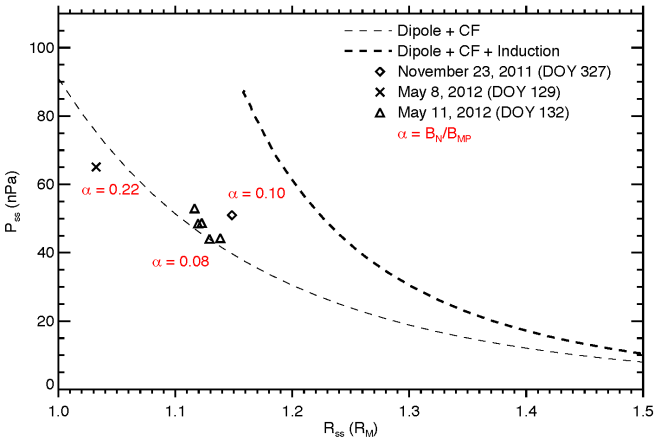

Figure 3. Solar wind ram pressure, P_{SW}, versus extrapolated magnetopause standoff distance, R_{SS}, for the magnetopause crossings of *Slavin et al.* [2014]. The magnetopause crossings on 23 November 2011, 8 May 2012, and 11 May 2012 are shown as a diamond, cross, and triangles, respectively. The dimensionless reconnection rate, α, averaged over the magnetopause crossings for each event, is also displayed for each event. The sixth-root relationship (thin dashed line) determined from a large data set of MESSENGER magnetopause encounters at typical upstream pressures of ~ 5 to 15 nPa [*Winslow et al.*, 2013] is compared with a theoretical model that includes the effects of induction in Mercury's interior [*Glassmeier et al.*, 2007] (thick dashed line). Figure from *Slavin et al.* [2014].

2.2 Dungey cycle at Mercury

Mercury's solar wind-driven magnetosphere experiences a circulation of plasma and magnetic flux similar to that of the Earth. This process is termed the Dungey cycle [*Dungey,* 1961; *Cowley*, 1982; see also Seki et al., this volume]. The Dungey cycle begins with magnetic reconnection between the IMF and planetary magnetic field at the dayside magnetopause, resulting in open fields with one end rooted to the planet and the other in the solar wind. This open magnetic flux facilitates the exchange of solar wind and planetary plasma to and from the magnetosphere. The open fields are then carried downstream by the solar wind flow until they join the north and south lobes of the magnetotail. The oppositely directed fields of these tail lobes meet at the cross-tail current sheet where they reconnect. Tail reconnection creates two new magnetic field lines, a detached field line that rejoins the IMF and a closed field line with both ends attached to the planet. This closed field line convects sunward toward the planet, eventually moving toward the dayside and completing the cycle. Using observations from the second MESSENGER flyby of Mercury, *Slavin et al.* [2009; 2010] determined Dungey cycle times of ~2 min, which is much shorter than the 1 h convection times at Earth [*Siscoe et al.*, 1975].

The Dungey cycle time is one of the keys for understanding the dynamical response of planetary magnetospheres to changes in the rates of magnetic reconnection at the magnetopause and in the magnetotail. It is determined by observing the rate of convection at various points in the cycle, as depicted in Figure 1. For example, the cycle time may be deduced from the time for ionospheric plasma to **E** × **B** drift anti-sunward across the polar cap and return at lower latitudes to its point of initiation. Alternatively, the cross-magnetospheric electric field may be inferred

from observations of the rate of magnetic flux being reconnected and transferred to/from the magnetotail or measured directly with electric field instrumentation. At Earth the time necessary for this cycle is in the range of 1–2 hr [*Cowley*, 1982]. However at Mercury, *Hill et al.* [1976] noted that the lack of an ionosphere, and the expected resistive nature of the regolith, eliminates the need to take into account "line-tying" or "saturation" effects [see *Kivelson and Ridley*, 2008] that reduce the cross-magnetospheric electric field at Earth from the maximum value, $-\mathbf{V}_{SW} \times \mathbf{B}_{SW}$, applied by the solar wind. *Siscoe et al.* [1975] then used scaling arguments and typical solar wind and IMF parameters to estimate that the Dungey cycle at Mercury would be of the order of 1 min.

MESSENGER's observations taken during its second flyby on 6 October 2008 provided the first opportunity to more directly infer the Dungey cycle time at Mercury. *Slavin et al.* [2009] used the magnetometer measurements [*Anderson et al.*, 2007] to determine the magnetic field normal to the magnetopause and, with assumptions, calculated a cross-magnetospheric electric field of about 2 mV/m, which corresponds to a Dungey cycle time of 2 min. MESSENGER's third flyby on 29 September 2009 provided another opportunity to determine the Dungey cycle time when a series of loading – unloading events were observed as the magnetotail was traversed. At Earth magnetospheric substorms are often associated first with an interval of net magnetic flux transfer to the magnetotail, termed loading, which ends with the onset of magnetic reconnection in the cross-tail current layer and the dissipation of the magnetic flux stored in the tail [*Baker et al.*, 1996]. The duration of the tail loading and unloading intervals, sometimes referred to as the "growth" and "expansion" phases of the substorm because of the accompanying auroral signatures [*McPherron et al.,* 1973], are typically on the order of the Dungey cycle time. *Slavin et al.* [2010] analyzed the magnetic field measurements during the third flyby and found a total of four loading – unloading events. In each case the duration of the event was ~ 2 – 3 min and in reasonable agreement with the earlier estimate based upon the magnetic field normal to the magnetopause (i.e., dayside reconnection rate). We will show below that analogues to many aspects of the terrestrial substorm have been observed at Mercury, but on a time scale comparable to this miniature magnetosphere's Dungey cycle.

2.3 Magnetotail loading & unloading

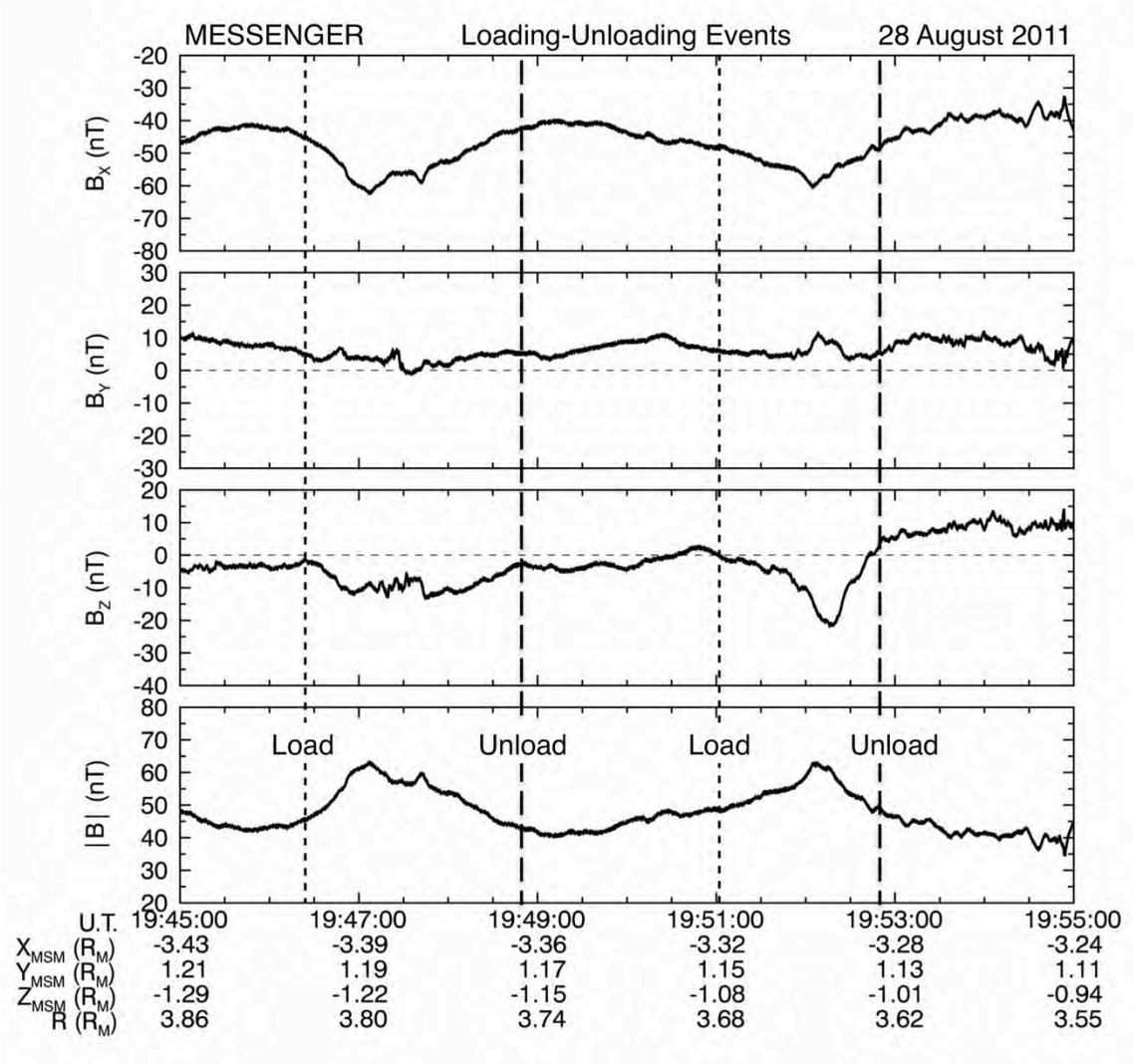

Figure 3: Substorms at Mercury – Loading/Unloading Events.

As already discussed, dayside reconnection at Earth loads the tail lobes with magnetic flux and increases the tail's overall energy levels, which are later dissipated via tail reconnection and substorms. This enhanced loading of the tail lobes with magnetic flux causes the enhanced flaring of the flank magnetopause and increases the fraction of solar wind ram pressure applied directly to the magnetotail [*Caan et al.*, 1973]. In this manner, loading of the tail with magnetic flux is reflected in the magnetic field measurements both as an increase the flaring of the magnetic field (i.e., $|B_Z|$ and/or $|B_Y|$) and in the total magnetic field magnitude. At Earth, the increase in the intensity of the lobe region magnetic field intensity during the substorm loading – unloading cycle is typically ~ 10 to 30% [*Milan et al.,* 2004; *Huang et al.,* 2009]. However, the fractional enhancement in the lobe magnetic field observed at Mercury during the third flyby loading events appeared much larger, perhaps even reaching 100% [*Slavin et al.,* 2010].

MESSENGER observations since orbit insertion on 18 March 2011 have provided many opportunities to observe these loading – unloading events in the magnetotail. A comprehensive analysis has yet to be carried out, but Figure 3 shows

two examples of this phenomenon on 28 August 2011 where, between 19:45 and 19:55 UTC, two loading – unloading events are evident. MESSENGER was located in the south lobe of the tail at a distance of ~3.3 R_M behind the planet. Each event begins with a total magnetic field intensity of ~40 nT directed primarily in the $-X_{MSM}$ direction. The field then increases for ~1 min until it reaches at peak value of ~65 nT. This increase in total field is closely correlated with the B_Z component becoming more negative as the magnetic field flares away from the central axis of the tail. After the peak in total intensity the B_Z component becomes less negative as the intensity decreases back to its pre-substorm levels. The total increase in field magnitude during these events, ~50%, is significantly larger than observed at Earth, but below the larger values observed during the third flyby. The duration of the events, ~2 min, is very close to the value determined from measurements of dayside magnetopause reconnection rate [*Slavin et al.*, 2009; *DiBraccio et al.*, 2013].

3 Sources

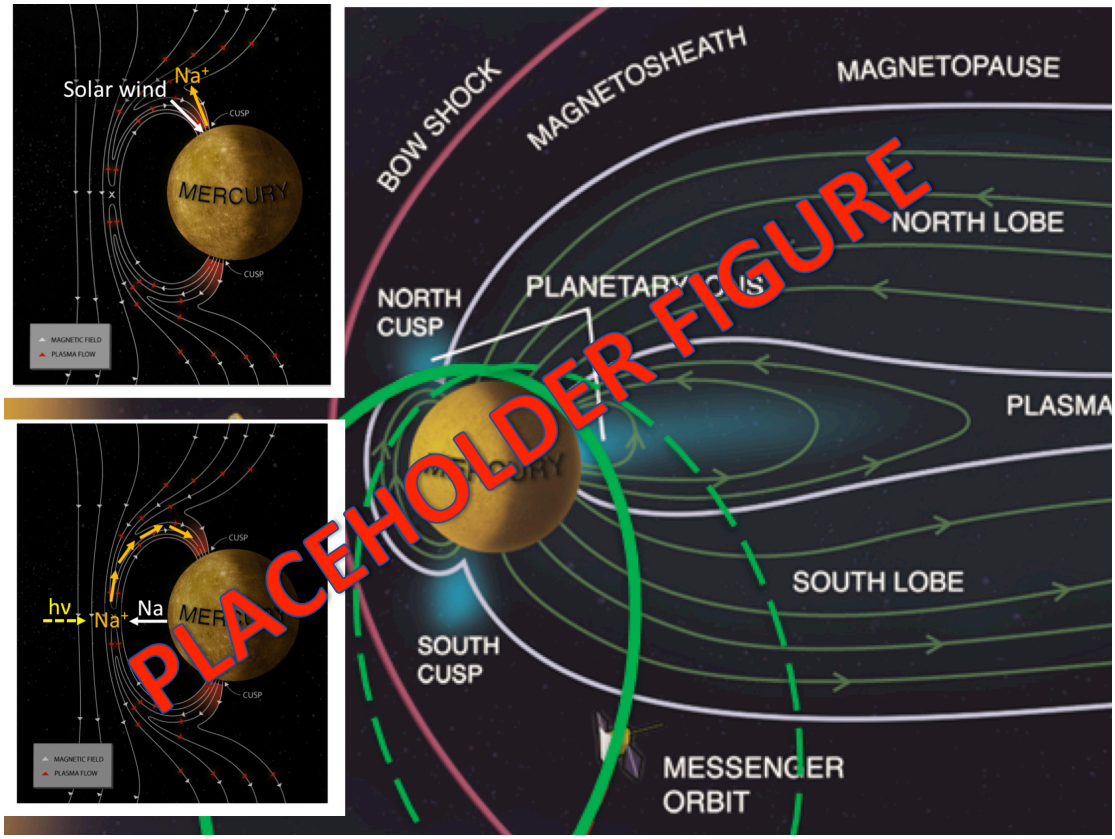

Figure AA. Plasma sources to Mercury's magnetosphere.

3.1 Solar wind entry

The solar wind is an important source of plasma to Mercury's magnetosphere. It can enter the magnetosphere mainly through five processes, studied in detail at Mercury: Magnetopause reconnection followed by entry via the plasma mantle, Flux Transfer Events (FTEs), and Kelvin-Helmholtz waves are described below. Cusp precipitation following magnetopause reconnection is described in Section 3.2.3.2. The fifth process, direct impact of the solar wind on the surface, due either to erosion

or compression of the dayside magnetopause, has been studied only indirectly (Section 2.1.2).

3.1.1 Magnetopause reconnection and the plasma mantle

Magnetopause magnetic reconnection is the dominant process for the transfer of mass, momentum, and energy between the solar wind and Mercury's magnetosphere. The resulting field topology exhibits a magnetic field component that is normal to the magnetopause, B_N. This was first observedat Mercury's magnetopause, indicating that magnetic reconnection had occurred, during the second MESSENGER flyby of Mercury on 6 October 2008 [*Slavin et al.*, 2009]. During this period, the IMF was oriented southward, a configuration that is conducive to reconnection. Using a minimum variance analysis (MVA), *Slavin et al.* [2009] determined a significant, non-zero B_N, ~13 nT, at the outbound magnetopause crossing, indicating that the boundary was a rotational discontinuity. The dimensionless reconnection rate, α, is determined by:

$$\alpha = \frac{B_N}{B_{MP}}$$

where B_{MP} is the magnitude of the field just inside the magnetopause. During this second flyby, *Slavin et al*. [2009] calculated a reconnection rate of $\alpha = 0.13$.

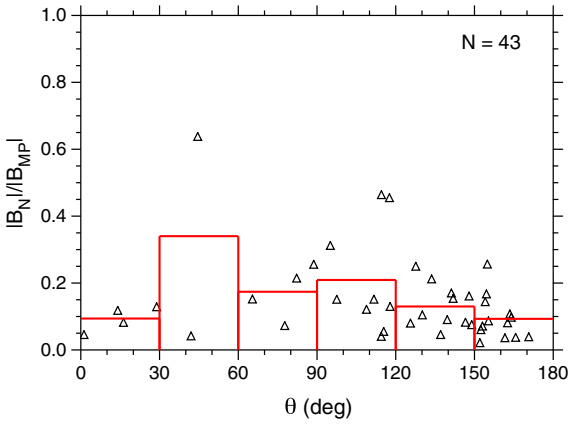

Figure 4. Magnetopause shear angle θ compared with the rate of reconnection for the magnetopause crossings. The average reconnection rate was calculated in 30° bins, as indicated by the red rectangles. Little correlation between

In a statistical survey of magnetopause reconnection at Mercury, *DiBraccio et al.* [2013] identified 43 events with well-determined boundary normal vectors. The average B_N was ~20 nT, an order of magnitude larger than typical measurements at Earth. Additionally, the mean rate of reconnection resulting from this study was $\alpha = 0.15 \pm 0.02$, which is about a factor of three larger than the most extensive studies at Earth. However, more importantly, this study revealed that reconnection occurs at Mercury's magnetopause independent of the magnetic shear angle θ, the angle between the planetary field and the IMF (Figure 4). In fact, *DiBraccio et al*. [2013] identified several reconnection events with $\theta < 30°$, including one event where $\theta \sim 1°$. Upon further inspection, the low-shear reconnection at Mercury appears to be a product of the low plasma β and decreased Alfvénic Mach number (M_A) of the solar wind in the inner heliosphere, as predicted by *Slavin and Holzer* [1979]. The frequency of strong PDLs [*Gershman et al.*, 2013] to also appears enhance the occurrence of reconnection for all IMF shear angles at Mercury [*Slavin et al.*, 2014].

the two quantities is evident, indicating that the reconnection occurs at Mercury for a large range of shear angles

Using MESSENGER FIPS and MAG data, *DiBraccio et al.* [in prep] presented the first observations of Mercury's plasma mantle, a main source for solar wind entry into the planet's magnetosphere, located in the high-latitude magnetotail. The plasma mantle is created as reconnected fields, populated with solar wind plasma, convects downstream of the planet and rejoin the magnetosphere as part of the Dungey cycle. The analysis of two successive orbits on 10 November 2012, revealed a dense population of solar wind protons present just inside the high-latitude tail magnetopause [*DiBraccio et al.*, in prep]. These two events, with durations of 16 and 21 min, exhibited clear dispersions in the proton energy distributions observed by FIPS. This dispersion indicated that low-energy protons were transported much deeper into the magnetosphere than the higher energy particles, which escape to large downtail distances before they can $\mathbf{E}\times\mathbf{B}$ drift deeper toward the plasma sheet, where $\mathbf{E}$ and $\mathbf{B}$ is the cross-tail electric field and magnetic field magnitude, respectively. Frequent FTEs observed throughout the magnetosheath, cusp, and into the magnetotail during these orbits are supportive of the high reconnection rates measured at Mercury and suggest that intense dayside reconnection is responsible for transporting solar wind plasma into Mercury's magnetosphere just as at Earth. Observations of Mercury's plasma mantle have provided direct evidence of one mechanism responsible for transporting solar wind plasma into the magnetosphere, which has consequences for surface space weathering especially through nightside plasma precipitation.

3.1.2 Flux Transfer Events

Reconnection is also observed at Mercury's magnetopause in the form of FTEs [*Slavin et al.*, 2008, 2009, 2010, 2012b; *Imber et al.*, 2014]. FTEs are created as reconnection occurs between the IMF and planetary magnetic field at multiple dayside X-lines. They are identified by their flux rope topology: a strong, axial-aligned core field with helical outer wraps increasing in pitch angle with radial distance from the center. In magnetic field data, the helical wraps are typically indicated by a bipolar signature, which also provides information about the direction that the flux rope is traveling. The core field is designated by a local field enhancement that is coincident with the inflection point of the bipolar signature. Flux

ropes may also be remotely observed if the spacecraft does not directly pass through the FTE, but rather, encounters the draped and compressed fields surrounding the flux rope. These perturbations, called traveling compression regions (TCRs), are used to infer the dimensions of a flux rope.

During the first MESSENGER flyby of Mercury, *Slavin et al.* [2008] identified a ~4-s-duration FTE in the magnetosheath using magnetic field data implying a size of ~1200 km, or 0.5 R_M. The bipolar signature is evident in the B_Y component with an enhancement in both B_X and B_Z. During the second MESSENGER flyby, *Slavin et al.* [2009] reported a FTE with a core field strength of 160 nT and a duration of ~3 s (Figure 5). The size of this flux rope was estimated to be ~900 km, or 0.4 R_M. After a more extensive review of the MESSENGER flybys, *Slavin et al.* [2010] reported on six FTEs encountered during the first and second Mercury flybys. The durations of these events ranged from 1–6 s and a flux rope modeling technique [*Lepping et al.*, 1990, 1995, 1996] was implemented and determined the FTE diameters to range from 0.15–1.04 R_M. Additionally, the model results indicated that the magnetic flux content of these structures ranges from 0.001–0.2 MWb, or about 5% of the 4–6 MWb tail lobe flux [*Slavin et al.*, 2010]. Additionally, the largest of these events may contribute up to ~30 kV to the cross-magnetospheric electric potential.

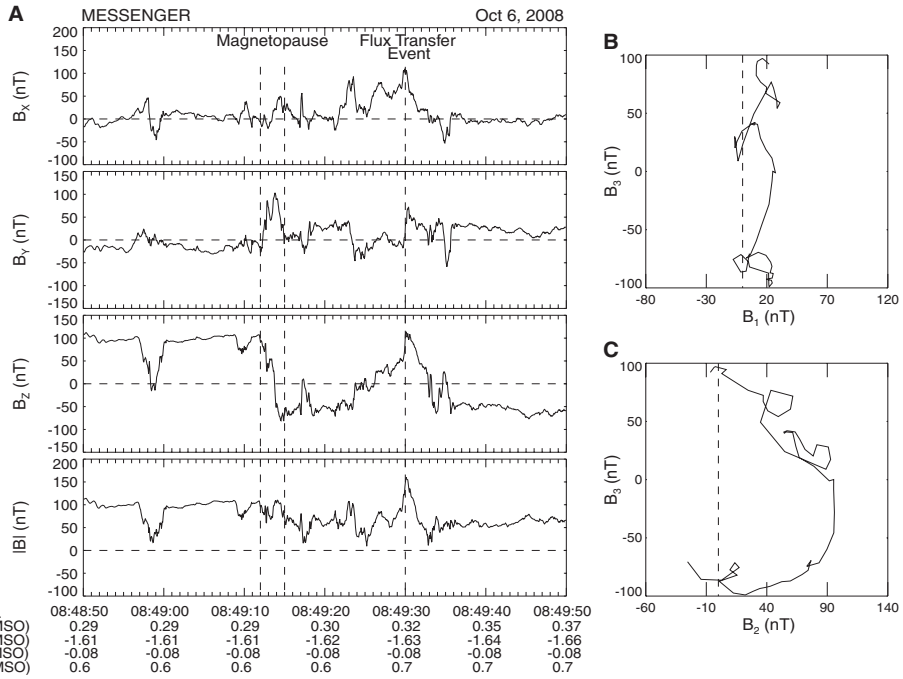

Figure 5. (A) Magnetic field observations of the inner current sheet and MP boundary observed as MESSENGER exited the dawn-side magnetosphere. (B) Magnetic field measurements across the MP graphed in the plane of maximum and minimum variance. (C) Magnetic field measurements across the MP graphed in the plane of maximum and intermediate variance *Adapted from Slavin et al.,* 2009.

At Mercury's magnetopause, flux ropes have been identified to occur as "FTE showers" [*Slavin et al.*, 2012b]. During a MESSENGER noon-midnight orbit on 11 April 2011, a combination of 163 FTEs and TCRs were observed over a 25 min interval as the spacecraft traversed the southern tail magnetopause (Figure 6). During this orbit, the IMF was predominantly oriented northward. The average duration of the FTEs and TCRs was 1.7 s and 3.2 s, respectively, and all events were separated by

periods of ~8–10 s. By implementing the flux rope modeling technique of *Hidalgo et al.* [2002a, 2002b], the mean semimajor axis of the flux ropes was determined to be 0.15 R_M.

Most recently, *Imber et al.* [2014] performed a statistical study on FTEs observed in Mercury's subsolar magnetosheath. In this study, 58 large-amplitude FTEs, with core fields larger than the magnitude of the planetary field just inside the magnetopause, were selected. The average durations of these events were 2.5 s. MVA was used to determine their orientation and the force-free flux rope model of *Lepping et al.* [1990, 1995, 1996] was applied to estimate an average flux content of 0.06 MWb. *Imber et al.* [2014] concluded that unlike Earth, where FTEs contribute to < 2% of substorm flux transport, at least 30% of the flux transport required to drive Mercury's 2–3 min substorms is contributed by FTEs.

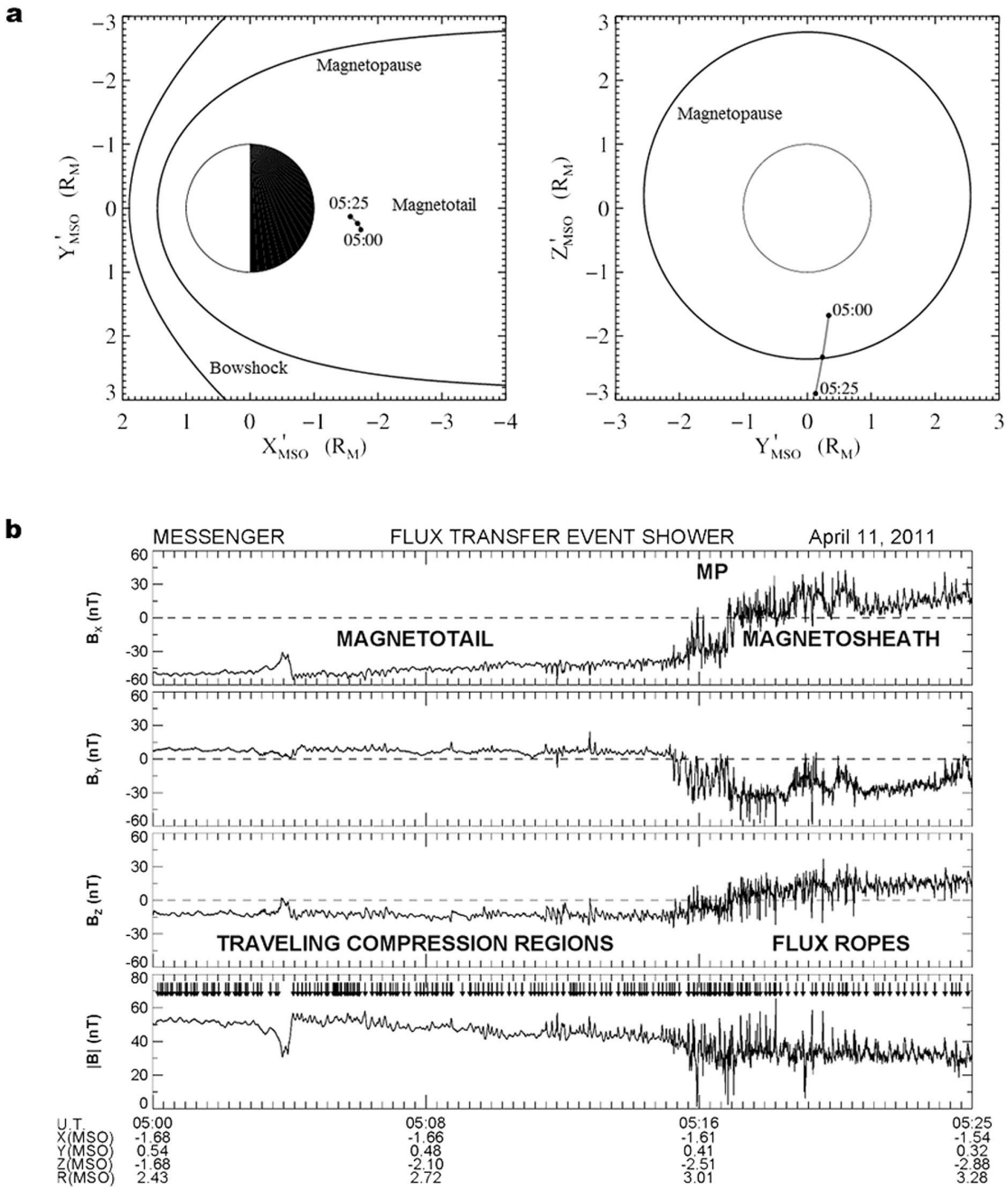

Figure 6. MESSENGER trajectory from 05:00 to 05:25 UTC on 11 April 2011, projected on to the aberrated MSO *X-Y* and *Y-Z* planes. Note that the bow shock and magnetopause surfaces are shifted northward by 0.20 R_M to match the northeward offset in Mercury's internal magnetic dipole. (b) Magnetic field measurements taken during this interval span the outer portion of the southern lobe of Mercury's magnetotail, the magnetopause, and the nearby magnetosheath. Vertical arrows in the fourth panel mark 97 TCRs inside the magnetotail and 66 FTE-type flux ropes in the adjacent magnetosheath. *Adapted from Slavin et al.,* [2012b].

3.1.3 Kelvin-Helmholtz waves

Kelvin-Helmholtz (KH) instabilities are another well-known mechanism responsible for the transfer of mass, momentum, and energy from the solar wind into planetary magnetospheres. In situ observations of KH waves at a planetary magnetopause can be identified as surface waves creating a series of periodic magnetopause crossings. Indeed, the growth rate of KH waves relies on the velocity shear and finite Larmor radius effects. During the first MESSENGER flyby of Mercury, *Slavin et al.* [2008, 2009] reported possible KH wave activity after identifying three rotations along the dusk magnetopause while the IMF had a northward orientation. The durations of these field rotations were ~5–25 s, implying spatial scales of ~0.2–2 R_M. *Sundberg et al.* [2010] studied these events in further detail and concluded that the observed waves were not due to KH instabilities but might possibly indicate an initial perturbation leading to KH vortices further down the tail.

During the third MESSENGER flyby, *Boardsen et al.* [2010] identified magnetic field variations indicated by 15 dusk-side magnetopause crossings over a short 2-minute interval, likely suggesting the presence of KH instabilities. Additionally, a distinct sawtooth pattern present in B_Y and, to a lesser extent, B_X, supports the conclusion of highly steepened KH wave activity. *Sundberg et al.* [2011] revisited these observations and performed a reconstruction of the KH vortex, with the assumption that the wave pattern is quasi-stationary. This analysis concludes that the spatial reconstruction of a vortex pattern is in agreement with the field rotations located at the dusk-side magnetopause during the third MESSENGER flyby.

To understand the general characteristics of KH waves at Mercury's magnetopause, *Sundberg et al.* [2012] performed a survey of six KH wave trains by identifying the events based on sawtooth wave patterns (Figure 7) and periodic magnetopause crossings in magnetic field data. The results provide clear evidence that KH waves are frequently observed at Mercury's dusk-side magnetopause with wave periods ranging from 10–40 s and large-amplitude oscillations ranging from 70–150 nT.

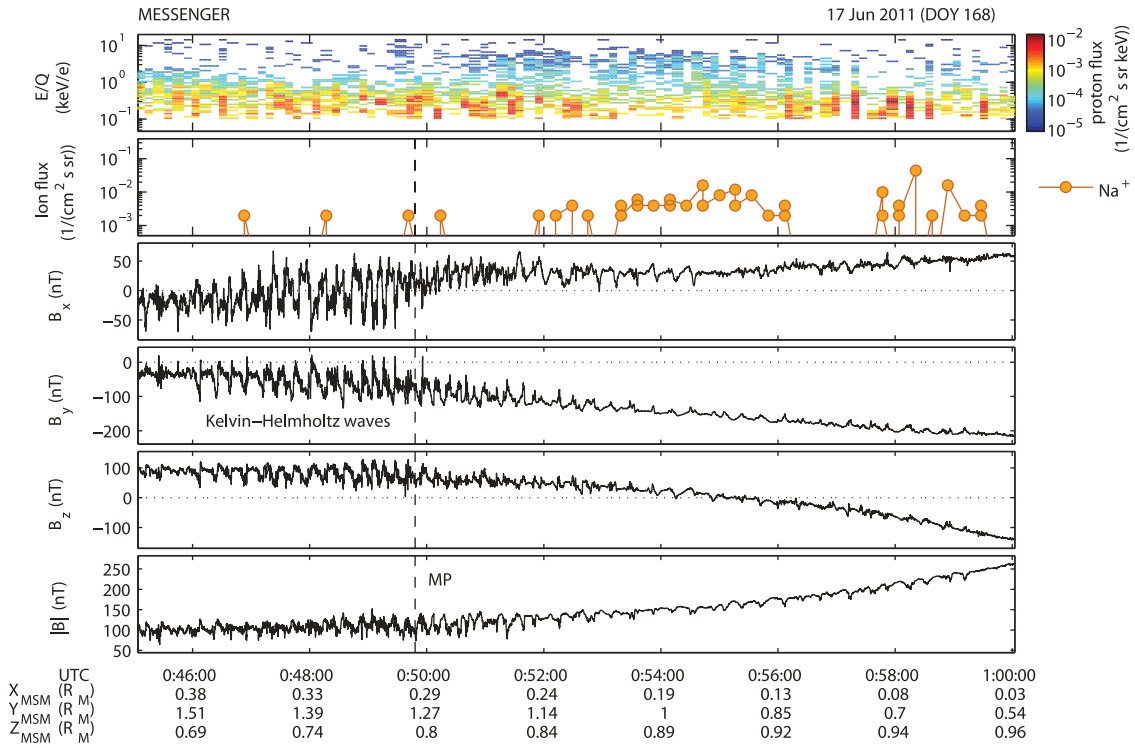

Figure 7. KH observations on 17 June 2011. The first and second panels show the FIPS spectrogram of *E*/*Q* for the measured proton flux and the sodium ion count rate, respectively. The third–fifth panels are the magnetic field components and the sixth panel is magnetic field strength. *Adapted from Sundberg et al.* [2012].

Gershman et al. [2015] showed that KH waves observed on Mercury's dusk-side (~18–21 h local time) magnetopause can be affected by the presence of heavy planetary ions. On the dusk-side, where Na^+-group ions (*m/q* 21–30) can dominate the pressure, KH waves appear at the Na^+ ion gyrofrequency. This kinetic-scale behavior is due to the large gyroradii of these planetary ions. This is contrasted with the fluid-scale behavior of other KH waves observed at Mercury, especially on the dayside region around the dusk terminator (12–18 h local time). This work constitutes the best evidence to date that Na^+-group ions can be dynamically important in the magnetosphere, an open question since the discovery of the Na-dominated exosphere at Mercury.

3.2 Planetary ions

Planetary ions are formed at Mercury, either by ionization from exospheric neutral atoms or from processes that act directly on the surface. As a result, both the surface and the exosphere are significant plasma sources to Mercury's magnetosphere.

3.2.1 Surface processes

Exogenic processes acting on the surface causing particle release permanently populate Mercury's exosphere, the thin, collision-free, gaseous envelope around the planet. Ionization of these exospheric particles contributes significantly to the magnetospheric population of ions. Four processes have long been considered for particle release at Mercury: thermal desorption (TD), photon-stimulated desorption

548 (PSD), micro-meteoritic impact vaporisation (MIV), and ion-induced particle
549 sputtering (IS). These particle release processes have been reviewed several times
550 [e.g., *Wurz and Lammer*, 2003; *Killen et al.*, 2007 and General Processes chapter of
551 this volume] and have been extensively studied for Mercury [e.g., *Mura et al.*, 2009;
552 *Wurz et al.*, 2010].
553 The intense solar irradiation of the surface is responsible for TD and PSD, i.e.,
554 these processes are confined to the dayside of Mercury. TD is restricted to volatile
555 species, i.e., species that have an appreciable sublimation rate at the surface
556 temperatures of Mercury, 100–700K. These volatiles (H_2, N_2, O_2, H_2O, CO_2, He, Ne,
557 Ar and molecular fragments thereof) are expected to constitute the major part of
558 Mercury's dayside exosphere, but only He has been detected so far. Contributions by
559 the other three processes are orders of magnitude lower [*Wurz and Lammer*, 2003;
560 *Wurz et al.*, 2010]. Since the evaporation rates for the dayside temperatures are large,
561 volatile species falling onto the surface will be re-emitted almost immediately into the
562 exosphere and will be thermally accommodated with the surface temperature. Only at
563 the night side some volatiles can condense and are thus removed from the exosphere.
564 Thus, a day-night modulation in exospheric density of some volatiles is expected, as
565 was observed for argon in the lunar exosphere [*Stern*, 1999]. Since TD-released
566 particles have thermal energies, they all fall back onto the surface and escape (Jeans
567 escape) is negligible. The contribution to the magnetosphere is via photoionization of
568 exospheric gas. Since the scale heights of thermal particles are low, and thus the
569 ballistic travel times are low, the flux of photoions from thermal species is moderate.
570 PSD, also driven by solar irradiation, is even more restricted than TD for
571 species it can release from the surface: at Mercury only Na and K are released by this
572 process. However, appreciable PSD yields of Na and K are only observed if the alkali
573 metal is freed from the mineral bound in the crystal and is available as adsorbed atom
574 on the surface [*Yakshinskiy and Madey*, 1999, 2004]. Impacting energetic plasma ions
575 may cause the liberation of the alkali metal from the mineral, which was used in a
576 recent 3D model to explain Na observations during Mercury transit of the Sun [*Mura*
577 *et al.*, 2009]. Alternatively, a surface reservoir of Na was postulated to model the
578 exospheric Na observations during a Mercury year [*Leblanc and Johnson*, 2010]. A
579 part of these models is the consideration of the fate of alkali atoms when they fall
580 back to the surface, which is discussed as sticking probability in surface physics. The
581 sticking probability for atomic K is nearly constant over the surface temperature range
582 of 100–500 K, whereas for Na it decreases with increasing temperature in this range
583 [*Yakshinskiy and Madey*, 2005], which influences the Na/K ratio to be observed in the
584 exosphere. More recently, extensive UVVS observations of Na (K has not been
585 observed by the MESSENGER) have shown that TD is not a significant process for
586 Na [*Cassidy et al.*, 2015]. It is also not seen in the other species regularly observed by
587 UVVS: Ca [*Burger et al.*, 2014] and Mg. The lack of TD is surprising for Na given
588 that it is relatively volatile [*Hunten et al.*, 1988] but may be explained by the
589 relatively large binding energy seen for Na adsorbed on an ion-bombarded surface
590 [*Yakshinskiy et al.*, 2000].
591 MIV will take place everywhere on the surface of Mercury, on the day- and
592 nightside. MIV fluxes at Mercury have been modeled by several authors [*Cintala*,
593 1992; *Müller et al.*, 2002; *Cremonese et al.*, 2005; *Bruno et al.*, 2006; *Borin et al.*,
594 2010]. These fluxes are usually considered omni-directional, though *Killen et al.*
595 [2014] showed that preferential dust bombardment on the dawn hemisphere could
596 explain the concentration of Ca exosphere there [*Burger et al.*, 2014]. The impact of
597 micro-meteorites and meteorites results in the release of surface material in form of

gas and solid fragments [e.g., *Cintala*, 1992] where the gas fraction is a hot thermal expanding cloud composed from all the material of the impact site. Most of the micro-meteorites are indeed very small particles, and thus a constant flux bombards Mercury's surface resulting in a constant contribution to the exosphere [*Wurz et al.*, 2010]. For typical solar wind conditions, MIV and IS give similar exospheric particle populations [*Wurz et al.*, 2010]. However, larger projectiles may sometimes hit the surface causing the exospheric density contribution from MIV to temporarily increase (for about 1 hour) by up to a factor of 100 for projectiles of 0.1 m [*Mangano et al.*, 2007]. Nevertheless, such episodic events have not been observed for the more than 15 Mercury years that UVVS has been regularly observing Na, Ca, and Mg.

IS is the process of particle release upon the impact of an energetic ion on a solid surface. IS is a very well understood process because of its application in semi-conductor industry [*Behrisch and Eckstein*, 2007]. IS depends on the energy of the impacting ion, and the sputter yield, i.e., the number of surface atoms sputtered per incoming ion, is maximal for ions with energy of 1 keV/nuc. All atoms on the surface are released by IS more or less stoichiometrically causing a continuous erosion of the surface. IS arises either from solar wind ions at the locations where solar wind ions have access to the surface of Mercury or by magnetospheric ions, both given by the topology of Mercury's magnetosphere. For typical solar wind conditions the sputtering contribution to the exosphere is small [*Wurz et al.*, 2010], but for CMEs with significantly higher plasma density and increased He^{++} contents the ion sputtering contribution may increase dramatically for the duration of the CME passage, as was recently discussed for the Moon [*Farell et al.*, 2012]. Sputtered particles have high kinetic energies, and a significant fraction of them can escape the gravitational field of the planet [*Wurz et al.*, 2007, 2010]. Because of their large exospheric scale height and the resulting long ballistic flight times, significant ionization of sputtered atoms occurs, which is species dependent, providing input to the ion population of Mercury's magnetosphere. In addition, about 0.1 to 10% of the sputtered atoms are already ionized when sputtered from the surface [*Benninghoven*, 1975], thus contributing directly to the magnetospheric ion population. Magnetospheric dynamics may cause some of these ions to return to the surface [*Delcourt et al.*, 2003] and cause sputtering themselves, including on locations on the night side surface.

3.2.2 Neutral observations

The components of Mercury's exosphere are sources of the magnetospheric ion population mostly through the photoionization process. For this reason, it is important to investigate the density, distribution and variability of the neutral component to understand the plasma populations.

Generally, the observation of the exosphere can be performed by ground-based telescopes in the spectroscopic regions free of Earth atmospheric lines or by in situ measurements with ultraviolet-visible (UV-Vis) spectrometers and mass spectrometers. Particularly in the case of Mercury, ground-based observations can take advantage of both night telescopes and solar telescopes/towers and can provide global imaging of the extended exosphere (disk and tail). So far, only the elements Na, K, and Ca have been observed by ground based telescopes. In situ measurements, instead, can provide high-resolution imaging of local density and allow the detection of lower intensity signals to extend the list of observable species. In both cases the

exosphere brightness is calibrated using photometric models of Mercury's surface [*Hapke*, 1981, 1984, 1986; *Domingue et al.*, 1997].

Mercury's exosphere was discovered by a UV spectrometer onboard Mariner 10 [*Broadfoot et al.*, 1977] that covered part of the extreme and far wavelength ranges (30–167 nm). It discovered atomic H and He, and made a possible detection of O. An occultation experiment on Mariner 10 also provided an upper limit of the total atmospheric abundance, which was higher than the sum of detected constituents [*Fjelbo et al.*, 1976], meaning that some exospheric species remained still undetected. About a decade later, ground-based observations discovered Na, identified via the D1 and D2 emission lines (near 589 nm wavelength), which are caused by resonant scattering of sunlight [*Potter and Morgan*, 1985]. Later, also K and Ca have been detected by ground-based observations [*Potter and Morgan*, 1986, 1997; *Bida et al.*, 2000] and an upper limit for Al, Fe and Si was defined [*Doressoundiram et al*., 2009]. MESSENGER UVVS discovered Mg and Ca^{+}, and in its orbital phase regularly observed Na, Ca, Mg, and occasionally H. Its wavelength range (115 nm – 600 nm) precluded observations of He and K.

The *Broadfoot et al.* [1976] Mariner 10 detection of atomic oxygen was 'very tentative', and it was not replicated by MESSENGER UVVS, which could have easily seen the claimed ~60 Rayleigh emission [*Vervack et al.*, 2011]. *Wurz et al.* [2010] predicted that ion sputtering and impact vaporization should produce large atomic oxygen column density (comparable in magnitude to the observed sodium), but it would be difficult to detect with UVVS given the poor efficiency with which atomic oxygen scatters sunlight [*Killen et al.*, 2009]. This hypothesized oxygen exosphere is a likely source for the abundant oxygen ions detected by FIPS [*Zurbuchen et al.*, 2011; *Raines et al.*, 2013].

Neutral observation of Na revealed, since their first detection, very distinctive features, such as recurrent peaks at mid latitudes [e.g., *Potter et al.*, 1999] and a significant neutral tail in the anti-sunward direction [*Potter et al.*, 2002; *Schmidt et al.*, 2012; *Kameda et al.*, 2009]. Moreover, the variability of these features has been

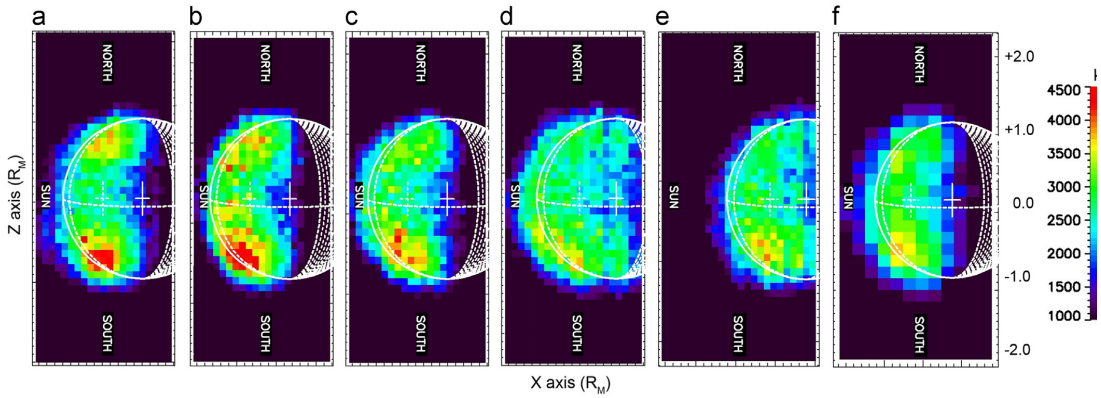

Figure 8. Time sequence of scans of Na emission intensity (in kiloRayleigh) obtained in July 13th 2008 from 7 to 17 UT. The X–Z plane is the projection plane, with the Z-axis pointing northward; the Y-axis is along the direction Earth–Mercury (with the center being the sub-Earth point). The Sun is on the left. The solid white line denotes the disk of the planet and the cross indicating the center of the disk; in white dashed the region of the disk not illuminated by the Sun, the sub-solar meridian, and the cross indicating the point of highest emission brightness due to solar reflection of the surface [*Mangano et al.*, 2013].

seen in almost three decades of Earth-based observations [*Sprague et al.*, 1997; *Potter et al.*, 2006; *Leblanc et al.*, 2009]. The average intensity and tail length modulate

along the Mercury orbit in relation to the solar radiation pressure, which maximizes together with the velocity radial component [*Leblanc et al.*, 2008]. *Kameda et al.* [2009] related the average intensity modulation to the crossing of the interplanetary dust disk. The seasonal variation has been confirmed by MESSENGER UVVS [*Cassidy et al.,* 2015]. Most of the sodium exosphere is confined to low altitudes on the dayside; the scale height is only ~100 km at low latitudes [*Cassidy et al.*, 2015]. This means that most of the ion source is deep within the magnetosphere, which has consequences for sodium ion kinetics [*Raines et al.*, 2013, 2014; *Gershman et al.*, 2014].

The improved spectral and temporal resolution of ground based observations allowed investigation of speed distributions [*Leblanc et al.*, 2009] and detection of even more detailed features of the Na exosphere, which now range from time-scales of days to hours. Daily variations are often due to changes in the position of Mercury around its orbit and to solar events [*Killen et al.*, 2001; *Potter et al.*, 2007]. Hourly variations are attributed to normal solar wind fluctuations (mostly density and speed) and to rapidly changing IMF coupling with the planetary magnetic field [*Mangano et al.*, 2013]. Figure 8 shows an example of hourly variations of high latitude peaks in exospheric Na emission when observed from Earth. Similar double peaks at mid latitudes have been reported for the K exospheric distribution [*Potter and Morgan*, 1986]. This may indicate that both of these volatile species are linked to the solar wind impact onto the Mercury dayside surface below the cusps, even if it cannot be generated by direct ion sputtering [*Mura et al.*, 2009]. Observations of Ca [*Burger et al.*, 2014] and UVVS observations of Na [*Cassidy et al.*, 2015], instead, show different behavior apparently not related to solar wind impact but probably to MIV processes acting more efficiently in certain regions of the orbit due to higher MIV fluxes [*Killen and Hahn*, 2015]. In contrast to the rapid variability of the ground-based observations, UVVS observations of Na and Ca show little episodic variability as described below.

MESSENGER UVVS observations are quite different from, and complementary to, ground-based observations. UVVS provided unprecedented temporal coverage, observing the exosphere almost daily for over 16 Mercury years. It also provided unprecedented spatial resolution: altitude profiles of exospheric emission resolve details down to the km scale (Figure 9). UVVS had the advantage of *not* observing through Earth's atmosphere, but it had limitations, too. It was not an imaging spectrometer, and its field of view (FOV) and observation geometries were restricted by the many considerations of spacecraft operations in a challenging environment. It also had a relatively poor spectral resolution compared to the ground-based observations (~0.5 nm).

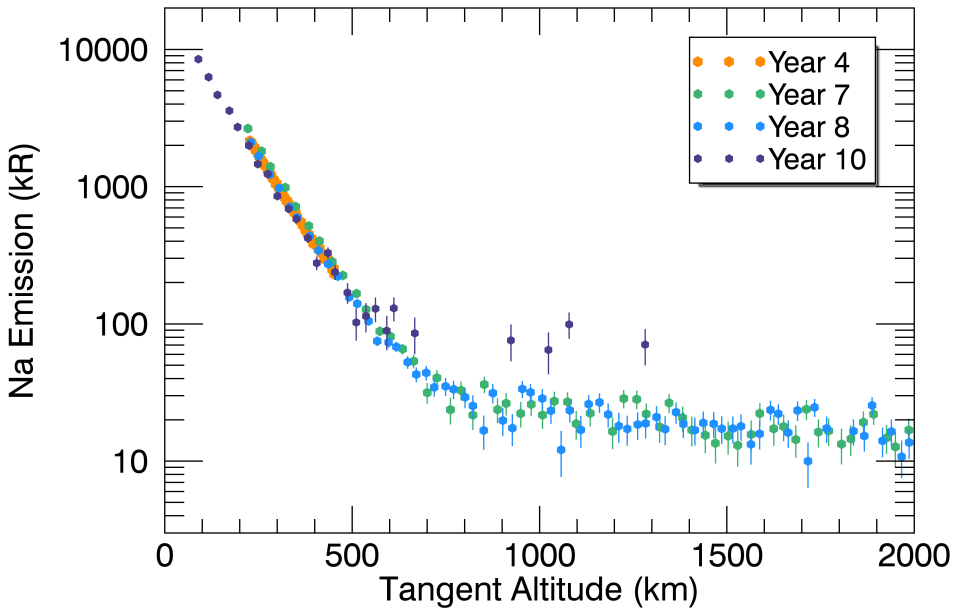

Figure 9. Altitude profiles of sodium emission observed above Mercury's subsolar point by the MESSENGER MASCS UVVS instrument. These were taken over several Mercury years (as indicated by the legend), but all were taken near the same true anomaly angle, between 65°–70° in this example. Although the sodium exosphere varies temporally, this figure highlights the seasonal repeatability of MASCS observations.

Some of the UVVS results are surprising in light of the decades of work published on Mercury's exosphere. In particular, ground observations (e.g. *Mangano et al.*, 2013, above) and models show a Na exosphere that is highly variable on the time scale of hours. These sudden changes are thought to be in response to changing solar wind and IMF conditions. UVVS observations do not show this. The species that were regularly observed (sodium, calcium, magnesium) look quite similar from one Mercury year to the next, at least wherever consistent observing geometries were used over long periods of time [*Burger et al.*, 2014; *Cassidy et al.*, 2015]. On the other hand, operational constraints have severely limited UVVS observations in the cusp, the most variable region. This may explain the differences, at least in part. Much of the UVVS data remains to be analyzed, so more progress on the variability of these exospheric species can be expected.

3.2.3 Plasma observations

3.2.3.1 Overall planetary ion composition and distribution

Plasma observations at Mercury began with the electron observations of Mariner 10 through three flybys in 1974–1975. Measurements from the first flyby convincingly showed Mercury to have an Earth-like interaction with the solar wind: There was a well-developed bow shock and a dense, hot plasma magnetosheath, surrounding a small magnetosphere [*Ogilvie et al.*, 1974]. Magnetometer measurements were compared with the plasma electron measurements and corroborated this interpretation [*Ness et al.*, 1974]. Within the magnetosphere, electrons were detected over the full energy range of the instrument, 13.4 – 687 eV, with a significant population in 200 – 680 eV range. These measurements were later

interpreted as being from a hot plasma sheet [*Ogilvie et al.*, 1977]. Several energetic electron bursts were detected by the energetic particle instrument [*Simpson et al.*, 1974; see also discussion in *Wurz and Blomberg*, 2001], though they were later re-interpreted as being due to > 36 keV electrons [*Armstrong et al*., 1975; *Christon et al.*, 1987]. *Siscoe et al.* [1975], *Baker et al.* [1986] and *Christon et al.* [1987] attributed these energetic bursts to substorms at Mercury. Fluxes and spectral shape of plasma electrons were observed to be partially correlated with these energetic bursts. A hardware failure in the plasma ion instrument prevented any ion observations by Mariner 10 [*Ogilvie et al.*, 1977]. Measurements from both flybys were combined with neutral atom measurements from the ultraviolet spectrometer [*Broadfoot et al.*, 1974, 1976] to infer that Mercury has no ionosphere, making the magnetosphere effectively bounded on the inside by the planet's surface.

The first plasma ion measurements at Mercury came with the first flyby of the MESSENGER spacecraft on January 15, 2008. The Fast Imaging Plasma Spectrometer (FIPS) [*Andrews et al.*, 2007] detected ions throughout the entire Mercury space environment, confirming predictions of their presence [*Zurbuchen et al.*, 2008]. Protons and alpha particles (He^{2+}) from the solar wind were observed as the spacecraft traversed the magnetosphere, with highest abundance in the magnetosheath. Many heavy ions were also detected, ranging in mass per charge (*m/q*) from 6–40 amu/e. These ions were found with highest abundance within the magnetosphere, with Na^+ (or Mg^+) ions dominating the heavy ion population. As Na is one of the dominant atoms in the exosphere and is easily ionized [*Wurz and Lammer*, 2003], these ions are generally taken to be Na^+, though the separation of Na^+ from Mg^+ ion has not yet been accomplished from FIPS data.

Once MESSENGER went into orbit around Mercury on March 18, 2011, the vast increase in the amount of data also necessitated a change in approach to a more automated approach of assigning counts to individual ion species that could be applied to the data in a largely automatic fashion. The main effect of this change was grouping of ions into ranges of *m/q*: O^+ group, *m/q* 14–20, including O^+ and any water group ions (e.g., H_2O^+, OH^+); Na^+ group, *m/q* 21–30, including Na^+, Mg^+ and Si^+. Substantially improved background removal was also accomplished in this new method, along with a much better estimation of signal to noise. The use of counts as measurement units was also replaced with a more physically relevant unit, the observed density (n_{obs}). This is the density computed from the counts measured, without any correction for those unobserved due to the limited FIPS field of view (FOV) on the three-axis stabilized MESSENGER spacecraft. These methods are explained in more detail in *Raines et al.* [2013].

A more complete picture of the distribution of ions in Mercury's space environment emerged from this much larger dataset. First, planetary ions were found throughout this space environment, both inside and outside of the magnetosphere. For the two most abundant species, Na^+-group and O^+-group ions, this distribution is not at all uniform. These ions show a very substantial abundance enhancement in the region of Mercury's northern magnetospheric cusp. Na^+-group and O^+-group ions are also very abundant in the nightside near-equatorial region, and often near high-latitude, dayside crossings of the magnetopause [*Zurbuchen et al.*, 2011]. Figure 10 shows this distribution, as a function of planetary latitude and local time, accumulated from 25 March 2011 through 31 December 2011. The different panels are accumulations over more than 500 orbits, indicating that these enhancements are very likely permanent features of Mercury's magnetosphere.

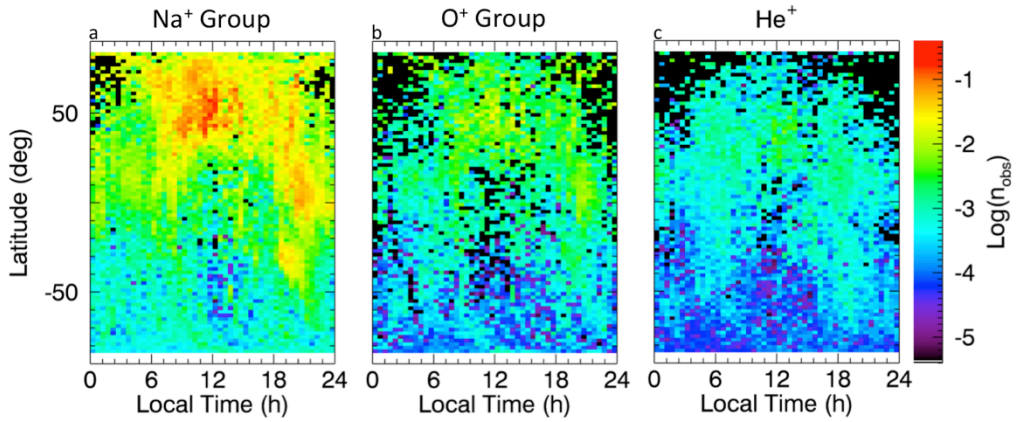

Figure 10. Na^+-group (a), O^+-group (b), and He^+ (c) ion observed density as a function of local time and planetary latitude. Observed density is averaged within each 0.5 h by 2° local time - latitude bin. Unobserved regions are colored white while observed regions with zero counts are coloured black. *Updated from Zurbuchen et al.* [2011].

In contrast to Na^+-group and O^+-group ions, He^+ is much more evenly distributed throughout the space environment [*Zurbuchen et al.*, 2011; *Raines et al.*, 2013]. This ion is present in the solar wind, but its enhanced abundance around the planet indicates that a significant fraction of its population comes from Mercury, either from the surface or exosphere. For example, He^+ has a distinct distribution from alpha particles (He^{2+}), not showing the magnetosheath enhancements very clearly observed in the doubly ionized He^{2+}. Very low plasma densities in Mercury's space environment make formation of He^+ from He^{2+} unlikely in any substantial quantities.

Of course, the distribution of planetary ions does not directly infer their sources. In the absence of a collisional atmosphere or ionosphere, the inner boundary of Mercury's magnetosphere is essentially the surface of the planet. Ions observed anywhere in this environment have been subject to the electromagnetic forces and processes of the magnetosphere, and their trajectories have been substantially affected. Furthermore, most of these processes are expected to be highly variable in time. One strategy employed for examining the relationship between observations and sources has been to look at the average behavior of ion distributions, hoping to find some commonality with the expected exosphere or surface sources. *Raines et al.* [2013] showed that the average observed density of Na^+-group and O^+-group ions varied substantially with true anomaly angle, the angle between Mercury and its orbital periapsis around its Keplarian orbit (Figure 2c of that work). He^+ ions showed a much less pronounced variation. These results were compared notionally with ground observations of the same variation of the exosphere. No clear correlation was apparent. In that same work *e*-folding heights of observed density versus altitude were computed for those same three planetary ion species, around three local times (dawn, noon and dusk). These heights showed substantial differences across local time and species, with the smallest height always at noon and those of Na^+ group ~2–6 times smaller than other ions. These ion *e*-folding heights are much larger, at least 5–10 times, than calculated scale heights for species of the neutral exosphere [*Wurz and Lammer*, 2003; *Wurz et al.*, 2010], likely confirming expectations that magnetospheric dynamics plays a substantial role.

3.2.3.2 Cusp

Mercury's magnetospheric cusps have long been thought to be major sources of planetary ions for its magnetosphere, primarily through the process of solar wind sputtering [*Lammer et al.,* 2003*; Leblanc and Johnson,* 2003, 2010*; Massetti et al.,* 2003]. As discussed above, the abundance of planetary ions is largest there [*Zurbuchen et al.*, 2011; *Raines et al.*, 2013]. The cusps, however, are very active, and dynamic regions at Mercury, so a more detailed analysis was required to connect observed ions to cusp sources.

Raines et al. [2014] performed such a study of Mercury's Northern cusp region. Focusing on Na^+-group ions and protons, these authors selected 77 cusps with significant Na^+-group ion content from 518 orbits, spanning observations from September 2011 through May 2012. They examined ion flow directions, energy-resolved pitch angle, energy and spatial distributions for these two species. Their main result was that Na^+-group ions in Mercury's cusp are too high in energy (2.7 keV on average) to be produced locally in the cusp. They also found a regular occurrence of keV-energy Na^+-group ions flowing northward in the dayside magnetosphere. From these measurements, the authors hypothesized that neutral Na atoms were ionized in the vicinity of the subsolar magnetopause and accelerated into the cusp by reconnection. This process may constitute a significant source of keV-energy planetary ions in Mercury's magnetosphere.

Two other interesting results emerged from this work, both of which can be more easily seen from energy-resolved pitch angle distributions. These plots (Figure 11), which show the flow direction of ions relative to the magnetic field, are particularly interesting in the cusp because the magnetic field is largely radial there. This means that ions traveling in the anti-parallel magnetic field direction are effectively headed away from the surface, while those parallel ions are headed toward the surface. The energy-resolved pitch angle distribution for protons (Figure 13) shows a distinct depletion in flux coming up from the surface (anti-parallel, left side of figure), when compared with the flux going down toward the surface (parallel, right side of figure). This asymmetry likely results from the fact that a fraction of protons traveling toward the surface are lost to surface precipitation, rather than being reflected in the increasing magnetic field there. This loss cone appears to be >40° and constitutes a strong indication that protons are impacting Mercury's surface in the cusp. The opposite is observed for Na^+-group ions (Figure 10e): At energies of 100–300 eV, they are enhanced in the anti-parallel direction and therefore appear to be streaming out of the cusp. This is also visible as a small bump in the anti-parallel phase space density shown in the left half of Figure 10f. Taken together, these two results may constitute a cause and effect observation of solar wind sputtering at Mercury, though some additional explanation of Na^+-group acceleration is required. Several studies provided a more quantitative look at proton precipitation at the cusp. Those are reviewed in Section 4.3.1.

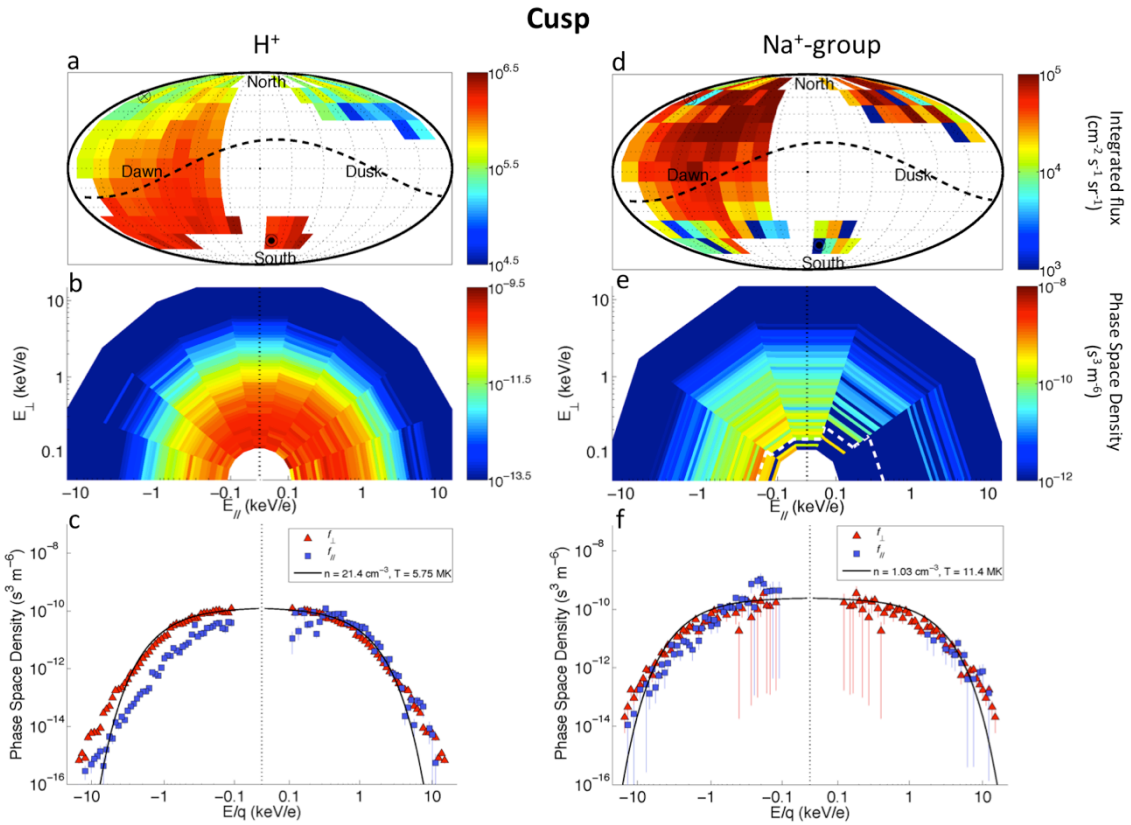

Figure 11. Kinetic properties of protons and Na^+-group ions within the cusp, accumulated over 77 cusp crossings. Top panels (a, d) show flow direction histograms for protons and Na+-group ions. The middle panels (b, e) are energy-resolved pitch angle distributions, which show the flow direction and energy of ions relative to the magnetic field in 20° (protons) and 36° (Na^+-group) bins. Slices through these distributions in the parallel, anti-parallel and perpendicular directions are shown in the bottom panels (c,f). These figures show protons which are flowing down toward the surface, as well as loss cone of >40° in width. Low energy (100-300 eV) Na+-group ions appear to be upwelling from the surface, while those at energies up to 10 keV have large perpendicular energy components. *Reproduced from Raines et al. [2014].*

3.2.3.3 Central Plasma Sheet

A large collection of data from the orbital phase showed that average plasma sheet densities were in line with those observed in the first flyby, though average temperatures were higher [*Gershman et al.*, 2014]. In addition to values for protons, average density and temperature were also reported for alpha particles and Na^+-group ions (Table 1), giving a good average picture of plasma sheet ions for consideration by other studies. The estimated pressure contribution from plasma sheet protons was found to be in good agreement with the observed magnetic depressions there [*Korth et al.*, 2011], providing an independent validation of these recovered plasma parameters.

Species	Density (cm^{-3})	Temperature (MK)
H^+	7.81	9.29
He^{2+}	0.265	30.3
Na^+-group	0.663	15.7

Table 1. Average kinetic properties in the central plasma sheet. From *Gershman et al.*, 2014.

One of the most interesting results from *Gershman et al.* [2014] comes from the relative temperatures of plasma sheet ions (Figure 12). For solar wind ions, alpha particles and solar wind heavy ions (mostly O^{6+} and C^{5+}), the ratio of their temperature to that of protons is mass-proportional, i.e., $T_i/T_{H^+} = m_i$. This is expected for ions that are accelerated to the same speed, as is often the case in the solar wind and reconnection outflow. However, planetary Na^+-group and O^+-group ion temperatures show a roughly constant ratio to protons, as if they were accelerated through a potential. This may result from them having gyroradii which are large compared to plasma sheet magnetic field gradients, so that their motion in the plasma sheet is dominated by the cross-tail electric field. This result is consistent with findings by *Raines et al.* [2013] that Na^+-group ions are substantially enhanced in the pre-midnight plasma sheet when compared to the post-midnight side. These may both be observational evidence of the expected non-adiabatic behavior of heavy ions at Mercury, a point to which we return in some detail below.

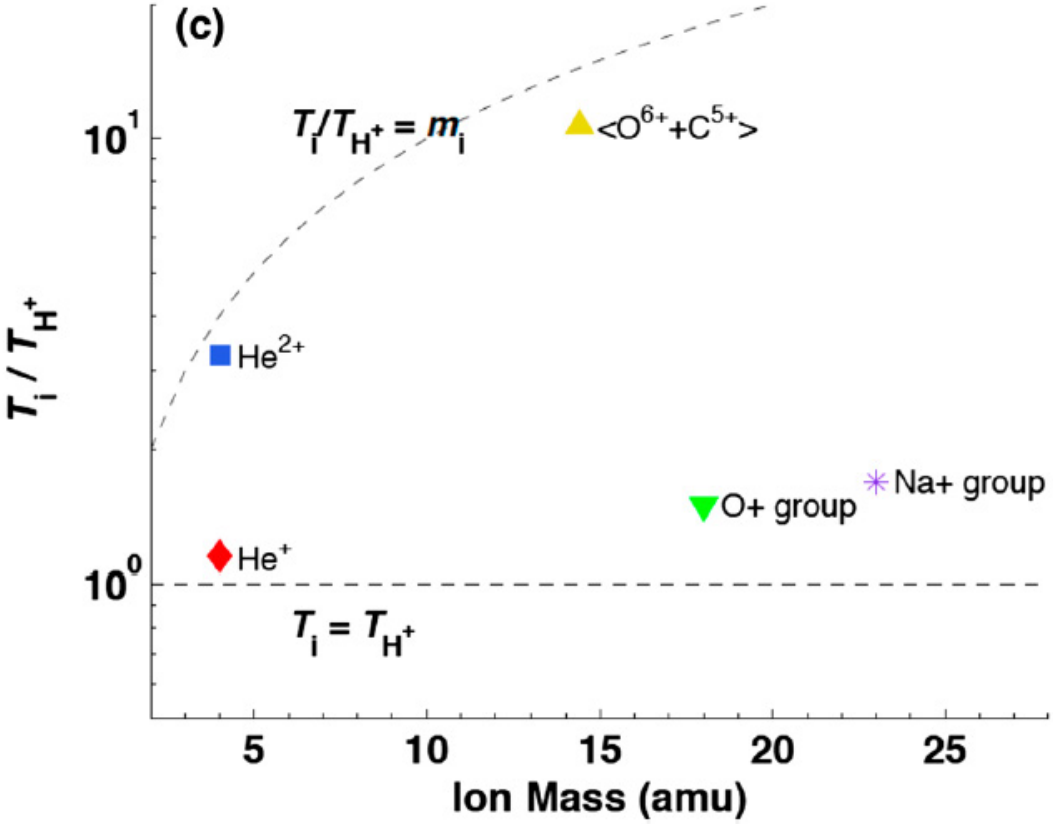

Figure 12. (a) Average temperature T_i of each species relative to that of H^+. Dashed lines corresponding to T_i/T_{H+} = mi are also shown.

4 Losses

There have been no studies of MESSENGER data focused on computing plasma loss rates from Mercury's magnetosphere. Estimating these rates from single spacecraft measurements of a highly dynamic system requires tightly coordinated and well-calibrated combination of models and data that has not yet been achieved. Work is heading in that direction, as described below in Section 5.1.2, so it is likely the

plasma loss rates will be derived in the near future. Studies of several magnetospheric processes that contribute to plasma loss are described below.

4.1 Observations of plasmoids and TCRs

Loading of the tail lobes and magnetopause flaring lead to thinning of the plasma sheet and its embedded cross-tail current layer for reasons that are still not well understood [*Kuznetsova et al*., 2007; *Winglee et al.,* 2009; *Raeder et al.,* 2010]. When the current sheet thins, the normal magnetic field component is sufficiently reduced such that it becomes unstable to reconnection. A fundamental aspect of the reconnection process is the formation of magnetic islands with helical or quasi-loop-like topologies in the cross-tail current layer [*Hesse and Kivelson*, 1998]. These magnetic structures are called "plasmoids" [*Hones et al*., 1984]. Similar to the FTEs at the magnetopause (Section 3.1.2), the lobe magnetic field becomes draped and locally compressed about the plasmoid, which can be observed as TCRs [*Slavin et al.,* 1993]. Because TCRs can be observed over a large fraction of the lobe region they are observed far more frequently than the underlying plasmoids that occupy a much smaller volume. Plasmoids and TCRs are highly correlated with the onset of magnetospheric substorms [*Slavin et al.*, 1992; *Moldwin and Hughes*, 1992]. Many flux rope- or magnetic loop-like plasmoids can be formed during a given reconnection event, with some being carried sunward and others tailward by the fast Alfvénic jetting of plasma away from reconnection X-lines [*Slavin et al.,* 2003]. Indeed, initial

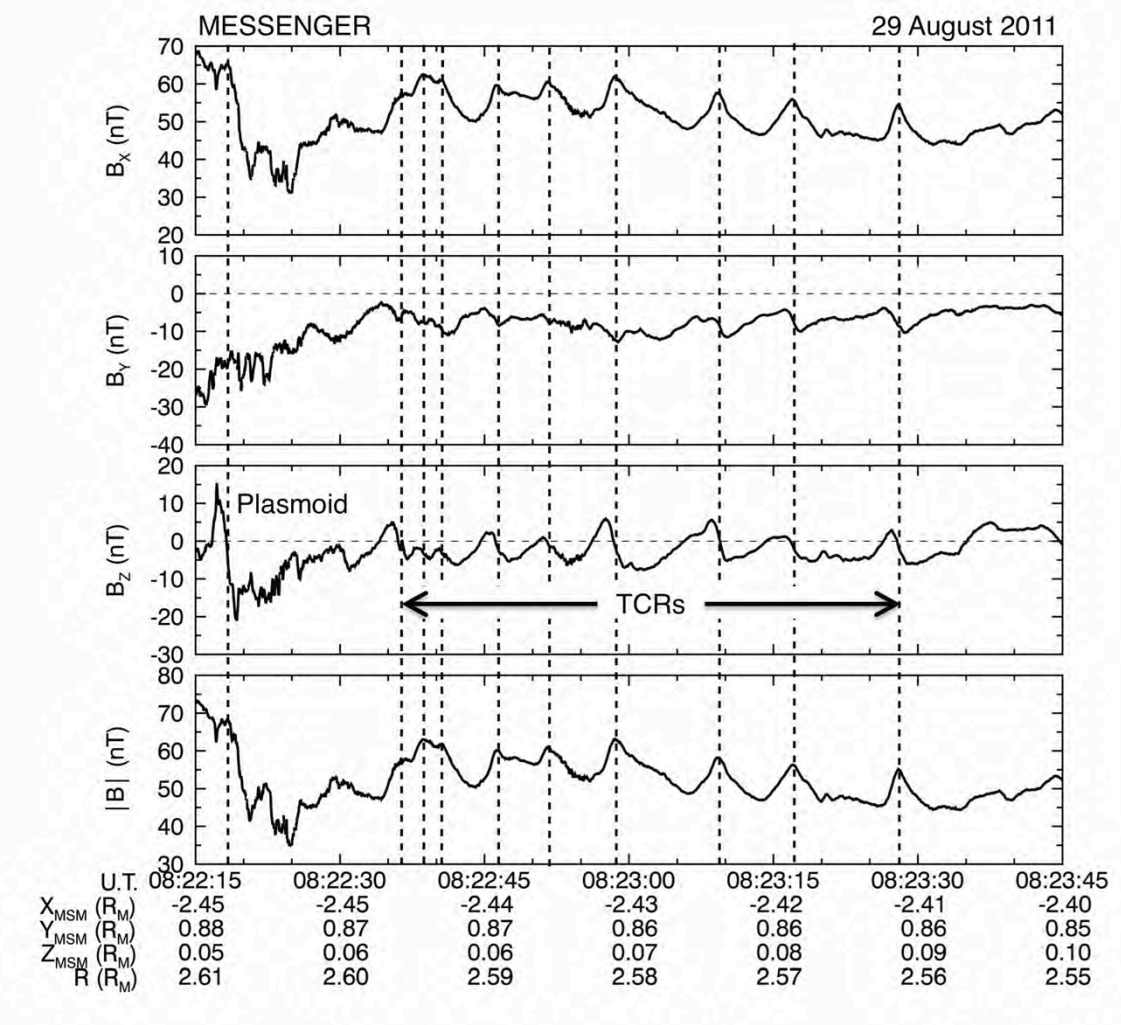

Figure 13. Quasi-periodic plasmoids and TCRs observed during the orbital phase of the MESSENGER mission are marked with vertical dashed lines.

analyses of the MESSENGER measurements have revealed the presence of sunward- and anti-sunward-moving plasmoids and TCRs [*Slavin et al.,* 2009, 2012a].

Figure 13 displays a 90 sec-long interval on 29 August 2011 when MESSENGER had just entered the north lobe of the magnetotail ~ 2.4 R_M downstream of Mercury. The interval starts at 08:22:19 UTC with the spacecraft encountering a plasmoid. It is identified by the ~ 1.5 sec-long, large amplitude, north-then-south B_Z perturbation followed by a ~ 6 sec interval of weaker magnetic field with a southward orientation and higher frequency fluctuations. The plasmoid is then followed by a series of 9 traveling compression regions, which are similarly characterized by ~ 1 – 2 sec north-then-south B_Z perturbations with a recovery period of ~ 5 sec. However, the TCRs differ in that they are strongly correlated with 10 – 15% enhancements in the total magnetic field intensity. The absence of higher frequency fluctuations and the steady sunward orientation of the magnetic field indicate that all of these events take place in the northern lobe of the tail.

These observations are remarkably similar to the plasmoid and TCR events observed during the second flyby [*Slavin et al.*, 2009]. MESSENGER does not have the capability to measure the plasma flow during these events, but the mean ejection speed for plasmoids in the Earth's near-tail is ~ 500 – 600 km/s [*Ieda et al.,* 1998; *Slavin et al*., 2003]. If we assume a speed of 500 km/s for these plasmoid and TCR events at Mercury, then the average diameters of these structures at Mercury are ~ 500 km, or 0.2 R_M. This compares with ~ 1 to 3 R_E plasmoid diameters in the near-tail of Earth [*Slavin et al.*, 2003]. Given the factor ~ 8 scaling between the dimensions of these two magnetospheres, the diameters of plasmoids at these two planets appear to take up similar relative volumes at Mercury and Earth. It should also be noted that "chains" of plasmoids and TCRs, such as displayed in Figure 13, are also common at Earth [*Slavin et al.*, 1993, 2005; *Imber et al.*, 2011]. What is still not understood is whether these chains form simultaneously due to reconnection at multiple X-lines, as sometimes observed in simulations of ion tearing-mode reconnection [*Schindler*, 1974; *Tanaka et al.,* 2011] or to periodic episodes of reconnection at a smaller number of X-lines. Interestingly, the mean interval of 9 sec between the plasmoid and TCR events in Figure 13 is very close the ~ 8 – 10 sec spacing between flux transfer events observed at Mercury by *Slavin et al.* [2012b].

In a statistical survey of 49 flux rope-like plasmoids in Mercury's magnetotail, observed between 1.7 R_M and 2.8 R_M down the tail from the center of the planet, *DiBraccio et al*. [2014] analyzed MESSENGER MAG and FIPS orbital data to determine the average characteristics of these structures. A superposed epoch analysis of the plasmoid-type flux rope events with north-then-south Bz pertubations, consistent tailward motion, from DiBraccio et al. is displayed in Figure 14. The magnetic field shows the characteristic variation expected for this type of flux rope [Slavin et al., 2003]. In particular the strong core magnetic field in the +/- Y direction centered on the bi-polar Bz variation associated with the outermost wraps of magnetic flux. DiBraccio et al. concluded that This study concluded that the typical plasmoid diameter was ~345 km, or ~0.14 R_M, which is comparable to a proton gyroradius in the plasma sheet, or ~380 km. The events in this survey demonstrated that the magnetic variations of flux ropes at Mercury are similar to those observed at Earth but with timescales that are 40 times shorter at Mercury.

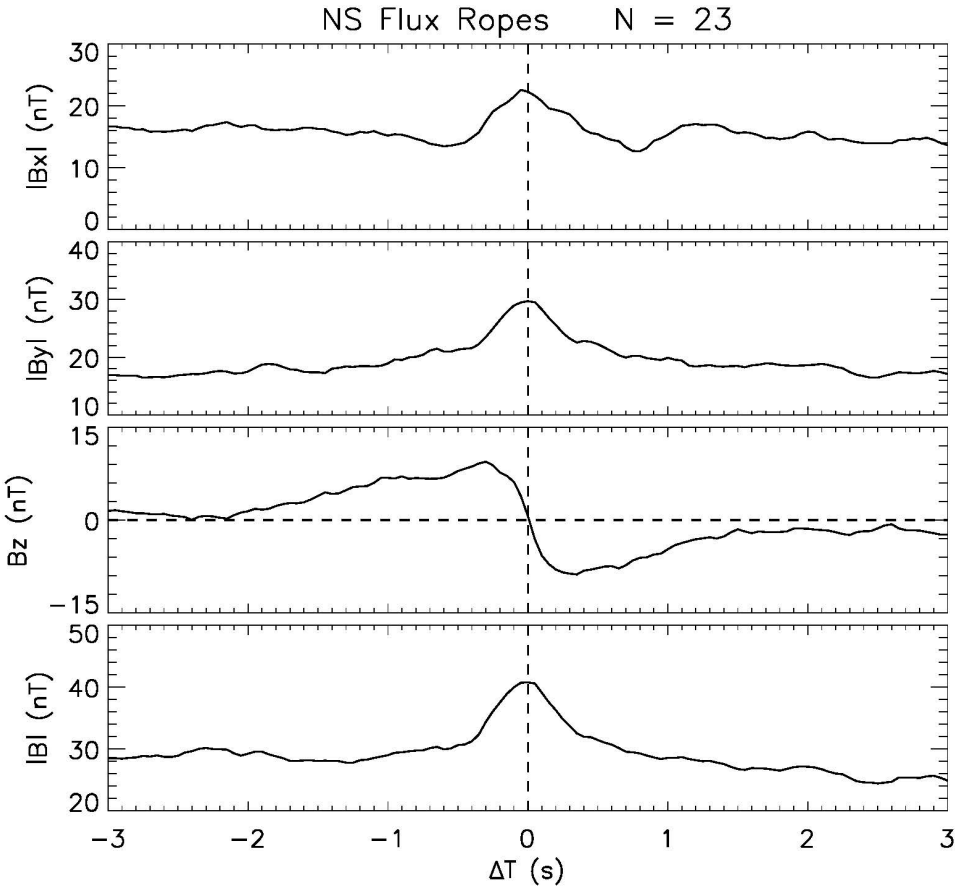

Figure 14. Superposed epoch analysis of the magnetic fields measured during 23 plasmoid-type flux ropes in Mercury Solar Orbital coordinates [from DiBraccio et al., 2014]. Note the strong core magnetic field coincident with the bipolar variation in the Bz perturbation. The continued negative Bz following the plasmoid is due to continued reconnection involving lobe magnetic flux after the plasmoid is released as observed at Earth.

4.2 Observations of dipolarization

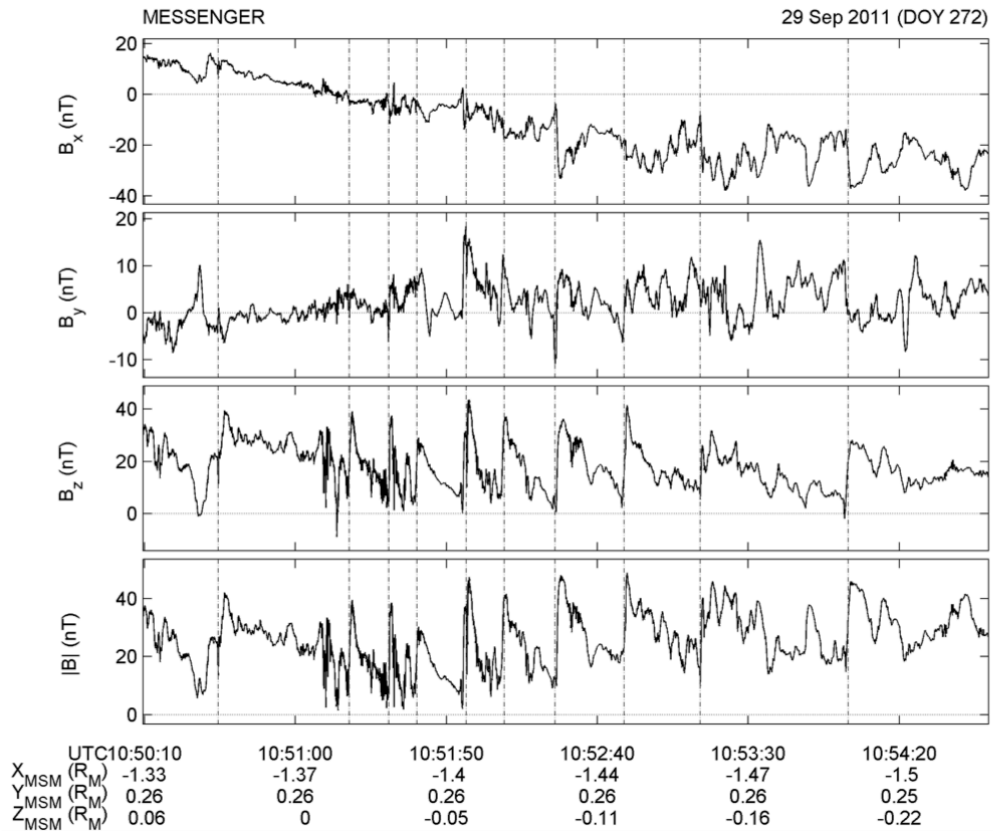

Figure 15. A series of dipolarizations of the magnetic field in the plasma sheet observed by MESSENGER and analyzed by Sundberg et al. [2012]. These brief, several second-long events are marked by vertical dashed line. Each has sudden, strong transitions from the magnetic field being highly stretched to a more dipolar configuration with a greatly enhanced Bz component.

An integral step in the substorm process is dipolarization of the fields in the near-tail [*Baker et al.*, 1996]. The transient increases in the northward, or dipolar, component of the equatorial magnetic field are closely associated with the braking of sunward directed bursty-bulk flows originating at reconnection X-lines in the magnetotail [*Angelopoulos et al.*, 1994]. This is most readily understood as the result of the reconfiguration of the magnetotail into a lower energy state in which the stretched field lines created by the tail loading process quickly return to a more dipolar configuration [*Shiokawa et al.*, 1997]. At Earth these propagating dipolarization fronts are often accompanied by enhanced ion and electron fluxes up to hundreds of keV due to betatron acceleration as the magnetic field intensity increases [*Ashour-Abdalla et al.*, 2011].

Earth-like dipolarization events were first observed at Mercury by Mariner 10 during it first flyby in 1974 [*Baker et al.*, 1986; *Christon et al.*, 1987]. The observed magnetic field signatures were in good agreement with those expected from terrestrial dipolarization events, but with durations only of order 1 to 10 sec as opposed to tens of min at Earth. Figure 15 displays an example of dipolarization events at Mercury on 29 September 2011 that have been analyzed by *Sundberg et al.* [2012]. As shown, a series of 10 dipolarizations are seen to occur during a single plasma sheet encounter of several minutes at a distance of ~ 1.4 R_M downstream of Mercury's terminator plane. The dipolarization events, marked by dashed lines, are evident in the rapid (~ 1 sec) increases and slow (~10 s) decays in the B_Z component of the magnetic field. The amplitudes of the magnetic field increases are 40–50 nT, similar to such events at

Earth [*Runov et al.*, 2011]. The relatively short lifetime of the events is attributed to fast decay of the field-aligned currents that must accompany such dipolarizations. At Earth these currents close through an ionosphere with a conductance that is expected to be one or even two orders of magnitude larger than that of Mercury's regolith. The recurrence rate is generally in good agreement with those of plasmoids and traveling compression regions discussed previously.

4.3 Precipitation

4.3.1 Loss cone determination

Several studies provided a more quantitative look a proton precipitation at the cusp. Mapping of plasma pressures to invariant latitude [*Korth et al.*, 2014] showed a clear north-south asymmetry on the nightside. This indicated increased particle loss through precipitation in the southern hemisphere, as anticipated from larger cusp that is created there by the northern offset of the planetary dipole. *Winslow et al.* [2014] used FIPS data to provide the first quantitative estimates of Mercury's loss cones and, from those, estimates of the surface fields in the cusp regions. In that work, self-normalized pitch angle distributions were summed over many cusp passages and then fit to an equation for pitch angle diffusion. The best-fit solutions gave loss cones of $121° \pm 3°$ for the northern cusp and $47°^{+7}_{-13}$ in the southern cusp. The locations of the cusps were also mapped assuming an offset dipole field down from the spacecraft altitude to the surface. The northern cusp was found to be centered around 76.4° N latitude and noon local time, with a 15.6° extent in latitude and 7.5 h extent in local time. In the southern hemisphere, the cusp observations mapped to 23° - 34° S latitude and 16 – 5.3 h local time. MESSENGER's orbit restricted the observation of the southern cusp to latitudes north of 30° S latitude, so uncertainties in the southern hemisphere are larger.

4.3.2 ULF waves

Ultra-low frequency (ULF) waves were first detected in Mercury's magnetosphere by Mariner 10 [*Russell,* 1989]. Aside from acting as an important mechanism of energy transfer, these waves can increase plasma losses by scattering them into the loss cone. During the first MESSENGER flyby, *Slavin et al.* [2008] detected ULF waves in the magnetic field data between closest approach and the outbound magnetopause crossing with frequencies of ~0.5 to 1.5 Hz. *Boardsen et al.* [2009] performed a detailed analysis of these waves and found their fundamental mode was at frequencies between the He^+ and H^+ cyclotron frequencies (Figure 16). *Boardsen et al.* [2009] concluded that wave frequency and amplitude increased from closest approach to the edge of a boundary layer located adjacent to the magnetopause; however, the frequency decreased by a factor of two and the amplitude increased by an order of magnitude inside the boundary layer.

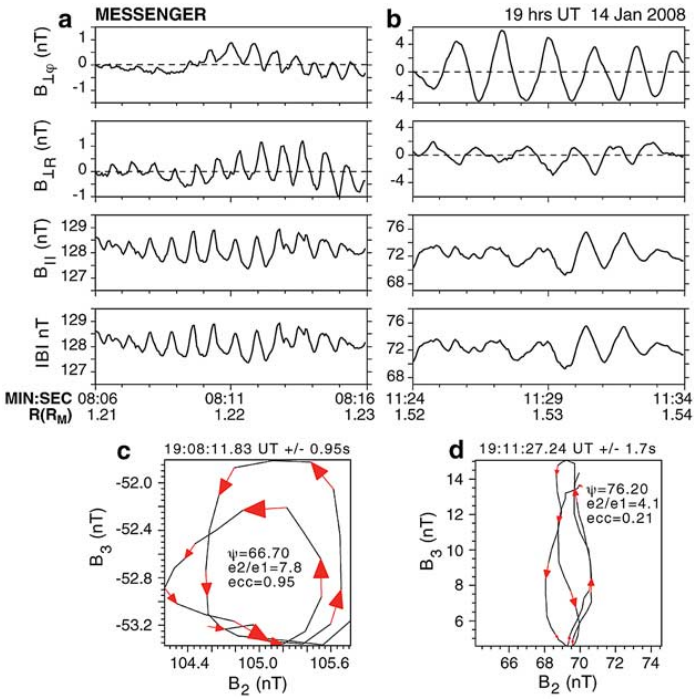

Figure 16. (a) Time-series examples of ULF waves detected outbound from closest approach. (b) Example ULF waves. Hodograms of the time series shown in Figures (c) 2a and (d) 2b. Axes B_2 and B_3 are the directions of intermediate and maximum variance, respectively. The wave-normal angle (Ψ), ratio of median to minimum eigenvalue (e2/e1) and ellipticity (ecc) are given for each hodogram. *Adapted from Boardsen et al.,* [2009].

Also inside Mercury's magnetosphere, *Boardsen et al.* [2012] surveyed coherent ULF waves at frequencies between 0.4–5 Hz. They were observed at the inner magnetosphere ($R < 0.2\ R_M$) at all MLTs. The waves are observed to be compressional and at maximum power near the equator on the nightside (Figure 17), and become transverse with power decreasing for increasing magnetic latitudes. On average, the waves are strongly linear with wave-normal angles peaked around 90 deg and elliptical values < 0.3.

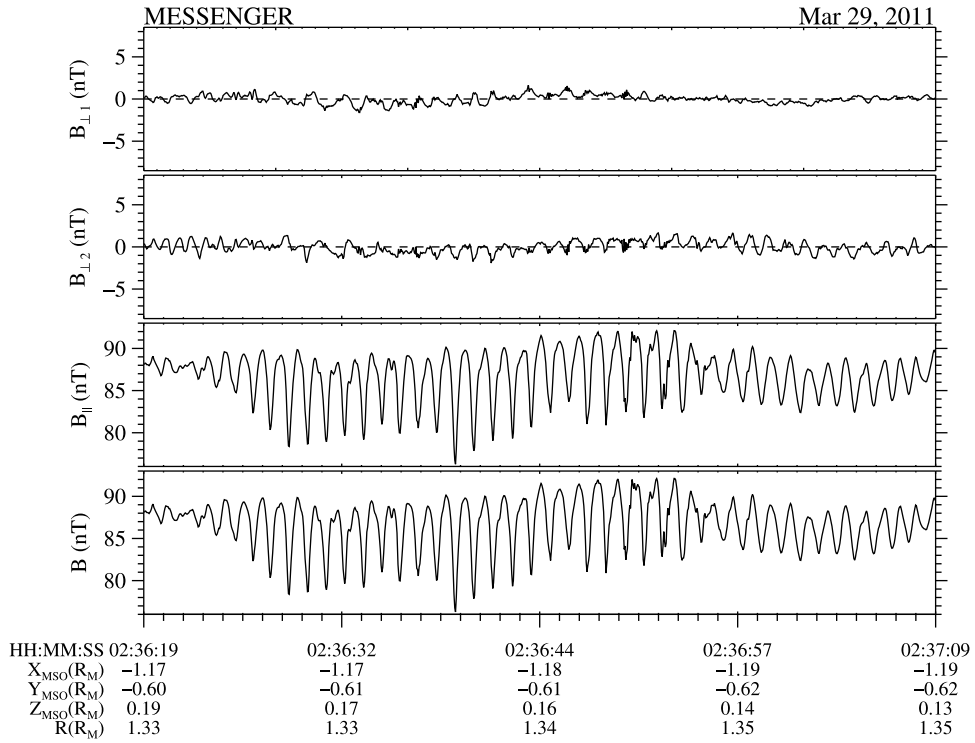

Figure 17. Strongly compressional waves near Mercury's magnetic equator. Perpendicular components of the field from two-dimensional MVA are shown in the first (minimum perpendicular variance) and second (maximum perpendicular variance) panels. The third panel is the parallel field component and the fourth panel is the field magnitude. Peak-to-peak amplitudes are 10 nT. *Adapted from Boardsen et al.* [2012].

5 Modeling

5.1 Global Modeling of Mercury's Magnetosphere

5.1.1 MHD and hybrid models of Mercury's magnetosphere

Global simulation models have been developed and applied to Mercury to understand the solar wind-magnetosphere interaction. These global models provide global context for interpreting and linking measurements obtained in various parts of the system, thereby extending our knowledge of Mercury's magnetospheric environment beyond that available from localized spacecraft observations. Two types of simulation models have been widely used in the global modeling of Mercury's magnetosphere, i.e., magnetohydrodynamic (MHD) simulation and hybrid simulation.

Global MHD simulation, in which both ions and electrons are treated as fluid, usually can provide a description of the global interaction over a reasonably large region around the obstacle and with relatively high resolution at a feasible computational cost. MHD models have been used to characterize the large-scale structure of Mercury's magnetosphere under various solar wind and IMF conditions. For example, *Kabin et al.* [2000] employed a single-fluid MHD model to characterize the configuration of Mercury's magnetosphere under extreme solar wind dynamic pressure conditions. *Ip and Kopp* [2002], also using a global MHD model,

investigated the response of Mercury's magnetospheric configuration to different IMF orientations focusing particularly on the size of the polar caps, through which the solar wind particles can gain access to Mercury's surface. Recent MHD modeling efforts have been made to extend single-fluid MHD to multi-fluid MHD models. *Kidder et al.* [2008] adapted a multi-fluid model to Mercury that tracks the solar wind protons and planetary ions of Mercury origin as separate fluids, allowing for studying the effects of planetary heavy ions on the global magnetospheric structure. *Benna et al.* [2010] applied a two-fluid, Hall-MHD model in which the ion and electron fluids are treated separately with the inclusion of the Hall physics within the ideal MHD framework.

Another type of global simulations frequently used in the modeling of Mercury's magnetosphere is the hybrid model in which electrons are treated as a massless fluid while ions are represented as individual macro-particles. This allows for modeling ion kinetic effects, e.g., finite gyroradius effects and non-Maxwellian particle distributions. Compared to MHD simulation, hybrid simulation normally needs relatively expensive computational resources to achieve reasonably good resolution and to reduce system noise. With the rapid increase of computing power, it has recently become viable to apply a three-dimensional hybrid model to simulate Mercury's magnetosphere on a global scale [e.g., *Kallio and Janhunen*, 2003; *Travnicek et al.,* 2007, 2010; *Wang et al.*, 2010; *Müller et al.,* 2012; *Richer et al.*, 2012]. These hybrid simulations have provided significant insights into many of the fundamental plasma processes operating in Mercury's magnetosphere, especially those on the ion kinetic scale, such as energy-dependent particle drifts and wave generations resulting from ion temperature anisotropy.

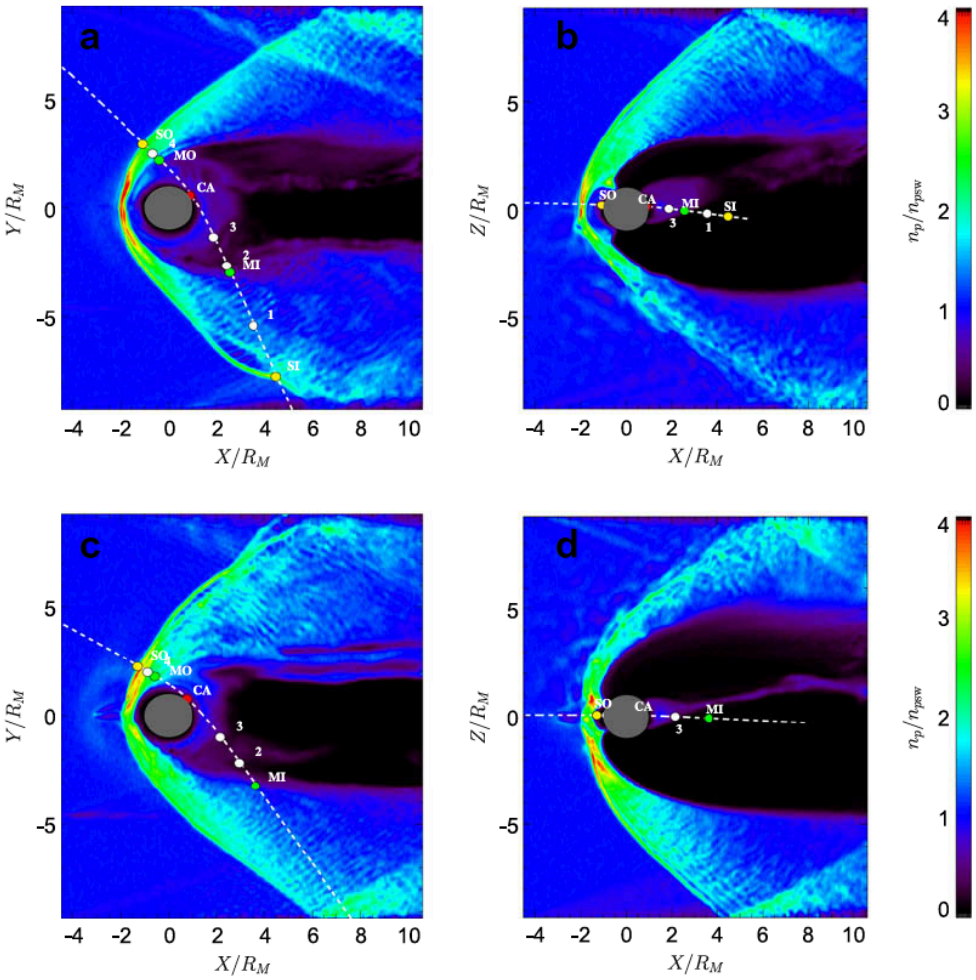

Figure 18: Simulated magnetospheric configuration from the global hybrid model of *Travenick et al.* (2010). Panels (a) and (b) show the simulated solar wind proton density in the equatorial and noon-midnight meridional planes, respectively, under northward IMF conditions. Panels (c) and (d) are the same but for southward IMF. Colors in each panel represent the density of solar wind protons normalized to the upstream value. MESSEGER trajectories of the M1 and M2 flybys are superimposed as white dashed lines.

5.1.1.1 Solar wind entry into the magnetosphere

Various modeling studies using global MHD and hybrid simulations have in general confirmed the picture of Mercury's magnetosphere derived from measurements, that reconnection is the dominant process transferring solar wind plasma and energy into Mercury's magnetosphere. Modeling has also shown that other boundary processes, such as the Kelvin-Helmholtz instability [*Paral and Rankin*, 2013] and ion kinetic motion across the magnetopause due to finite gyroradius effect [e.g., *Müller et al.*, 2012], also contribute to the transfer of magnetosheath plasma into the magnetosphere as observed by MESSENGER. As an example, Figure 18 shows the large-scale configuration of Mercury's magnetosphere from the hybrid model of *Travenick et al.* [2010]. Familiar magnetospheric structures can be readily identified in the figure, such as the bow shock, magnetosheath, cusps, tail lobes and plasma sheet. Several modeling studies based on MHD and hybrid simulations have found that Mercury's magnetosphere changes its configuration

considerably when the IMF orientation varies. In particular, as shown in Figure 18, the dayside magnetopause is located closer to the planet during southward IMF compared to northward IMF [e.g., *Ip and Kopp*, 2002; *Kidder et al*., 2008; *Travenick et al.*, 2010], consistent with the suggestion by *Slavin and Holzer* [1979] that enhanced low-latitude reconnection during periods of southward IMF can effectively erode the dayside magnetopause causing the boundary to move closer to the planet's surface. Correspondingly, the location and morphology of the cusps, through which the solar wind plasma can gain access to the low altitude region, also vary in response to solar wind and IMF changes. As described above, however, analysis of MESSENGER data [e.g., *DiBraccio et al*., 2013] does not support the strong bias of reconnection rate based on IMF direction alone. This behaviour has not yet been captured in global models of Mercury's magnetosphere.

Aside from the IMF, solar wind dynamic pressure is another important factor that can significantly affect the size and configuration of Mercury's magnetosphere. *Kabin et al.* [2000] using an MHD model simulated Mercury's interaction with the solar wind for different upstream pressures. They showed that under extremely high solar wind dynamic pressure conditions Mercury's dayside magnetopause can be pushed all the way to the surface, a situation in which the solar wind plasma can directly impinge on the planet. Similar results have also been found in the hybrid simulation by *Kallio and Janhunen* [2003]. However, results from MESSENGER observations paint a more nuanced picture: *Slavin et al.* [2014] found that increases in magnetic field due to induction in the planet's core act to resist this compression, where the resulting stand-off distance is the result of competition between these two processes. Some models now included this induction (Section 5.1.1.3 below).

5.1.1.2 Precipitation of solar wind particles onto Mercury's surface

Once the solar wind enters the magnetosphere, the bulk of the plasma follows the large-scale Dungey cycle magnetospheric convection driven by the solar wind. Since precipitation of solar wind particles onto Mercury's surface is a major of its exosphere and magnetosphere, it is of high interest to derive from global magnetosphere models quantitative information about this process as well as its dependence on the internal and external conditions.

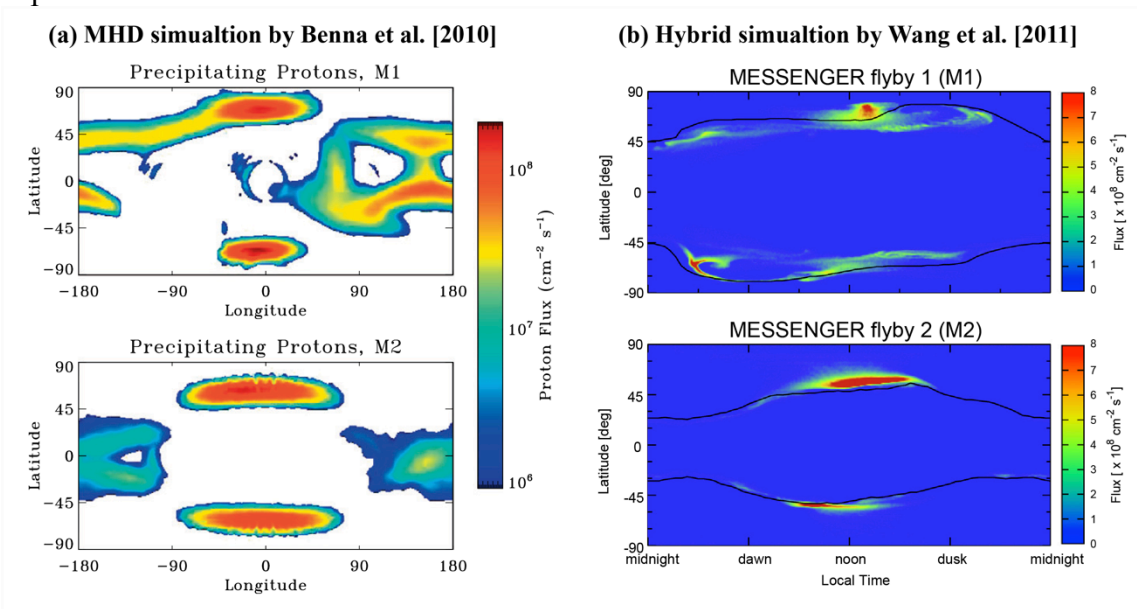

Figure 19. Maps of precipitating solar wind proton fluxes (in the unit of particles per cm^2 per

second) predicted by global magnetosphere simulations for the MESSENGER M1 and M2 flyby conditions. (a) From the MHD model by *Benna et al.* [2010] (figure adapted from *Burger et al.,* 2010). (b) From the hybrid model by *Wang and Ip* [2011]. For each model, the top panel shows the precipitation map for the M1 flyby conditions while the bottom panel is for the M2 flyby.

Figure 19 shows maps of the solar wind precipitation onto Mercury's surface as predicted by MHD and hybrid simulations for the first two MESSENGER flybys. It should be noted that the two simulation models discussed here used different modeling approaches (MHD versus hybrid) and differ in many aspects, such as the input parameters and details of the numerical codes. Nevertheless, the two models give qualitatively similar results on the general features of ion precipitation. In general, there are two main regions on the surface to which solar wind particles can have access. One is the cusp region on the dayside and the other is the low-latitude region on the night side. As mentioned above, the location and size of the two cusps responds to IMF changes. This can be clearly seen by comparing the precipitation maps between the cases for the M1 (northward IMF) and M2 (southward IMF) flybys. The peak fluxes are centered above 70 degree latitude for the M1 flyby conditions whereas they move equatorward to about 65 degree latitude for the M2 flyby conditions, which is in accordance with the variation of the open-closed field line boundary as shown in the hybrid case (Figure 19(b)). Both models predict a noticeable north-south asymmetry in the impact rate and the spatial distribution of the cusp precipitation. Such an asymmetry has been suggested to arise from the presence of a strong B_X component in the IMF [*Sarantos et al.,* 2001], a typical feature of the Parker spiral at Mercury's orbit. *Benna et al.* [2010] attributed a north/south asymmetry in the sodium density observed during a MESSENGER flyby to this precipitation flux asymmetry. Others have also invoked ion flux to help explain sodium exosphere observations via the processes of ion sputtering, ion-enhanced diffusion, and chemical sputtering, as in the Monte Carlo models of *Mura et al.* (2009*), Leblanc and Johnson* (2010), and *Burger et al.* (2010). In later work, the north/south asymmetry in precipitation was attributed mostly to Mercury's offset magnetic dipole [e.g. *Winslow et al.*, 2014].

Ion precipitation is seen on the night side mainly at low latitudes where the magnetic field lines are closed field lines with both ends connected to the planet. The existence of such an ion impact region is consistent with the expectation that Mercury's plasma sheet ions have relatively large loss cone [*Korth et al.,* 2014] because of the planet's weak intrinsic magnetic field. While the MHD and hybrid models show similar features of the cusp precipitation, the nightside precipitation appears to have different characteristics between the two models. The MHD model predicts a broad region of ion precipitation on the night side, which has been attributed to the absorption of particles in the drift belt formed in the equatorial region. Hybrid models, on the other hand, also predict the existence of such a drift belt near the planet [e.g., *Travenick et al.*, 2010]. However, a surprising result of the hybrid simulations [e.g., *Travenick et al.*, 2010; *Wang et al.*, 2011] is that those ions precipitate onto the surface primarily at high latitudes, instead of near the equator as one might expect on the basis of finite gyroradius effect.

In addition to the external conditions, the internal conditions, such as the magnetic properties of the planet, may also affect the distribution of ion precipitation onto the surface. *Richer et al*. [2012] using a hybrid model explored the sensitivity of the global magnetospheric interaction to details of Mercury's intrinsic magnetic field. Two different internal field representations were used in their simulations: one

contains a northward offset dipole [*Anderson et al.*, 2011] and the other is a combination of a centered dipole and quadrupole fitted to the offset dipole derived from MESSENGER observations. They found that while the two internal field models yielded similar magnetic configuration in the northern hemisphere, the north-south asymmetry is more pronounced in the case with the a dipole plus a quadrupole field. This leads to very different precipitation patterns between the northern and southern hemispheres, an interesting result that needs to be checked against with observations of the low-altitude region of the southern hemisphere from future missions to Mercury, such as the BepiColombo mission.

5.1.1.3 Simulation of the induction effect arising from the planetary core

There is no doubt that the electromagnetic coupling between the planetary interior and the magnetosphere is an important element of Mercury's interaction system that needs to be included in global modeling, especially when considering the system response to time-varying external conditions. Most the global models applied to Mercury thus far excluded the planetary interior from the simulation domain. In those models, the electrical properties of the planet are mimicked through prescription of boundary conditions. To properly model the coupling between the magnetosphere and the core, it is desirable to explicitly include the planetary interior as part of the simulation domain. Such an attempt has been undertaken by *Müller et al*. [2012], who adapted a 3D hybrid model previously applied to planetary moons to Mercury and included the planetary interior with a specified conductivity distribution. The model has been applied to simulate MESSENGER flybys and shown to reproduce MESSENGER observations reasonably well. However, the induction effect arising from the core was not clearly demonstrated because the model employed steady solar wind conditions as input and focused on the steady-state behavior of the magnetosphere, as what has been done with most global models applied to Mercury. *Jia et al.* [2013] recently developed a global resistive MHD model that also explicitly includes the planetary interior with layers of different conductivities in their simulation. To characterize how the coupled system dynamically responds to the external forcing, they drive the simulation by using time-dependent solar wind conditions containing different types of disturbances typical of those seen at Mercury's orbit, such as Coronal Mass Ejections (CMEs) and IMF rotations. Their results show that the reconfiguration of Mercury's magnetosphere indeed induces intense electric currents at the core where the electrical conductivity is high. Associated with those induced currents are strong magnetic perturbations present not only inside of the planet but also throughout the magnetosphere, clearly demonstrating that the induction effect plays an important role in determining the global magnetospheric structure.

While the modeling efforts discussed above represent a first step in characterizing Mercury's magnetosphere-core coupling in a self-consistent manner, future work is clearly needed to further quantify the induction effect. A particularly important question that should be addressed with self-consistent global simulations is how the strong magnetosphere-core coupling affects the extent to which the solar wind particles can have access to the planet's surface, which is of direct relevance to the plasma sources of Mercury's magnetosphere.

5.1.2 Exospheric Modeling

Global models of Mercury's neutral exosphere have made significant contributions to understanding of its origin from complex interactions between the Sun and the surface of the planet, as well as of seasonal variations due to Mercury's highly elliptical orbit [*Leblanc and Johnson*, 2003, 2010; *Mura et al.*, 2007; *Burger et al.*, 2010, 2012; *Wurz et al.*, 2010; *Sarantos et al*., 2011; Pfleger et al., 2015]. Since the exosphere is collisionless, particle dynamics in these models are determined rather simply by gravity and radiation pressure; however, the sources and sinks of the exosphere add considerable complication and are the main area of active development. Global models typically include the source processes that have been described in Section 3.2.1: thermal desorption, ion sputtering, photon-stimulated desorption and micrometeroid vaporization (TD, IS, PSD and MV). Additionally, the main loss processes included are photoionization, surface sticking and gravitational escape. Of these three loss mechanisms, photoionization of exospheric neutral atoms is particularly important because it is also a significant *source* of planetary ions to Mercury's magnetosphere. The physics of these processes is well understood from laboratory measurements. Nevertheless, there is sufficient uncertainty in crucial parameters – such as Mercury's surface composition and the incident solar wind plasma – that the relative contributions of these processes are not well determined. Many researchers have sought to remedy this problem by using observations to constrain their models, either from Earth (ground-based) or MESSENGER. This synthesis of models and observations has been very effective in narrowing the parameter space, but the relative contributions of the various surface processes are still in dispute.

A subset of global exosphere models are able to simulate the dynamics of planetary ions in the system once they are created [*Sarantos et al.*, 2009]. This modeling capability is key to obtain a global understanding of plasma sources into Mercury's magnetosphere. It provides, thus far, the only quantitative connection to planetary ion sources from both the exosphere and surface, though their relative importance is also an open question. To model ion dynamics, exospheric models must also include the electric and magnetic fields of the magnetosphere. These models primarily focus on planetary ions, which are much lower in abundances than the solar wind ions that drive the magnetosphere. As a result, they incorporate static fields, typically from MHD models. Planetary ions are then *flown* through these fields by integrating their equation of motion directly. The ions are often treated as test particles, each representing a larger number of ions in the real system.

The ion component of global exospheric modeling can feedback into understanding the composition of the exosphere itself. From MESSENGER FIPS measurements, as well as from ion composition measurements around the Moon [e.g., *Mall et al.*, 1998], we know that many more species exist that have not been observed. Many of these atmospheric species do not have emission lines in the MESSENGER UltraViolet and Visible Spectrometer (UVVS) spectral range; therefore FIPS measurements present the only way to update upper limits prior to BepiColombo orbit insertion. The observed seasonal variability of the exosphere [e.g., *Leblanc and Johnson*, 2010, for Na; *Burger et al.*, 2014, for Ca] has not yet been folded into ion model calculations.

5.1.2.1 Ions from the exosphere

Na+ of exospheric origin is the only species that has been systematically studied with simulations. Trajectory tracings of Na ion test particles were performed in analytical [*Delcourt et al.*, 2003], resistive MHD [*Yagi et al.*, 2010; *Seki et al.*, 2013], Hall MHD [*Sarantos et al.*, 2009] and hybrid [*Paral et al.*, 2010] simulated fields (Figure 20). For the first three the exospheric model of *Leblanc and Johnson* [2003] was used, in which the finite Na reservoir is quickly depleted by thermal desorption leading to an exosphere with a dawn-dusk asymmetry, whereas the other two considered different mixes of photon stimulated desorption and sputtering, both spherically symmetric with respect to the Sun-Mercury line. Unfortunately, because of the small size of Mercury's magnetosphere, these tracings are very sensitive to the treatment of the inner boundary condition [*Seki et al.*, 2013] and therefore differ between models.

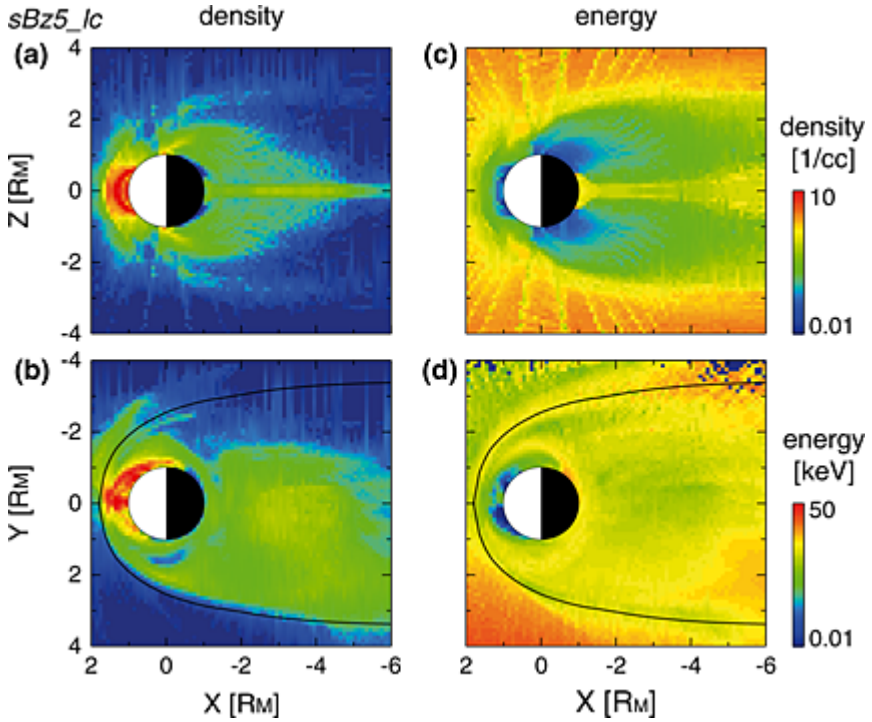

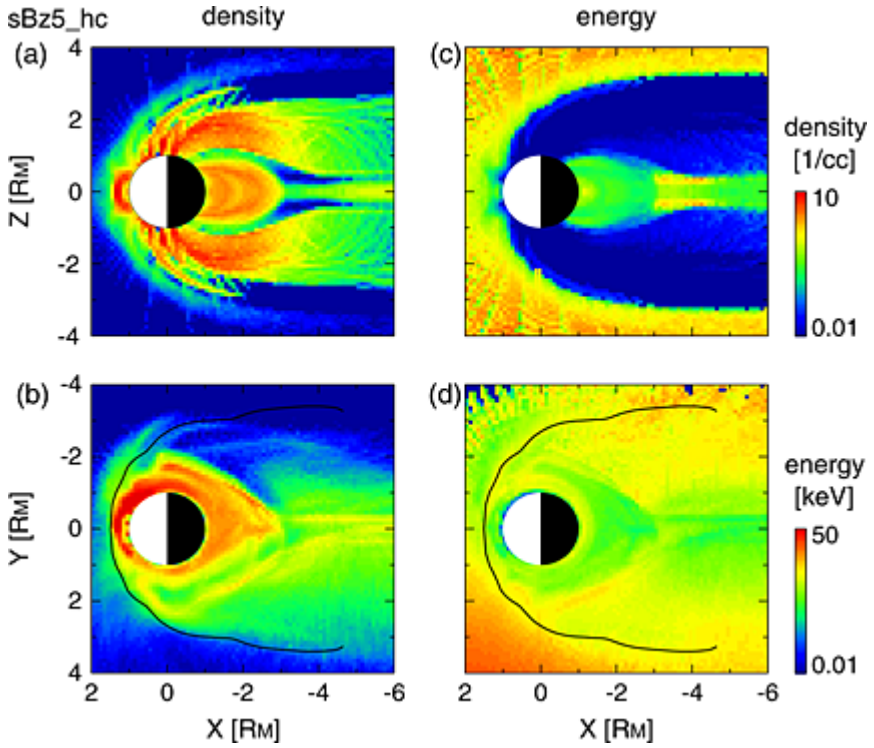

Figure 20. Na ion distribution under the same southward IMF (B_z = –5 nT) and solar wind conditions, initialized with the same exosphere model, but subject to different assumptions of the inner boundary condition. Case with high surface conductance shown in the bottom panel. The resulting ion distributions are markedly different as the formation of an X-line further from the planet inhibits escape in the second case. [From Seki et al., 2013]

A common feature of these simulations is an enhancement of Na^+ near dawn and in the morning sector. The estimated concentration peaks exceeded 10 Na^+ cm^{-3} near the equator [*Yagi et al.*, 2010]. The pressure exerted by planetary ions in these simulations can locally surpass 10% of the total, thus necessitating that sodium becomes one of the species of the MHD and hybrid simulations. Escape of planetary ions through a porous magnetopause, especially under southward IMF conditions, is evident in the simulations [*Paral et al.*, 2009].

Magnetospheric ion recycling and its effect has been the subject of several works. "Self sputtering" is itself an inconsequential source for the exosphere [e.g., *Delcourt et al.*, 2003; *Poppe et al.*, 2013] as the recycled ion fluxes are a small portion of the inferred neutral efflux (~10^7 Na cm^{-2} s^{-1}). However, recycling could be important if ions neutralized in the soil increase the available reservoir for trace species [*Killen et al.*, 2004]. High ion recycling rates will obviously increase the reservoir for exogenous species of the exosphere that are in balance with the solar wind influx (e.g., He, Ne); but they could also increase the reservoir for exospheric Na and K, which are very nearly depleted on the dayside [*Leblanc and Johnson*, 2003, 2010) to levels that can be supported by grain diffusion [*Killen et al.*, 2004]. Broad bands of nightside precipitation of Na+ with fluxes ~10^5 Na+ cm^{-2} s^{-1} and extending up to ±50° latitude form when realistic conditions about the surface conductance are adopted [*Seki et al.*, 2013]. These contain sub-keV ions which are deposited very near the top of the grains and should quickly diffuse to the grain surface. *Schmidt* [2013] proposed that ion precipitation to Mercury's nightside, which is shifted northward because the geomagnetic equator is displaced with respect to the geographic equator,

is a mechanism for producing the north-south asymmetries of the dayside Na exosphere observed from ground-based telescopes [e.g., *Potter et al.*, 2006].

5.1.2.2 Ions from the surface

Both precipitating protons and electrons can contribute to a surface ion source. *McLain et al.* [2011] suggested that electron stimulated desorption (ESD) could be an important source of Mercury's ions. Thresholds for such emission (~20 eV) are typically too high for solar wind electrons impinging onto the Moon but can clearly be exceeded at Mercury. While the typical yield for sputtered ions by proton impingement is in the range of 10^{-4} to 10^{-1} per impacting ion [*Benninghoven*, 1975], the yields measured for ESD could be ten times higher, especially the more energetic the incident electrons [*Wang et al.*, 1984]. Ions and electrons from the solar wind should precipitate not only onto Mercury's cusp areas but also persistently onto the nightside in auroral regions as well as regions surrounding the geomagnetic equator [e.g., *Benna et al.*, 2010]. Thus, the Hermean surface at high latitudes of the dayside and low latitudes of the nightside are regions of planetary ion emission.

Outflow of ions released directly from the surface could be responsible for some of the cusp signatures observed by MESSENGER FIPS [*Raines et al.*, 2014]. Despite their sub-escape initial energies (~1 eV), such ions will be rapidly accelerated by centrifugal sources and escape into the magnetosphere [*Delcourt et al.*, 2012]. Their importance relative to photoions is uncertain. At the Moon, predictions from *Sarantos et al.* [2012] suggest that ions from exospheric neutrals dominate over surface ions for many metallic constituents such as Na^+, although for some species with more stringent exospheric limits (e.g., Ca^+) the surface should be the most important source. At Mercury such calculations are yet to be performed.

5.1.2.3 Estimating total ion source rates

Models of the exosphere can provide a rough estimate for the sodium ion source rate in Mercury's magnetosphere, indirectly, via the commonly reported quantity of total exosphere content and the assumption, common to all models, that photoionization is the dominant ionization process. The answer varies from model to model, of course, but despite their major differences, all sodium models estimate the *content* to be on the order of 10^{28} sodium atoms [the exosphere content ranges 0.3-$4\text{x}10^{28}$ in the following: *Smyth and Marconi*, 1995; *Killen et al.*, 2001; *Mura et al.*, 2009; *Leblanc and Johnson*, 2010; *Mouawad et al.*, 2011].

These models do not use the same data sets and they even have different basic assumptions, yet they estimate the sodium content within the same order of magnitude. Consider the difference between the models described by *Leblanc and Johnson* [2003, 2010] and *Burger et al.* [2010]: the two models have quite different mixtures of source processes and, even more fundamentally, differ in basic construction. The exosphere in Leblanc and Johnson is coupled to a large reservoir of adsorbed sodium atoms on Mercury's surface, while Burger et al. have no reservoir. Leblanc et al. [2010] ran their model for several simulated Mercury years and matched their results to several Earth years of ground-based observations; the Burger et al. model only simulated several hours and compared their result data taken during two of MESSENGER's Mercury flybys.

The the ion source rate can be estimated from published results by multiplying this exosphere content by the photoionization frequency, which is on the order of 10^{-4} s^{-1} [*Huebner et al.*, 1992]. Assuming that most of the exosphere is exposed to

sunlight, this gives a sodium ion source rate on the order of 10^{24} sodium ions s^{-1}, or a mass loss of several 10s of g s^{-1}. This is comparable to the ion outflow from the other terrestrial planets [*Strangeway et al.*, 2010], but some fraction of Mercury's ion production is lost to its surface. As discussed above, Na^+ is the most abundant planetary ion detected by FIPS. Ionized magnesium may contribute to the sodium ion signature owing to its similar mass, but it is much less abundant in the exosphere and has a longer lifetime against photoionization.

Sodium is the most abundant exospheric species identified so far, but there are several others. During one of MESSENGER's Mercury flybys, UVVS observed simultaneously neutral and ionized Ca (Figure 21). The observed sharp decrease in Ca away from the planet can be explained by quick ionization [*Vervack et al.*, 2010] and models applied to MASCS data support a strong localized source at dawn at high temperature (>50000 K), probably related to micrometeoritic impact vaporization of Ca in the form of CaO and CaOH, and subsequently dissociated [*Burger et al.*, 2014]. The model of UVVS calcium observations provides a Ca^+ photoion source on the order of 10^{23} calcium ions s^{-1} [*Burger et al.*, 2014], though much of the calcium is ionized beyond the magnetosphere owing to its high-energy ejection process. Hydrogen and helium gases are thought to be neutralized solar wind plasma that are later (re-) ionized to contribute to the planetary ions detected by FIPS. The planetary helium is distinct from solar wind helium as it is singly, rather than doubly, ionized. *Broadfoot et al.* [1976] estimated that most of the planetary helium escapes Mercury's gravity before photoionization, although the energy distribution of the neutral helium is highly uncertain [*Shemansky and Broadfoot*, 1977; *Leblanc and Chaufray*, 2011]. *Broadfoot et al.* [1976] estimated that the helium ion source rate from the helium exosphere is on the order of 10^{22} helium ions s^{-1}.

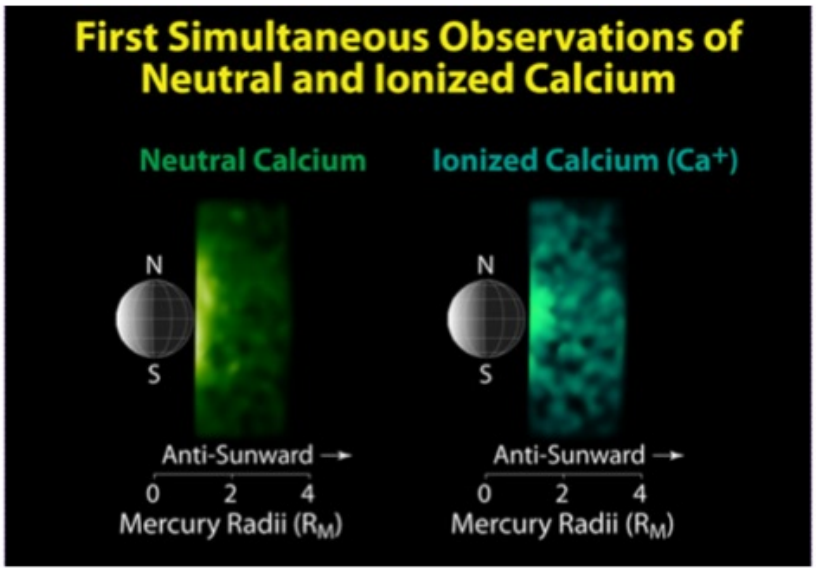

Figure 21. Ca and Ca^+ distribution tailward as detected by MESSENGER MASCS UVVS during flybys. ***Additional (unpublished) material from Vervack et al.*****, [2010].**

5.2 Ion Acceleration Processes and Non-adiabatic Behavior

5.2.1 Centrifugal acceleration in Mercury's lobes

To the first order, the large scale plasma circulation at Mercury resembles that at Earth, the coupling between the magnetosphere and the interplanetary magnetic field being responsible for a dawn-to-dusk convection electric field with antisunward transport at high latitudes (typically, above 50°) and return sunward flow at low latitudes. In this context, a process that readily affects planetary ions after their ejection into the magnetosphere is the centrifugal acceleration associated with the large scale **E**×**B** transport. Using a guiding center approach, *Cladis* [1986] showed that, during transport from high to low latitudes, ions expelled from the topside terrestrial ionosphere may be subjected to substantial acceleration in the parallel direction. Because of the small spatial scales of the Hermean environment, it was pointed out by *Delcourt et al.* [2002] that this acceleration is more pronounced at Mercury than at Earth, possibly leading to energization of heavy ions up to several hundreds of eVs or a few keVs in the lobes prior to their entry into the plasma sheet. This is at variance with the energy gain up to at most a few tens of eVs expected at Earth [e.g., *Yau et al.*, 2012].

In particular, in contrast to Earth, the above centrifugal acceleration may play a specific role in the escape of planetary material at Mercury; hence, a prominent impact on the net plasma supply to the Hermean magnetosphere. Indeed, at Earth, unless a short-lived compression event affects the magnetosphere [e.g., *Cladis et al.*, 2000], this acceleration is weak and operates over a long time as particles travel downtail in the lobes. Ions ejected from the terrestrial ionosphere with velocities smaller than the escape speed are not sufficiently accelerated by this mechanism to overcome gravity and return toward the ionosphere according to parabolic or hoping trajectories [e.g., *Horwitz*, 1984]. Because of the pronounced curvature of the magnetic field lines in the immediate vicinity of the planet surface, a different situation is obtained at Mercury with abrupt energization of the ions immediately after ejection into the magnetosphere [*Delcourt*, 2013]. In this latter study, it was found that the numerous populations that are released at very low energies such as those due to thermal desorption are rapidly accelerated up to ~$2V_{\boldsymbol{E}\times\boldsymbol{B}}$ ($V_{\boldsymbol{E}\times\boldsymbol{B}}$ being the **E**×**B** drift speed) in a like manner to the acceleration due to a moving magnetic mirror [*Cowley*, 1984]. Accordingly, instead of being trapped near the planet surface due to ejection velocities smaller than the escape speed, these ions readily overcome gravity and flow into the magnetosphere. Also, since the parallel velocity realized does not depend upon mass-to-charge ratio, all ion species are transported into a similar region of space in the pre-midnight sector of the inner magnetotail which may explain the density enhancements locally recorded by MESSENGER [*Raines et al.*, 2013].

Moreover, the study of *Delcourt* [2013] suggests that the centrifugal focusing of planetary material thus obtained depends little upon the convection rate, an increase of the convection electric field magnitude (and associated **E**×**B** drift speed) resulting into an increase of the particle parallel speed in the same proportion.

5.2.2 Spatial nonadiabaticity in Mercury's magnetotail

Upon reaching the field reversal in the magnetotail, particles may not conserve their magnetic moment (first adiabatic invariant) because of significant field variations on the length scale of the particle Larmor radius. A parameter that is often used to characterize this nonadiabatic behavior is the parameter κ defined as the square root of the minimum field line curvature radius-to-maximum Larmor radius ratio. For $\kappa > 3$, the particle motion is adiabatic and the guiding center approximation is valid while for κ of the order of unity or below, the motion is nonadiabatic with possibly large variations of the magnetic moment. (For more details see *Seki et al.*, 2015, this volume). At Earth, the transition from adiabatic to nonadiabatic regimes, viz. $\kappa \approx 1$, occurs in the mid-tail for plasma sheet ions. This region has been viewed either as the onset of prominent injections into the atmospheric loss cone and subsequent ion precipitation (leading to the Isotropy Boundary interpretation framework of *Sergeev et al.* [1993]) or as a domain of enhanced trapping (hence, the "wall" picture put forward by *Ashour-Abdalla et al.* [1992]), both pictures being valid since particles are subjected to either magnetic moment damping or enhancement [e.g., *Delcourt et al.*, 1996]. At Mercury, because of the weak intrinsic magnetic field and of the strong solar wind dynamical pressure, the magnetosphere is small and the planet occupies a much larger volume of it than at Earth. The nearly dipolar region of the inner terrestrial magnetosphere where the particle motion is essentially adiabatic is thus absent at Mercury, and it is expected that most ions behave nonadiabatically throughout the magnetotail. Computations of the adiabaticity parameter κ in model magnetospheres of Mercury actually suggest that the condition $\kappa \approx 3$ is met in the immediate vicinity of the planet. Hybrid simulations where a kinetic description is used for ions while electrons are treated as a massless fluid are thus most appropriate at Mercury [e.g., *Kallio and Janhunen*, 2003; *Travnicek et al.*, 2007; *Richer et al.*, 2012].

The fact that ions behave nonadiabatically in most of the hermean magnetotail is of importance for its structure and dynamics. In particular, be they of solar wind or planetary origin, ions at $\kappa < 1$ may display either quasi-trapped orbits with repeated crossings of the field reversal or Speiser-type orbits [*Speiser*, 1965] with large energization along the dawn-dusk convection electric field during meandering motion about the midplane. Such nonadiabatic behaviors that are sometimes referred to as "quasi-adiabatic" because of possible conservation of the action integral I_Z [*Büchner and Zelenyi*, 1989], are of paramount importance since they lead to the formation of

thin current sheets embedded within a thick plasma sheet. Instability of these thin current sheets can lead to local current disruption and consequent reconfiguration of the magnetic field lines [e.g., *Mitchell et al.*, 1990]. Nonadiabatic particle behaviors also lead to the formation of nongyrotropic distribution functions ; hence, significant off-diagonal terms in the plasma pressure tensor and a stress balance that does not rely on a large pressure gradient along the tail axis.

As planetary ions reach the magnetotail midplane after **E**×**B** transport over the polar cap, they are nearly aligned with the magnetic field owing to pitch angle folding from low to high altitudes. Would their motion be adiabatic (magnetic moment conserving), these ions would return to the planet vicinity after a single crossing of the magnetotail midplane and precipitate onto the surface. Far from such a behavior, planetary ions are subjected to prominent magnetic moment scattering upon interaction with the field reversal. As a result of this isotropization and temporary trapping, and without invoking other processes such as wave-particle interactions, these ions are found to substantially contribute to the plasma sheet populations. In a quantitative study of the Na^+ circulation at Mercury, *Delcourt et al.* [2003] considered a model exosphere of neutral sodium [*Leblanc and Johnson*, 2003] and showed that this planetary material may contribute up to a few tenths of ions/cm^3 to the equatorial magnetotail, this contribution depending upon phase angle along Mercury orbit. Such densities are in qualitative agreement with those reported by *Raines et al.* [2013] in their analysis of MESSENGER data. Also, assuming a cross-polar cap potential drop of 20 kV, the simulations of *Delcourt et al.* [2003] put forward times of flight from the high-latitude dayside sector to the inner plasma sheet of the order of a few minutes on the average, together with a prominent asymetry between dawn and dusk sectors due to westward drift of the ions.

During their nonadiabatic transport, Na^+ ions can be injected inside the loss cone which is much larger at Mercury than at Earth due to the weak planetary magnetic field; hence, their precipitation onto the planet surface. In the modified Luhmann-Friesen model considered by *Delcourt et al.* [2003], this ion precipitation is organized according to two narrow bands at mid-latitudes (between ~30° and ~40°), the κ parameter varying from ~1 down to ~0.1 as the latitude increases. The poleward boundary of these precipitation bands is controlled by the width of the magnetotail, ions at higher latitudes (or, equivalently, at larger distances in the magnetotail) intercepting the magnetopause in the course of their duskward motion. Using results of MHD simulations, *Seki et al.* [2013] demonstrated that this overall precipitation pattern may significantly depend upon the planet surface conductivity as well as IMF orientation, the formation of a near-Mercury neutral line leading to significant downtail loss of planetary ions.

5.2.3 Temporal nonadiabaticity in Mercury's magnetotail

The nonadiabatic transport features described above in the magnetotail field reversal result from large magnetic field variations on the length scale of the particle Larmor radius. These features accordingly relate to spatial nonadiabaticity. In the case of explicit temporal variations of the field on the time scale of the particle gyroperiod, nonadiabatic features may appear as well. This latter temporal nonadiabaticity cannot be characterized with the help of the κ parameter, and it may actually occur in regions where $\kappa > 3$ (i.e., where the spatial adiabaticity condition is fulfilled). Such a temporal nonadiabaticity may emerge for instance during short-lived reconfigurations of the magnetospheric field lines. In this regard, it was shown that, at Earth, heavy ions originating from the ionosphere such as O^+ may be subjected to prominent nonadiabatic energization up to the hundred of keV range during substorm dipolarization [e.g., *Delcourt*, 2002]. This energization due to the electric field induced by the time-varying magnetic field preferentially affects O^+ ions that have cyclotron periods comparable to the dipolarization time scale. In contrast, protons that have smaller gyroperiods are transported adiabatically (provided that $\kappa > 3$) and subjected to Fermi-type or betatron energization. Because of the smaller characteristic time scales of the Mercury's environment (e.g., with a typical Dungey cycle time of ~2 min as opposed to ~1 hour at Earth), it may be anticipated that protons will be subjected to such a temporal nonadiabaticity during reconfigurations of the Hermean magnetotail.

Figure 22 shows the energy variations obtained for protons in the case of a 10-second model dipolarization of the magnetic field lines in the inner magnetotail of Mercury. In this figure, the H^+ post-dipolarization energy is shown as a function of initial energy and for different initial gyrophases. Because the particles considered here are equatorially trapped (i.e., 90° pitch angle at equator), no effect due to parallel motion and spatial nonadiabaticity is to be expected.

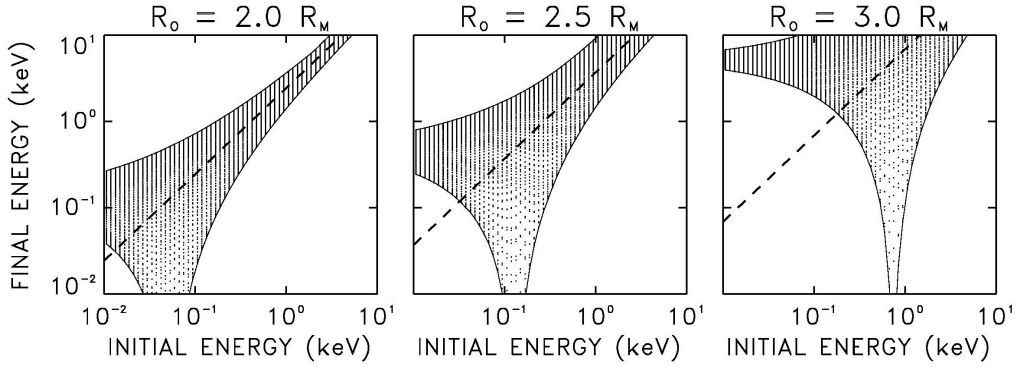

Figure 22: Post-dipolarization energy versus initial energy for equatorially mirroring H^+ launched from different initial distances : (from left to right) 2, 2.5, and 3 R_M. In each panel, the various dots

correspond to distinct initial gyrophases whereas the dashed line shows the final energy expected in the case of adiabatic (betatron-type) energization.

It is apparent from Figure 22 that protons with low initial energies are systematically energized up to a level that gradually increases with initial distance (from left to right). In particular, in the right panel of Figure 22, the low-energy protons initialized at 3 R_M are systematically energized up to ~4 keV while being transported down to ~1.8 R_E. This nonadiabatic behavior at low initial energies contrasts with that obtained at large initial energies where betatron-type energization (i.e., in proportion to the change in magnetic field magnitude) is obtained. Although short-lived fluctuations of the magnetic field that are not considered here may lead to deviations from these results, it is clearly apparent from Figure 22 that, in a like manner to O^+ at Earth, protons may be transported in a nonadiabatic manner during dipolarization events at Mercury. Under the effect of the transient induced electric field, these ions may experience energy gains significantly above that expected from the large scale convection electric field alone.

Because temporal nonadiabaticity is to be expected whenever the magnetic field changes significantly on the time scale of the particle gyroperiod, it may be anticipated that ions will be transported nonadiabatically not only in the equatorial region but also at high latitudes. This follows from the short characteristic time scales at Mercury as well as from the weak intrinsic magnetic field that leads to large ion gyroperiods. An example of such behaviors is provided in Figure 23 that shows the results of Na^+ simulations during a 20-s turning of the IMF from $B_X = 0$ to $B_X = 20$ nT [*Delcourt et al.*, 2011]

The leftmost panels of Figure 23 depict symmetrical Na^+ flows from the high latitude dayside sector above the polar cap as well as gradual centrifugal acceleration up to the keV range before reaching the nightside plasma sheet. On the other hand, during IMF turning (from left to right in Figure 23), it is apparent that the Na^+ average energy (bottom panels) off equator rapidly increases up to several keVs. As discussed above, this energization occurs in a nonadiabatic manner and follows from resonance between the induced electric field and the particle gyromotion. At high latitudes, such a resonance is achieved for Na^+ and Figure 23 thus suggests that IMF turning or short-lived magnetic transitions at Mercury may go together with the rapid production of heavy energetic material in the magnetospheric lobes.

6 Summary

Mercury's magnetosphere is dynamic and its environment is extreme. It is similar enough to allow application of terrestrial theory and approaches, yet it has differences sufficient to challenge some of them with the need for more sophistication. Mercury's intrinsic field is sufficient to stand off the solar wind, but creates a very small magnetosphere that responds dramatically to changing solar wind

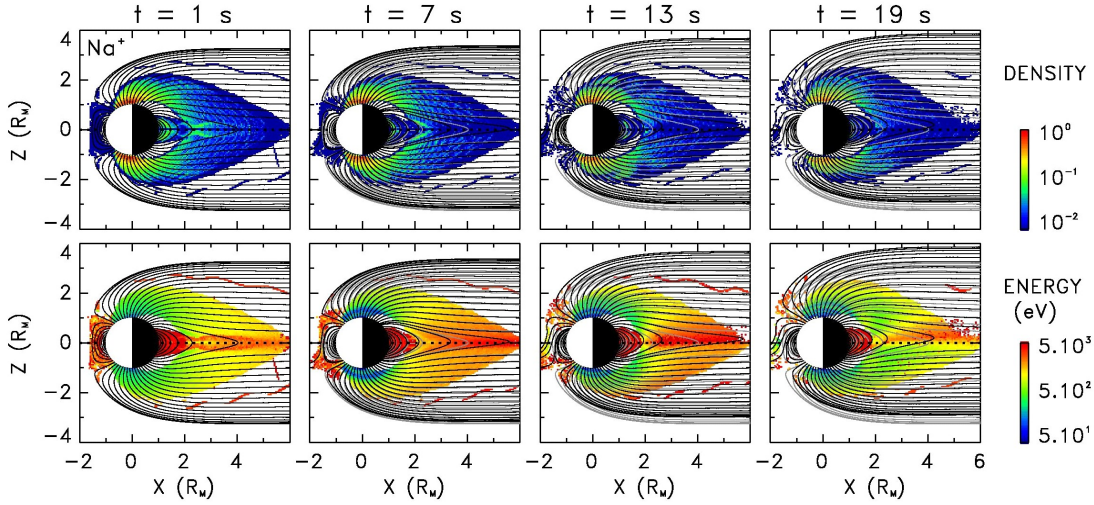

Figure 23 : (Top) Model normalized density and (bottom) average energy of Na^+ ions in the noon-midnight meridian plane during a model IMF turning. Panels from left to right show snapshots at distinct times of the magnetic transition. Black and grey lines show the magnetic field lines at the corresponding time and in the initial configuration, respectively. Density and energy are coded according to the colour scales at right. From *Delcourt et al.* [2011].

conditions. The main global dynamical behavior is Dungey cycle circulation but at a rate about 30 times faster than at Earth, contributing to the magnetosphere's ability to reconfigure very quickly. This convection is driven by magnetic reconnection at the dayside magnetopause, but unlike other planetary magnetospheres, the reconnection rate is independent of magnetic shear angle. As a consequence of frequent magnetopause reconnection, Mercury's magnetosphere is dominated by Dungey cycle convection.

MESSENGER measurements have unambiguously proven that Mercury's magnetosphere is populated with plasma of both solar wind and planetary origins. The magnetospheric plasma distribution is similar to Earth's, concentrated at high-latitudes in the dayside magnetospheric cusp and tail lobes as well as in the equatorial plane of the central plasma sheet in the tail. Solar wind protons are the most abundant species in those regions, followed by solar wind alpha particles and Mercury-derived Na^+ ions (grouped with Mg^+ and Si^+ in observations). Two other planetary ion species have been studied, the O^+ group and He^+. Both are present in lower abundance than Na^+-group ions and have not been studied in much detail. Other planetary ions with $m/q > 30$ appear in FIPS data and work is underway to identify them. In the cusp, Na^+-group ions come from two sources: upwelling from the surface and swept in by reconnection from the vicinity of the dayside magnetopause. Plasma loss to the surface has been observed through the presence of a large loss cone of ~59° in a long-term average. In the central plasma sheet, protons dominate the number density by an order of magnitude, but Na^+-group ions can comprise up to 50% of the mass density and 15% of the thermal pressure. Observations of Kelvin-Helmholtz waves, along the

magnetopause boundary, have provided the first conclusive evidence that these planetary ions are dynamically important in Mercury's magnetosphere.

The ultimate sources of planetary ions are certainly Mercury's tenuous exosphere and mineral surface, but their relative contributions have not yet been determined conclusively. Lacking a collisional ionosphere, Mercury's magnetosphere and exosphere are co-located, making their coupling via source and sink processes very direct. Global modeling of the exosphere is quite sophisticated, including all of these processes as well as effects related to surface reservoir and Mercury's extreme seasonal differences. Ground-based observations of the exosphere have been used extensively to constrain these models, though constraint with MESSENGER observations is just reaching maturity. Some of these models include generation and test particle tracing of planetary ions, but work to compare these quantitatively with MESSENGER plasma ion observations is only beginning.

7 Open Questions

Despite understanding many aspects of plasma sources in Mercury's magnetosphere, there are several top-level questions that still remain.

What is the role of the solar wind in generating the exosphere and populating the magnetosphere with planetary ions? The solar wind is expected to act as a highly variable exospheric (and likewise magnetospheric) source via precipitation and ion sputtering. The search for concrete observational evidence of this effect is still on going. Precipitation of solar wind protons and upwelling surface ions has been observed *in situ* by MESSENGER but a definitive cause and effect relationship has not been established. One complication is the fact that newly created ions, from all processes involved, have peak energies of just a few eV and to be observed they must be accelerated above FIPS energy minimum, which has been 46 eV for much of the MESSENGER mission. The limit was lowered in August 2014, down to effectively the spacecraft potential (10s of eV) but those measurements have not yet been analysed in detail. Ground-based exospheric observations have shown variability on the timescale of hours, consistent with solar wind generation of exospheric neutrals, but have not been correlated *in situ* solar wind observations. Finally, confirmation with MESSENGER UVVS observations has proven elusive, due partly to operational constraints that have allowed for only very limited UVVS observations in the magnetospheric cusps where variability due to solar wind should be at a maximum. The frequency of these observations increased toward the end of the mission so the nature of this relationship may still be established from MESSENGER data. In any case, the BepiColombo Mercury Planetary Orbiter will measure these neutral atoms directly with the Strofio instrument, a low energy neutral gas mass spectrometer of the SERENA particle package [*Orsini et al.* 2010]. Working with the particles and fields instrument on the Mercury Magnetospheric Orbiter, this correlation should be established in a straightforward way.

In what proportions to other exogenic processes contribute and how do they vary with season? Despite significant progress in tying observations to physical processes and the creation of realistic global models, no quantitative, consensus global picture of exosphere generation has emerged. One problem is that the system is under-constrained. The relative contributions to the exosphere of the many source and sink processes is likely different for each exospheric neutral species, and may be a function of Mercury season and even location on the surface. Exospheric composition depends on details of surface composition at significantly higher resolution than

available. It may depend on other inputs such as micrometeriod impact rates or traversal of the interplanetary dust disk, which are at best difficult to measure. On-going work combining the available measurements with self-consistent exosphere/magnetosphere models will likely continue to improve understanding, as will additional measurements from the two-spacecraft BepiColombo mission. However it is possible that there are just too many free parameters to adequately constrain with the relatively sparse measurements that are possible at Mercury.

Do heavy planetary ions make an important contribution to magnetospheric dynamics and if so, how? MESSENGER observations have shown that planetary ions change the scale of Kelvin-Helmholtz waves along Mercury's tail magnetopause. This dynamical contribution could have significant effect on plasma entry through this process. Observations in Mercury's central plasma sheet have shown that they can make up a significant portion of the pressure and dominate the mass density. This certainly sets the stage for participating in magnetospheric dynamics. That said, planetary ions have not yet been shown to influence plasmoids in the magnetotail or act as more than a tracer of plasma flowing through Mercury's northern magnetospheric cusp on newly reconnected field lines. Further analysis of MESSENGER data will likely shed more light on this question. However, the BepiColombo mission, with two spacecraft, more complete particles and fields instrumentation and the larger fields of view possible without sunshade obstructions, is well-poised to address this very complex question.

Does surface impact and sputtering by magnetospheric ions constitute a significant source to Mercury's exosphere and magnetosphere? Tracing protons on closed field lines in the magnetotail has shown losses that should be indicative of impact on the planet's surface. They have nearly the same energy as precipitating protons in the cusp and should, therefore, cause sputtering of ions and neutral atoms. Protons traveling toward the surface in closed field regions have not been observed, though MESSENGER's orbit and orientation is not well-suited to observing this precipitation. MHD and Hybrid simulations show this behavior, but as of yet, determining the contribution to the exosphere and magnetosphere of this process from simulations has not converged to clear values. In addition to protons, planetary ions such as Na^+ present in the magnetotail should behave similarly. Their higher energies, up to 10 keV, could make their precipitation contribute more than would be expected by relative number densities alone.

A lot has been learned about Mercury so far, from Mariner 10, ground observations, MESSENGER and modeling, but there is much left to do. Analysis of MESSENGER orbital data is really just in the early stages; new results should continue to come out for years to come. In less than a decade after the end of the MESSENGER mission, BepiColombo will arrive to enable a new and potentially more detailed study of the closest planet to the Sun.

8 Compliance with Ethical Standards

This article is in compliance with the ethical standards laid out by the COPE guidelines. There are no conflicts of interest and no human or animal subjects were used in this work. All co-authors have contributed to this manuscript and have given their consent to its submission.

9 References

Alexeev, I. I., E. S. Belenkaya, J. A. Slavin, H. Korth, B. J. Anderson, D. N. Baker, S. A. Boardsen, C. L. Johnson, M. E. Purucker, M. Sarantos, and S. C. Solomon (2010), Mercury's magnetospheric magnetic field after the first two MESSENGER flybys, *Icarus, 209*, 23–39.

Anderson, B. J., M. H. Acuna, D. A. Lohr, J. Scheifele, A. Raval, H. Korth, and J. A. Slavin (2007), The Magnetometer instrument on MESSENGER, *Space Sci. Rev., 131*, 417-450.

Anderson, B. J., et al. (2011), The global magnetic field of Mercury from MESSENGER orbital observations, *Science, 333,* 1859–1862, doi:10.1126/science.1211001.

Anderson, B. J., C. L. Johnson, H. Korth, R. M. Winslow, J. E. Borovsky, M. E. Purucker, J. A. Slavin, S. C. Solomon, M. T. Zuber, and R. L. McNutt Jr. (2012), Low-degree structure in Mercury's planetary magnetic field, *J. Geophys. Res., 117*, E00L12, doi:10.1029/2012JE004159.

Anderson, B. J., C. L. Johnson, H. Korth, J. A. Slavin, R. M. Winslow, R. J. Phillips, R. L. McNutt Jr., and S. C. Solomon (2014), Steady-state field-aligned currents at Mercury, *Geophys. Res. Lett., 41*, 7444–7452, doi:10.1002/2014GL061677.

Andrews, G. B., et al. (2007), The Energetic Particle and Plasma Spectrometer instrument on the MESSENGER spacecraft, *Space Sci. Rev., 131*, 523–556, doi:10.1007/s11214-007-9272-5.

Angelopoulos, V., C. F. Kennel, F. V. Coroniti, R. Pellat, M. G. Kivelson, R. J. Walker, C. T. Russell, W. Baumjohann, W. C. Feldman, and J. T. Gosling (1994), Statistical characteristics of bursty bulk flow events, *J. Geophys. Res., 99*, 21,257–21,280.

Armstrong, T. P., S. M. Krimigis, and L. J. Lanzerotti (1975), A reinterpretation of the reported energetic particle fluxes in the vicinity of Mercury, *J. Geophys. Res., 80*, 4015–4017, doi:10.1029/JA080i028p04015.

Ashour-Abdalla, M., L. M. Zelenyi, J.-M. Bosqued, V. Peroomian, Z. Whang, D. Schriver, and R. L. Richard (1992), The formation of the wall region: Consequences in the near-Earth magnetotail, *Geophys. Res. Lett.*, *19*, 1739.

Ashour-Abdalla, M., M. El-Alaoui, M. L. Goldstein, M. Zhou, D. Schriver, R. Richard, R. Walker, M. G. Kivelson, and K. J. Hwang (2011), Observations and simulations of non-local acceleration of electrons in magnetotail magnetic reconnection events, *Nature Phys., 7,* 360–365.

Baker, D. N., J. A. Simpson, and J. H. Eraker (1986), A model of impulsive acceleration and transport of energetic particles in Mercury's magnetosphere, *J Geophys. Res, 91*, 8742–8748.

Baker, D. N., T. I. Pulkkinen, V. Angelopoulos, W. Baumjohann, and R. L. McPherron, (1996), Neutral line model of substorms: Past results and present view, *J. Geophys. Res., 101*, 12,975–13,010.

Baker, D. N., G. Poh, D. Odstrcil, C. N. Arge, M. Benna, C. L. Johnson, H. Korth, D. J. Gershman, G. C. Ho, W. E. McClintock, T. A. Cassidy, A. Merkel, J. M. Raines, D. Schriver, J. A. Slavin, J. A., and S. C. Solomon (2013), Solar wind forcing at Mercury: WSA-ENLIL model results, *J. Geophys. Res. Space Physics, 118*, 45–57.

Baumjohann, W., and G. Paschmann (1989), Determination of the polytropic index in the plasma sheet, *Geophys. Res. Lett., 16*, 295–298.

Behrisch, R., and W. Eckstein (2007), Sputtering by particle bombardment: experiments and computer calculations from threshold to MeV energies, Springer, 110.

1741 Benkhoff, J., J. van Casteren, H. Hayakawa, M. Fujimoto, H. Laakso, M. Novara, P.
1742 Ferri, H. R. Middleton, and R. Ziethe (2010), BepiColombo-Comprehensive
1743 exploration of Mercury: Mission overview and science goals, *Planet. Space Sci.,*
1744 *58*, 2–20.
1745 Benna, M., et al., (2010), Modeling of the magnetosphere of Mercury at the time of
1746 the first MESSENGER flyby, *Icarus, 209*, 3–10, doi:10.1016/j.icarus.2009.11.036.
1747 Benninghoven, A. (1975), Developments in secondary ion mass spectroscopy and
1748 applications to surface studies, Surface Science, 53, 596-625, doi:
1749 10.1016/0039-6028(75)90158-2.
1750 Bida, T. A., R. M. Killen, and T. H. Morgan (2000), Discovery of calcium in
1751 Mercury's atmosphere, *Nature, 404*, 159–161.
1752 Boardsen, S. A., B. J. Anderson, M. H. Acuña, J. A. Slavin, H. Korth, and S. C.
1753 Solomon (2009), Narrow-band ultra-low-frequency wave observations by
1754 MESSENGER during its January 2008 flyby through Mercury's magnetosphere,
1755 *Geophys. Res. Lett., 36*, L01104, doi:10.1029/2008GL036034.
1756 Boardsen, S. A., T. Sundberg, J. A. Slavin, B. J. Anderson, H. Korth, S. C. Solomon,
1757 and L. G. Blomberg (2010), Observations of Kelvin-Helmholtz waves along the
1758 dusk-side boundary of Mercury's magnetosphere during MESSENGER's third
1759 flyby, *Geophys. Res. Lett., 37*, L12101, doi:10.1029/2010GL043606.
1760 Boardsen, S. A., J. A. Slavin, B. J. Anderson, H. Korth, D. Schriver, and S. C.
1761 Solomon (2012), Survey of coherent ~1 Hz waves in Mercury's inner
1762 magnetosphere from MESSENGER observations, *J. Geophys. Res., 117*, A00M05,
1763 doi:10.1029/2012JA017822.
1764 Borin, P., M. Bruno, G. Cremonese, F. Marzari (2010), Estimate of the neutral atoms'
1765 contribution to the Mercury exosphere caused by a new flux of micrometeoroids,
1766 *Astronom. and Astrophys., 517*, A89.
1767 Broadfoot, A. L., S. Kumar, and M. J. S. Belton (1974), Mercury's atmosphere from
1768 Mariner 10: Preliminary results, *Science, 185*, 166–169.
1769 Broadfoot, A. L., D. E. Shemansky, and S. Kumar (1976), Mariner 10: Mercury
1770 atmosphere. *Geophys. Res. Lett., 3*, 577–580.
1771 Broadfoot, A. L., S. S. Clapp, and F. E. Stuart (1977), Mariner 10 ultraviolet
1772 spectrometer: airglow experiment, *Space Sci. Instrum., 3*, 199–208.
1773 Bruno, M., G. Cremonese, and S. Marchi (2007), Neutral sodium atoms release from
1774 the surfaces of the Moon and Mercury induced by meteoroid impacts, *Planet.*
1775 *Space Sci. 55*, 1494–1501.
1776 Büchner, J., and L. M. Zelenyi (1989), Regular and chaotic charged particle motion in
1777 magnetotaillike field reversals: 1. Basic theory of trapped motion, *J. Geophys.*
1778 *Res., 94*, 11,821–11,842, doi:10.1029/JA094iA09p11821.
1779 Burger, M. H., R. M. Killen, R. J. Vervack, E. T. Bradley, W. E. McClintock, M.
1780 Sarantos, M. Benna, and N. Mouawad (2010), Monte Carlo modeling of sodium in
1781 Mercury's exosphere during the first two MESSENGER flybys, *Icarus, 209*, 63–
1782 74, doi: 10.1016/j.icarus.2010.05.007.
1783 Burger, M. H., R. M. Killen, W. E. McClintock, R. J. Vervack Jr., A. W. Merkel, A.
1784 L. Sprague, and M. Sarantos (2012), Modeling MESSENGER observations of
1785 calcium in Mercury's exosphere, *J. Geophys. Res., 117*, E00L11,
1786 doi:10.1029/2012JE004158.
1787 Burger, M. H., R. M. Killen, W. E. McClintock, A. W. Merkel, R. J. Vervack, Jr., T.
1788 A. Cassidy, and M. Sarantos (2014), Seasonal variations in Mercury's dayside
1789 calcium exosphere, *Icarus, 238*, 51–58.

1790 Burlaga, L. F. (2001), Magnetic fields and plasmas in the inner heliosphere: Helios
1791 results, *Planet. Space Sci., 49*, 1619–1627.
1792 Caan, M. N., R. L. Mcpherron, and C. T. Russell (1973), Solar wind and substorm-
1793 related changes in lobes of geomagnetic tail, *J. Geophys. Res., 78*, 8087–8096.
1794 Cassidy, T. A., A. W. Merkel, M. H. Burger, M. Sarantos, R. M. Killen, W. E.
1795 McClintock, and R. J. Vervack (2015), Mercury's seasonal sodium exosphere:
1796 MESSENGER orbital observations, Icarus, 248, 547-559, doi:
1797 10.1016/j.icarus.2014.10.037.
1798 Christon, S. P., J. Feynman, and J. A. Slavin, Dynamic substorm injections – Similar
1799 magnetospheric phenomena at Earth and Mercury, in *Magnetotail Physics*, edited
1800 by A. T. Y. Lui, pp. 393–400, Johns Hopkins Univ. Press, Baltimore, MD, 1987.
1801 Cintala, M. J. (1992), Impact induced thermal effects in the lunar and Mercurian
1802 regoliths, *J. Geophys. Res., 97*, 947–973.
1803 Cladis, J. B. (1986), Parallel acceleration and transport of ions from polar ionosphere
1804 to plasma sheet, *Geophys. Res. Lett., 13*, 893.
1805 Cladis, J. B., H. L. Collin, O. W. Lennartsson, T. E. Moore, W. K. Peterson, and C. T.
1806 Russell (2000), Observations of centrifugal acceleration during compression of
1807 magnetosphere, *Geophys. Res. Lett., 27*, 915.
1808 Cowley, S. W. H. (1982), The causes of convection in the Earth's magnetosphere: A
1809 review of developments during the IMS, *J. Geophys. Res., 20*, 531 – 565.
1810 Cowley, S. W. H., The distant geomagnetic tail in theory and observation, *AGU*
1811 *Monograph on "Magnetic reconnection in space and laboratory plasmas", vol. 30*,
1812 p. 228, 1984.
1813 Cremonese, G., M. Bruno, V. Mangano, S. Marchi, and A. Milillo (2005), Release of
1814 neutral sodium atoms from the surface of Mercury induced by meteoroid impacts,
1815 *Icarus, 177,* 122–128.
1816 Delcourt, D. C. (2002), Particle acceleration by inductive electric fields in the inner
1817 magnetosphere, *J. Atm. Solar Ter. Phys., 64*, 551.
1818 Delcourt, D. C. (2013), On the supply of heavy planetary material to the magnetotail
1819 of Mercury, *Ann. Geophys., 31*, 1673.
1820 Delcourt, D. C., T. E. Moore, and M.-C. Fok (2011), On the effect of IMF turning on
1821 ion dynamics at Mercury, *Ann. Geophys., 29*, 987.
1822 Delcourt, D. C., J.-A. Sauvaud, R. F. Martin Jr., and T. E. Moore (1996), On the
1823 nonadiabatic precipitation of ions from the near-Earth plasma sheet, *J. Geophys.*
1824 *Res., 101*, 17,409.
1825 Delcourt, D. C., T. E. Moore, S. Orsini, A. Millilo, and J.-A. Sauvaud (2002),
1826 Centrifugal acceleration of ions near Mercury, *Geophys. Res. Lett., 29*, 32, doi:
1827 10.1029/2001GL013829.
1828 Delcourt, D. C., S. Grimald, F. Leblanc, J.-J. Berthelier, A. Millilo, A. Mura, S.
1829 Orsini, and T. E. Moore (2003), A quantitative model of the planetary Na+
1830 contribution to Mercury's magnetosphere, *Ann. Geophys., 21*, 1723–1736,
1831 doi:10.5194/angeo-21-1723-2003.
1832 Delcourt, D. C., K. Seki, N. Terada, and T. E. Moore (2012), Centrifugally stimulated
1833 exospheric ion escape at Mercury, *Geophys. Res. Lett., 39*, L22105,
1834 doi:10.1029/2012GL054085.
1835 DiBraccio, G. A., J. A. Slavin, S. A Boardsen, B. J. Anderson, H. Korth, T. H.
1836 Zurbuchen, J. M. Raines, D. N. Baker, R. L. McNutt Jr., and S. C. Solomon
1837 (2013), MESSENGER observations of magnetopause structure and dynamics at
1838 Mercury, *J. Geophys. Res. Space Physics, 118*, 997–1008, doi:10.1002/jgra.50123.

1839 DiBraccio, G. A., J. A. Slavin, S. M. Imber, D. J. Gershman, J. M. Raines, C. M.
1840 Jackman, S. A. Boardsen, B. J. Anderson, H. Korth, T. H. Zurbuchen, R. L.
1841 McNutt, Jr., and S. C. Solomon (2014), MESSENGER observations of flux ropes
1842 in Mercury's magnetotail, *Planet. Space Sci.*, doi:10.1016/j.pss.2014.12.016.
1843 DiBraccio, G. A., J. A. Slavin, J. M. Raines, D. J. Gershman, P. J. Tracy, S. A.
1844 Boardsen, T. H. Zurbuchen, B. J. Anderson, H. Korth, R. L. McNutt Jr., and S. C.
1845 Solomon, First observations of Mercury's plasma mantle as seen by
1846 MESSENGER, in prep.
1847 Domingue, D. L., A. L. Sprague, and D. M. Hunten, (1997), Dependence of
1848 Mercurian atmospheric column abundance estimations on surface-reflectance
1849 modeling, *Icarus, 128*, 75–82.
1850 Domingue, D. L., P. L. Koehn, R. M. Killen, A. L. Sprague, M. Sarantos, A. F.
1851 Cheng, E. T. Bradley, and W. E. McClintock (2007), Mercury's atmosphere: A
1852 surface-bounded exosphere, *Space Sci. Rev., 131*, 161–186.
1853 Doressoundiram, A., F. Leblanc, C. Foellmi, and S. Erard (2009), Metallic species in
1854 Mercury's exosphere: EMMI/New technology telescope observations, *Astron. J.,*
1855 *137*, 3859–3863.
1856 Dungey, J. W. (1961), Interplanetary magnetic field and the auroral zones, *Phys. Rev.*
1857 *Lett., 6*, 47–48, doi:10.1103/PhysRevLett.6.47.
1858 Elphic, R. C., H. O. Funsten, B. L. Barraclough, D. J. McComas,M. T. Paffet, D. T.
1859 Vaniman, and G. Heiken (1991), Lunar surface composition and solar wind-
1860 induced secondary ion mass spectrometry, *Geophys. Res. Lett., 18*, 2165–2168,
1861 doi:10.1029/91GL02669.
1862 Eraker, J. H., and J. A. Simpson (1986), Acceleration of charged particles in
1863 Mercury's magnetosphere, *J. Geophys. Res., 91*, 9973–9993,
1864 doi:10.1029/JA091iA09p09973.
1865 Fairfield, D. H. (1971), Average and unusual locations for the Earth's magnetopause
1866 and bow shock, *J. Geophys. Res., 76*, 6700–6716, doi:10.1029/JA076i028p06700.
1867 Farrell, W. M., J. S. Halekas, R. M. Killen, G. T. Delory, N. Gross, L. V. Bleacher, D.
1868 Krauss-Varben, P. Travnicek, D. Hurley, T. J. Stubbs, M. I. Zimmerman, and T. L.
1869 Jackson (2012), Solar-Storm/Lunar Atmosphere Model (SSLAM): An overview of
1870 the effort and description of the driving storm environment, *J. Geophys. Res., 117*,
1871 E00K04, doi:10.1029/2012JE004070.
1872 Fjelbo, G., A. Kliore, D. Sweetnam, P. Esposito, B. Seidel, and T. Howard (1976),
1873 The occultation of Mariner 10 by Mercury, *Icarus, 29*, 407–415,
1874 doi:10.1016/0019-1035(76)90063-4.
1875 Gershman, D. J., T. H. Zurbuchen, L. A. Fisk, J. A. Gilbert, J. M. Raines, B. J.
1876 Anderson, C. W. Smith, H. Korth, and S. C. Solomon (2012), Solar wind alpha
1877 particles and heavy ions in the inner heliosphere observed with MESSENGER, *J.*
1878 *Geophys. Res., 117*, A00M02, doi:10.1029/2012JA017829.
1879 Gershman, D. J., J. A. Slavin, J. M. Raines, T. H. Zurbuchen, B. J. Anderson, H.
1880 Korth, D. N. Baker, and S. C. Solomon (2013), Magnetic flux pileup and plasma
1881 depletion in Mercury's subsolar magnetosheath, *J. Geophys. Res., 118,*
1882 doi:10.1002/2013JA019244.
1883 Gershman, D. J., J. A. Slavin, J. M. Raines, T. H. Zurbuchen, B. J. Anderson, H.
1884 Korth, D. N. Baker, and S. C. Solomon (2014), Ion kinetic properties in Mercury's
1885 premidnight plasma sheet, *Geophys. Res. Lett., 41*, 5740–5747,
1886 doi:10.1002/2014GL060468.
1887 Gershman, D. J., J. M. Raines, J. A. Slavin, T. H. Zurbuchen, T. Sundberg, S. A.
1888 Boardsen, B. J. Anderson, H. Korth, and S. C. Solomon, MESSENGER

observations of multi-scale Kelvin-Helmholtz vortices at Mercury, *J. Geophys. Res. Space Physics*, in revision.
Glassmeier, K.-H., J. Grosser, U. Auster, D. Constantinescu, Y. Narita, and S. Stellmach (2007), Electromagnetic induction effects and dynamo action in the Hermean system, *Space Sci. Rev., 132*, 511–527, doi:10.1007/s11214-007-9244-9.
Hapke, B. (1981), Bidirectional reflectance spectroscopy: 1. Theory, *J. Geophys. Res., 86,* 3039–3054.
Hapke, B. (1984), Bidirectional reflectance spectroscopy: 3. Correction for macroscopic roughness, *Icarus, 59*, 41–59.
Hapke, B. (1986), Bidirectional reflectance spectroscopy: 4. The extinction coefficient and the opposition effect, *Icarus, 67*, 264–280.
Hesse, M. and Kivelson, M. G. (1998), The Formation and Structure of Flux Ropes in the Magnetotail, in *New Perspectives on the Earth's Magnetotail* (eds A. Nishida, D.N. Baker and S.W.H. Cowley), American Geophysical Union, Washington, D. C., doi:10.1029/GM105p0139
Hidalgo, M. A., C. Cid, A. F. Vinas, and J. Sequeiros (2002a), A non-force-free approach to the topology of magnetic clouds in the solar wind, *J. Geophys. Res., 107*, 1002, doi:10.1029/2001JA900100.
Hidalgo, M. A., T. Nieves-Chinchilla, and C. Cid (2002b), Elliptical cross-section model for the magnetic topology of magnetic clouds, *Geophys. Res. Lett., 29*, 1637, doi:10.1029/2001GL013875.
Hill, T. W., A. J. Dessler, and R. A. Wolf (1976), Mercury and Mars: The role of ionospheric conductivity in the acceleration of magnetospheric particles, *Geophys. Res. Lett., 3*, 429–432, doi:10.1029/GL003i008p00429.
Ho, G. C., S. M. Krimigis, R. E. Gold, D. N. Baker, B. J. Anderson, H. Korth, J. A. Slavin, R. L. McNutt Jr., R. M. Winslow, and S. C. Solomon (2012), Spatial distribution and spectral characteristics of energetic electrons in Mercury's magnetosphere, *J. Geophys. Res., 117*, A00M04, doi:10.1029/2012JA017983.
Hones, E. W., J. Birn, D. N. Baker, S. J. Bame, W. C. Feldman, D. J. Mccomas, R. D. Zwickl, J. A. Slavin, E. J. Smith, and B. T. Tsurutani (1984), Detailed examination of a plasmoid in the distant magnetotail with ISEE-3, *Geophys. Res. Lett., 11,* 1046–1049.
Hood, L. L., and G. Schubert (1979), Inhibition of solar wind impingement on Mercury by planetary induction currents, *J. Geophys. Res. 84,* 2641–2647.
Horwitz, J. L. (1984), Features of ion trajectories in the polar magnetosphere, *Geophys. Res. Lett., 11*, 1111.
Huang, C.-S., A. D. DeJong, and X. Cai (2009), Magnetic flux in the magnetotail and polar cap during sawteeth, isolated substorms, and steady magnetospheric convection events, *J. Geophys. Res., 114*, A07202, doi:10.1029/2009JA014232.
Huebner, W. F., J. J. Keady, and S. P. Lyon (1992), Solar photo rates for planetary atmospheres and atmospheric pollutants, *Astrophys. Space Sci.*, *195*, 1–289.
Hunten, D. M., T. H. Morgan, and D. E. Shemansky (1988), The Mercury atmosphere, in *Mercury*, edited by F. Vilas, C. R. Chapman, and M. S. Matthews, pp. 562 – 612, Univ. of Ariz. Press, Tucson.
Ieda, A., S. Machida, T. Mukai, Y. Saito, T. Yamamoto, A. Nishida, T. Terasawa, and S. Kokubun (1998), Statistical analysis of the plasmoid evolution with Geotail observations, *J. Geophys. Res., 103*, 4453–4465.
Imber, S. M., J. A. Slavin, H. U. Auster, and V. Angelopoulos (2011), A THEMIS survey of flux ropes and traveling compression regions: Location of the near-Earth

1938 reconnection site during solar minimum, *J. Geophys. Res., 116*, A02201,
1939 doi:10.1029/2010JA016026.
1940 Imber, S. M., J. A. Slavin, S. A. Boardsen, B. J. Anderson, H. Korth, R. L. McNutt Jr.
1941 and S. C. Solomon (2014), MESSENGER observations of large dayside flux
1942 transfer events: Do they drive Mercury's substorm cycle?, *J. Geophys. Res Space*
1943 *Physics, 119*, 5613–5623, doi:10.1002/2014JA019884.
1944 Ip, W. H. and A. Kopp (2002), MHD simulations of the solar wind interaction with
1945 Mercury, *J. Geophys. Res., 107,* 1348, doi:10.1029/2001JA009171.
1946 Jia, X., J. A. Slavin, T. I. Gombosi, L. Daldorff, and G. Toth (2013), Global MHD
1947 simulations of Mercury's interaction with the solar wind: Influence of the
1948 planetary conducting core on the magnetospheric interaction, AGU Fall Meeting
1949 Abstracts, A2139- doi:
1950 Johnson, R. E. and R. Baragiola (1991), Lunar surface: Sputtering and secondary ion
1951 mass spectrometry, *Geophys. Res. Lett., 18*, 2169–2172.
1952 Kabin, K., T. I. Gombosi, D. L. DeZeeuw, and K. G. Powell (2000), Interaction of
1953 Mercury with the solar wind, *Icarus, 143*, 397–406.
1954 Kallio, E., and P. Janhunen (2003), Modelling the solar wind interaction with
1955 Mercury by a quasi-neutral hybrid model, *Ann. Geophys., 21*, 2133.
1956 Kameda, S., I. Yoshikawa, M. Kagitani, and S. Okano (2009), Interplanetary dust
1957 distribution and temporal variability of Mercury's atmospheric Na, *Geophys. Res.*
1958 *Lett., 36*, L15201, doi:10.1029/2009GL039036.
1959 Kidder, A., R. M. Winglee, and E. M. Harnett (2008), Erosion of the dayside
1960 magnetosphere at Mercury in association with ion outflows and flux rope
1961 generation, *J. Geophys. Res., 113*, A09223, doi:10.1029/2008JA013038.
1962 Killen, R. M. and W. H. Ip (1999), The surface-bounded atmospheres of mercury and
1963 the moon, *Rev. Geophys.*, *37*, 361–406.
1964 Killen, R. M. and J. M. Hahn (2015), Impact vaporization as a possible source of
1965 Mercury's calcium exosphere, Icarus, 250, 230-237, doi:
1966 10.1016/j.icarus.2014.11.035.
1967 Killen, R. M., A. E. Potter, P. Reiff, M. Sarantos, B. V. Jackson, P. Hick, B. Giles
1968 (2001), Evidence for space weather at Mercury, *J. Geophys. Res., 106*, 20,509–
1969 20,525.
1970 Killen, R. M., M. Sarantos, A. E. Potter, and P. Reiff (2004), Source rates and ion
1971 recycling rates for Na and K in Mercury's atmosphere, *Icarus, 171*, 1–19.
1972 Killen, R., G. Cremonese, H. Lammer, S. Orsini, A. E. Potter, A. L. Sprague, P.
1973 Wurz, M. Khodachenko, H. I. M. Lichtenegger, A. Milillo, and A. Mura (2007),
1974 Processes that Promote and Deplete the Exosphere of Mercury, *Space Sci. Rev.*
1975 *132*, 433–509.
1976 Killen, R., D. Shemansky, and N. Mouawad (2009), Expected emission from
1977 Mercury's exospheric species, and their ultraviolet-visible signatures, *Astrophys. J.*
1978 *Suppl., 181*, 351–359.
1979 Kivelson, M. G. and A. J. Ridley (2008), Saturation of the polar cap potential:
1980 Inference from Alfven wing arguments, *J. Geophys. Res., 113*, A05214,
1981 doi:10.1029/2007JA012302.
1982 Korth, H., B. J. Anderson, J. M. Raines, J. A. Slavin, T. H. Zurbuchen, C. L. Johnson,
1983 M. E. Purucker, R. M. Winslow, S. C. Solomon, and R. L. McNutt Jr. (2011),
1984 Plasma pressure in Mercury's equatorial magnetosphere derived from
1985 MESSENGER Magnetometer observations, *Geophys. Res. Lett.*, *38*, L22201-
1986 doi: 10.1029/2011GL049451.

1987 Korth, H., B. J. Anderson, D. J. Gershman, J. M. Raines, J. A. Slavin, T. H.
1988 Zurbuchen, S. C. Solomon, and R. L. McNutt Jr. (2014), Plasma distribution in
1989 Mercury's magnetosphere derived from MESSENGER Magnetometer and Fast
1990 Imaging Plasma Spectrometer observations, *J. Geophys. Res. Space Physics, 119*,
1991 2917–2932, doi:10.1002/2013JA019567.
1992 Kuznetsova, M. M., M. Hesse, L. Rastätter, A. Taktakishvili, G. Toth, D. L.
1993 DeZeeuw, A. Ridley, and T. I. Gombosi (2007), Multiscale modeling of
1994 magnetospheric reconnection, *J. Geophys. Res., 112*, A10210,
1995 doi:10.1029/2007JA012316.
1996 Lammer, H., P. Wurz, M. R. Patel, R. M. Killen, C. Kolb, S. Massetti, S. Orsini, and
1997 A. Milillo (2003), The variability of Mercury's exosphere by particle and radiation
1998 induced surface release processes, *Icarus, 166*, 238–247.
1999 Lavraud, B., H. Rème, M. W. Dunlop, J.-M. Bosqued, I. Dandouras, J.-A. Sauvaud,
2000 A. Keiling, T. D. Phan, R. Lundin, P. J. Cargill, C. P. Escoubet, C. W. Carlson, J.
2001 P. MacFadden, G. K. Parks, E. Moebius, L. M. Kistler, E. Amata, M.-B.
2002 Bavassano-Cattaneo, A. Korth, B. Klecker, and A. Balogh (2005), Cluster observes
2003 the high-altitude cusp region, *Surv. Geophys., 26*, 135–175, doi:10.1007/s10712-
2004 005-1875-3.
2005 Leblanc, F., and R. E. Johnson (2003), Mercury's sodium exosphere, *Icarus, 164*,
2006 261–281, doi:10.1016/S0019-1035(03)00147-7.
2007 Leblanc, F., and R. E. Johnson (2010), Mercury exosphere I. Global circulation model
2008 of its sodium component, *Icarus, 209*, 280–300.
2009 Leblanc, F. and J. Y. Chaufray (2011), Mercury and Moon He exospheres: Analysis
2010 and modeling, *Icarus, 216*, 551–559.
2011 Leblanc, F., E. Chassefiere, R. E. Johnson, D. M. Hunten, E. Kallio, D. C. Delcourt,
2012 R. M. Killen, J. G. Luhmann, A. E. Potter, A. Jambon, G. Crernonese, M.
2013 Mendillo, N. Yan, A. L. Sprague (2007), Mercury's exosphere origins and
2014 relations to its magnetosphere and surface, *Planet. Space Sci., 55*, 1069–1092.
2015 Leblanc, F., A. Doressoundiram, N. Schneider, V. Mangano, A. L. Ariste, C. Lemen,
2016 B. Gelly, C. Barbieri, G. Cremonese, (2008), High latitude peaks in Mercury's
2017 sodium exosphere: Spectral signature using THEMIS solar telescope, *Geophys.*
2018 *Res. Lett., 35*, L18204, doi:10.1029/2008GL035322.
2019 Leblanc, F., A. Doressoundiram, N. Schneider, S. Massetti, M. Wedlund, A. López,
2020 Ariste, C. Barbieri, V. Mangano, and G. Cremonese (2009), Short-term variations
2021 of Mercury's Na exosphere observed with very high spectral resolution, *Geophys.*
2022 *Res. Lett. 36*, L07201.
2023 Lepping, R. P., J. A. Jones, and L. F. Burlaga (1990), Magnetic field structure of
2024 interplanetary magnetic clouds at 1 Au, *J. Geophys. Res., 95*, 11,957–11,965.
2025 Lepping, R. P., D. H. Fairfield, J. Jones, L. A. Frank, W. R. Paterson, S. Kokubun,
2026 and T. Yamamoto (1995), Cross-tail magnetic flux ropes as observed by the
2027 Geotail spacecraft, *Geophys. Res. Lett., 22*, 10, 1193–1196.
2028 Lepping, R. P., J. A. Slavin, M. Hesse, J. A. Jones, and A. Szabo (1996), Analysis of
2029 magnetotail flux ropes with strong core fields: ISEE 3 observations, *J. Geomag.*
2030 *Geoelec., 48*,589–601.
2031 Liljeblad, E., T. Sundberg, T. Karlsson, and A. Kullen (2014), Statistical
2032 investigation of Kelvin-Helmholtz waves at the magnetopause of Mercury, *J.*
2033 *Geophys. Res. (Space Physics)*, *119*, 9670-9683, doi: 10.1002/2014JA020614.
2034 Mall, U., E. Kirsch, K. Cierpka, B. Wilken, A. Söding, F. Neubauer, G. Gloeckler,
2035 and A. Galvin (1998), Direct observation of lunar pick-up ions near the Moon,
2036 *Geophys. Res. Lett., 25*, 3799–3802, doi:10.1029/1998GL900003.

2037 Mangano, V., A. Milillo, A. Mura, S. Orsini, E. De Angelis, A.M. Di Lellis, and P.
2038 Wurz (2007), The contribution of impulsive meteoritic impact vapourization to the
2039 Hermean exosphere, *Planet. Space Sci., 55*, 1541–1556.
2040 Mangano, V., S. Massetti, A. Milillo, A. Mura, S. Orsini, and F. Leblanc (2013),
2041 Dynamical evolution of sodium anisotropies in the exosphere of Mercury, *Planet.*
2042 *Space Sci., 82-83*, 1–10.
2043 Massetti, S., S. Orsini, A. Milillo, A. Mura, E. De Angelis, H. Lammer, and P. Wurz
2044 (2003), Mapping of the cusp plasma precipitation on the surface of Mercury,
2045 *Icarus, 166*, 229–237.
2046 Masters, A., J. A. Slavin, G. A. DiBraccio, T. Sundberg, R. M. Winslow, C. L.
2047 Johnson, B. J. Anderson, and H. Korth (2013), A comparison of magnetic
2048 overshoots at the bow shocks of Mercury and Saturn, *J. Geophys. Res., 118*,
2049 doi:10.1002/jgra.50428.
2050 McClintock, W. E., R. J. Vervack, E. T. Bradley, R. M. Killen, N. Mouawad, A. L.
2051 Sprague, M. H. Burger, S. C. Solomon, and N. R. Izenberg (2009), MESSENGER
2052 observations of Mercury's exosphere: Detection of magnesium and distribution of
2053 constituents, *Science, 324*, 610–613.
2054 McGrath, M. A., R. E. Johnson, and L. J. Lanzerotti (1986), Sputtering of sodium on
2055 the planet Mercury, *Nature, 323*, 694–696.
2056 McLain, J. L., A. L. Sprague, G. A. Grieves, D. Schriver, P. Travnicek, and T. M.
2057 Orlando (2011), Electron-stimulated desorption of silicates: A potential source for
2058 ions in Mercury's space environment, *J. Geophys. Res., 116*, E03007,
2059 doi:10.1029/2010JE003714.
2060 McPherron, R. L., C. T. Russell, and M. P. Aubry (1973), Satellite studies of
2061 magnetospheric substorms on August 15, 1968: 9. Phenomenological model for
2062 substorms, *J. Geophys. Res., 78*, 3131–3149, doi:10.1029/JA078i016p03131.
2063 Milan, S. E., S. W. H. Cowley, M. Lester, D. M. Wright, J. A. Slavin, M. Fillingim,
2064 C. W. Carlson, and H. J. Singer (2004), Response of the magnetotail to changes in
2065 the open flux content of the magnetosphere, *J. Geophys. Res., 109*, A04220,
2066 doi:10.1029/2003JA010350.
2067 Milillo, A., et al. (2010), The BepiColombo mission: An outstanding tool for
2068 investigating the Hermean environment, *Planet. Space Sci., 58*, 40–60.
2069 Mitchell, D. G., D. J. Williams, C. Y Huang, L. A. Frank, and C. T. Russell (1990),
2070 Current carriers in the near-Earth cross-tail current sheet during substorm growth
2071 phase, *Geophys. Res. Lett., 17*, 583.
2072 Moldwin, M. B. and W. J. Hughes (1992), On the formation and evolution of
2073 plasmoids: A survey of Isee-3 Geotail data, *J. Geophys. Res., 97,* 19,259–19,282.
2074 Mouawad, N., Burger, M. H. Killen, R. M. Potter, A. E. McClintock, W. E. Vervack,
2075 R. J. Bradley, E. T. Benna, M. Naidu, S. (2011), Constraints on Mercury's Na
2076 exosphere: Combined MESSENGER and ground-based data, *Icarus, 211*, 21–36.
2077 Müller, J., S. Simon, Y.-C. Wang, U. Motschmann, D. Heyner, J. Schüle, W.-H. Ip,
2078 G. Kleindienst, and G. J. Pringle (2012), Origin of Mercury's double
2079 magnetopause: 3D hybrid simulation study with A.I.K.E.F., *Icarus, 218*, 666–687,
2080 doi:10.1016/j.icarus.2011.12.028.
2081 Müller, M., S. F. Green, N. McBride, D. Koschny, J. C. Zarnecki, and M. S. Bentley
2082 (2002), Estimation of the dust flux near Mercury, *Planet. Space Sci., 50*, 1101–
2083 1115.
2084 Mura, A., A. Milillo, S. Orsini, and S. Massetti (2007), Numerical and analytical
2085 model of Mercury's exosphere: Dependence on surface and external conditions,
2086 *Planet. Space Sci., 55*, 1569–1583.

Mura, A., P. Wurz, H. I. M. Lichtenegger, H. Schleicher, H. Lammer, D. Delcourt, A. Milillo, S. Massetti, M. L. Khodachenko, and S. Orsini (2009), The sodium exosphere of Mercury: Comparison between observations during Mercury's transit and model results, *Icarus, 200*, 1–11.

Ness, N. F., K. W. Behannon, R. P. Lepping, Y. C. Whang, and K. H. Schatten (1974), Magnetic field observations near Mercury: Preliminary Results from Mariner 10, *Science, 185*, 151–160.

Ogilvie, K. W., J. D. Scudder, R. E. Hartle, G. L. Siscoe, H. S.Bridge, A. J. Lazarus, J. R. Asbridge, S. J. Bame, and C. M. Yeates (1974), Observations at Mercury encounter by Plasma Science Experiment on Mariner 10, *Science, 185*, 145–151.

Ogilvie, K. W., J. D. Scudder, V. M. Vasyliunas, R. E. Hartle, and G. L. Siscoe (1977), Observations at planet Mercury by Plasma Electron Experiment: Mariner 10, *J. Geophys. Res., 82*, 1807–1824.

Orsini, S., S. Livi, K. Torkar, S. Barabash, A. Milillo, P. Wurz, A. M. Di Lellis, E. Kallio and the SERENA team (2010)Mg, , **"SERENA: *a*A suite of four instruments (ELENA, STROFIO, PICAM and MIPA) on board BepiColombo-MPO for particle detection in the Hermean Environment**, BepiColombo Special Issue on Planetary and**,"** Planet. Space Science, doi:10.1016/j.pss.2008.09.012,Sci. 58, (2010) 166-181,

Orsini, S., V. Mangano, A. Mura, D. Turrini, S. Massetti, A. Milillo, and C. Plainaki (2014), The influence of space environment on the evolution of Mercury, *Icarus, 239*, 281–290.

Paral, J., P. M. Trávníček, K. Kabin, R. Rankin, and T. H. Zurbuchen (2009), Spatial distribution and energy spectrum of heavy ions in the Hermean magnetosphere with applications to MESSENGER flybys, *Adv. Geosci.*, *15*, 1–16.

Paral, J., P. M. Trávníček, R. Rankin, and D. Schriver (2010), Sodium ion exosphere of Mercury during MESSENGER flybys, *Geophys. Res. Lett., 37*, L19102, doi:10.1029/2010GL044413.

Paral, J. and R. Rankin (2013), Dawn-dusk asymmetry in the Kelvin-Helmholtz instability at Mercury, *Nature Communications*, 4, 1645- doi: 10.1038/ncomms2676.

Pfleger, M., H.I.M. Lichtenegger, P. Wurz, H. Lammer, E. Kallio, M. Alho, A. Mura, J.A. Martín-Fernández, M.L. Khodachenko, and S. McKenna-Lawlor, **"3D-modeling of Mercury's solar wind sputtered surface-exosphere environment,"** Planet. Sp. Sci. (2015), submitted.

Poppe, A. R., J. S. Halekas, M. Sarantos, G. T. Delory (2013), The self-sputtered contribution to the lunar exosphere, *J. Geophys. Res., 118*, 1934–1944.

Potter, A., and T. H. Morgan (1985), Discovery of sodium in the atmosphere of Mercury, *Science, 229*, 651–653.

Potter, A., and T. H. Morgan (1986), Potassium in the atmosphere of Mercury, *Icarus 67*, 336–340.

Potter, A., and T. H. Morgan (1997), Sodium and potassium atmospheres of Mercury, *Planet. Space Sci., 45*, 95–100.

Potter, A., R. M. Killen, and T. H. Morgan (1999), Rapid changes in the sodium exosphere of Mercury, *Planet. Space Sci., 47*, 1441–1448.

Potter, A. E., R. M. Killen, and M. Sarantos (2006), Spatial distribution of sodium on Mercury, *Icarus, 181*, 1–12.

Potter, A., R. M. Killen, and T. H. Morgan (2002), The sodium tail of Mercury, *Meteor. Planet. Sci., 37*, 1165–1172.

2136 Potter, A. E., R. M. Killen, and T. H. Morgan (2007), Solar radiation acceleration
2137 effects on Mercury sodium emission, *Icarus*, *186*, 571–580.
2138 Raeder, J., P. Zhu, Y. Ge, and G. Siscoe (2010), Open Geospace General Circulation
2139 Model simulation of a substorm: Axial tail instability and ballooning mode
2140 preceding substorm onset, *J. Geophys. Res., 115*, A00I16,
2141 doi:10.1029/2010JA015876.
2142 Raines, J. M., J. A. Slavin, T. H. Zurbuchen, G. Gloeckler, B. J. Anderson, D. N.
2143 Baker, H. Korth, S. M. Krimigis, and R. L. McNutt Jr. (2011), MESSENGER
2144 observations of the plasma environment near Mercury, *Planet. Space Sci., 59*,
2145 2004–2015, doi:10.1016/j.pss.2011.02.004.
2146 Raines, J. M., D. J. Gershman, T. H. Zurbuchen, M. Sarantos, J. A. Slavin, J. A.
2147 Gilbert, H. Korth, B. J. Anderson, G. Gloeckler, S. M. Krimigis, D. N. Baker, R. L.
2148 McNutt Jr., and S. C. Solomon (2013), Distribution and compositional variations
2149 of plasma ions in Mercury's space environment: The first three Mercury years of
2150 MESSENGER observations, *J. Geophys. Res. Space Physics, 118*, 1604–1619,
2151 doi:10.1029/2012JA018073.
2152 Raines, J. M., D. J. Gershman, J. A. Slavin, T. H. Zurbuchen, H. Korth, B. J.
2153 Anderson, and S. C. Solomon (2014), Structure and dynamics of Mercury's
2154 magnetospheric cusp: MESSENGER measurements of protons and planetary ions,
2155 *J. Geophys. Res. Space Physics, 119*, 6587–6602, doi:10.1002/2014JA020120.
2156 Richer, E., R. Modolo, C. Chanteur, S. Hess, and F. Leblanc (2012), A global hybrid
2157 model for Mercury's interaction with the solar wind: Case study of the dipole
2158 representation, *J. Geophys. Res., 117*, doi:10.1029/2012JA017898.
2159 Runov, A., V. Angelopoulos, X.-Z. Zhou, X.-J. Zhang, S. Li, F. Plaschke, and J.
2160 Bonnell (2011), A THEMIS multicase study of dipolarization fronts in the
2161 magnetotail plasma sheet, *J. Geophys. Res., 116*, A05216,
2162 doi:10.1029/2010JA016316.
2163 Russell, C. T., and R. J. Walker (1985), Flux transfer events at Mercury, *J. Geophys.*
2164 *Res., 90*, 11067.
2165 Russell, C. T., D. N. Baker, and J. A. Slavin, The magnetosphere of Mercury, in
2166 *Mercury*, edited by F. Vilas, C. R. Chapman, and M. S. Matthews, pp. 514–561,
2167 Univ. of Ariz. Press, Tucson, 1988.
2168 Russell, C. T. (1989), ULF waves in the Mercury magnetosphere, *Geophys. Res. Lett.*,
2169 *16*, 1253-1256, doi: 10.1029/GL016i011p01253.
2170 Sarantos, M., P. H. Reiff, T. W. Hill, R. M. Killen, A. L. Urquhart (2001), A B_X-
2171 interconnected magnetosphere model for Mercury, *Planet. Space Sci., 49*, 1629–
2172 1635.
2173 Sarantos, M., J. A. Slavin, M. Benna, S. A. Boardsen, R. M. Killen, D. Schriver, and
2174 P. Trávníček (2009), Sodium-ion pickup observed above the magnetopause during
2175 MESSENGER's first Mercury flyby: Constraints on neutral exospheric models,
2176 *Geophys. Res. Lett., 36*, L04106, doi:10.1029/2008GL036207.
2177 Sarantos, M., R. M. Killen, W. E. McClintock, E. T. Bradley, R. J. Vervack, M.
2178 Benna, and J. A. Slavin (2011), Limits to Mercury's magnesium exosphere from
2179 MESSENGER second flyby observations, *Planet. Space Sci., 59*, 1992–2003.
2180 Sarantos, M., Hartle, R. E., Killen, R. M., Saito, Y., J. A., Slavin, and A. Glocer
2181 (2012), Flux estimates of ions from the lunar exosphere. *Geophys. Res. Lett., 39*,
2182 L13101, doi:10.1029/2012GL052001.
2183 Schmidt, C. A. (2013), Monte Carlo modeling of north-south asymmetries in
2184 Mercury's sodium exosphere, *J. Geophys. Res., 118*, 4564–4571,
2185 doi:10.1002/jgra.50396.

2186 Schmidt, C. A., J. Baumgardner, M. Mendillo, and J. K. Wilson (2012), Escape rates
2187 and variability constraints for high-energy sodium sources at Mercury, *J. Geophys.*
2188 *Res., 117*, A03301, doi:10.1029/2011JA017217.
2189 Seki, K., N. Terada, M. Yagi, D. C. Delcourt, F. Leblanc, and T. Ogino (2013),
2190 Effects of the surface conductivity and IMF strength on the dynamics of planetary
2191 ions in Mercury's magnetosphere, *J. Geophys. Res.*, *118*, doi:10.1002/jgra.50181.
2192 Sergeev, V. A., M. Malkov, and K. Mursula (1993), Testing the isotropic boundary
2193 algorithmm to evaluate the magnetic field configuration of the tail, *J. Geophys.*
2194 *Res., 98*, 7609.
2195 Shelley, E. G., R. G. Johnson, and R. D. Sharp (1972), Satellite observations of
2196 energetic heavy ions during a geomagnetic storm, *J. Geophys. Res., 77*, 6104.
2197 Shemansky, D. E., and A. L. Broadfoot (1977), Interaction of the surfaces of the
2198 Moon and Mercury with their exospheric atmospheres, *Rev. Geophys., 15*, 491–
2199 499, doi:10.1029/RG015i004p00491.
2200 Shiokawa, K., K. Yumoto, Y. Tanaka, T. Oguti, Y. Kiyama (1994), Low-latitude
2201 auroras observed at Moshiri and Rikubetsu (L=1.6) during magnetic storms on
2202 February 26, 27, 29, and May 10, 1992, *J. Geomag. Geoelec., 46*, 231–252.
2203 Simpson, J. A., J. H. Eraker, J. E. Lamport, and P. H. Walpole (1974), Electrons and
2204 protons accelerated in Mercury's magnetic field, *Science, 185*, 160–166.
2205 Siscoe, G. L., N. F. Ness, and C. M. Yeates (1975), Substorms on Mercury?, *J.*
2206 *Geophys. Res., 80*, 4359–4363, doi:10.1029/JA080i031p04359.
2207 Slavin, J. A., and R. E. Holzer (1979), The effect of erosion on the solar wind stand-
2208 off distance at Mercury, *J. Geophys. Res.*, *84*, 2076–2082.
2209 Slavin, J. A., M. F. Smith, E. L. Mazur, D. N. Baker, T. Iyemori, H. J. Singer, and E.
2210 W. Greenstadt (1992), ISEE-3 plasmoid and TCR observations during an extended
2211 interval of substorm activity, *Geophys. Res. Lett., 19*, 825–828.
2212 Slavin, J. A., M. F. Smith, E. L. Mazur, D. N. Baker, E. W. Hones, T. Iyemori, and E.
2213 W. Greenstadt (1993), ISEE-3 observations of traveling compression regions in the
2214 Earth's magnetotail, *J. Geophys. Res., 98*, 15,425–15,446.
2215 Slavin, J. A., R. P. Lepping, J. Gjerloev, D. H. Fairfield, M. Hesse, C. J. Owen, M. B.
2216 Moldwin, T. Nagai, A. Ieda, and T. Mukai (2003), Geotail observations of
2217 magnetic flux ropes in the plasma sheet, *J. Geophys. Res., 108*, 1015,
2218 doi:10.1029/2002JA009557.
2219 Slavin, J. A., E. I. Tanskanen, M. Hesse, C. J. Owen, M. W. Dunlop, S. Imber, E. A.
2220 Lucek, A. Balogh, and K.-H. Glassmeier (2005), Cluster observations of traveling
2221 compression regions in the near-tail, *J. Geophys. Res., 110*, A06207,
2222 doi:10.1029/2004JA010878.
2223 Slavin, J. A., R. P. Lepping, J. Gjerloev, D. H. Fairfield, M. Hesse, C. J. Owen, M. B.
2224 Moldwin, T. Nagai, A. Ieda, and T. Mukai (2007), MESSENGER: Exploring
2225 Mercury's magnetosphere, *Space Sci. Rev., 131*, 133–160.
2226 Slavin, J. A., et al. (2008), Mercury's magnetosphere after MESSENGER's first
2227 flyby, *Science, 321*, 85–89, doi:10.1126/science.1159040.
2228 Slavin, J. A., et al. (2009), MESSENGER observations of magnetic reconnection in
2229 Mercury's magnetosphere*, Science, 324,* 606–610.
2230 Slavin, J. A., et al. (2010), MESSENGER observations of extreme loading and
2231 unloading of Mercury's magnetic tail*, Science, 329,* 665–668.
2232 Slavin, J. A., et al. (2012a), MESSENGER and Mariner 10 flyby observations of
2233 magnetotail structure and dynamics at Mercury, *J. Geophys. Res., 117*, A01215,
2234 doi:10.1029/2011JA016900.

2235 Slavin, J. A., et al. (2012b), MESSENGER observations of a flux-transfer-event
2236 shower at Mercury, *J. Geophys. Res., 117*, A00M06, doi:10.1029/JA017926.
2237 Slavin, J. A., G. A. DiBraccio, D. J. Gershman, S. M. Imber, G. K. Poh, T. H.
2238 Zurbuchen, X. Jia, D. N. Baker, S. A. Boardsen, M. Sarantos, T. Sundberg, A.
2239 Masters, C. L. Johnson, R. M. Winslow, B. J. Anderson, H. Korth, R. L. McNutt
2240 Jr., and S. C. Solomon (2014), MESSENGER observations of Mercury's
2241 magnetosphere under extreme solar wind conditions, *J. Geophy. Res. Space*
2242 *Physics, 119*, 8087–8116, doi:10.1002/2014JA020319.
2243 Smith, M. F., and M. Lockwood (1996), Earth's magnetospheric cusps, *Rev.*
2244 *Geophys.*, *34*, 233–260, doi: 10.1029/96RG00893.
2245 Smith, D. E., et al. (2012), Gravity field and internal structure of Mercury from
2246 MESSENGER, *Science, 336*, 214–271, doi:10.1126/science.1218809.
2247 Smyth, W. H., and M. L. Marconi (1995), Theoretical overview and modeling of the
2248 sodium and potassium atmospheres of Mercury, *Astrophys. J., 441*, 839–864.
2249 Solomon, S. C., R. L., McNutt, R. E. Gold, and D. L. Domingue (2007),
2250 MESSENGER: Mission Overview, *Space Sci. Rev., 131*, 3–39.
2251 Speiser, T. W. (1965), Particle trajectory in model current sheets: 1. Analytical
2252 solutions, *J. Geophys. Res., 70*, 4219.
2253 Sprague, A. L., R. W. H. Kozlowski, D. M. Hunten, N. M., Schneider, D. L.
2254 Domingue, W. K. Wells, W. Schmitt, and U. Fink (1997), Distribution and
2255 abundance of sodium in Mercury's atmosphere, *Icarus, 129*, 506–527.
2256 Stern, S. A. (1999), The lunar atmosphere: history, status, current problems, and
2257 context, *Rev. Geophys., 37*, 453–491.
2258 Strangeway, R. J., C. T. Russell, J. G. Luhmann, T. E. Moore, J. C. Foster, S. V.
2259 Barabash, and H. Nilsson (2010), Does a planetary-scale magnetic field enhance or
2260 inhibit ionospheric plasma outflows? AGU Fall Meeting Abstracts, 1893.
2261 Suess, S. T., and B. E. Goldstein (1979), Compression of the Hermean magnetosphere
2262 by the solar wind, *J. Geophys. Res., 84*, 3306–3312.
2263 Sundberg, T., S. A. Boardsen, J. A. Slavin, L. G. Blomberg, and H. Korth (2010), The
2264 Kelvin-Helmholtz instability at Mercury: An assessment, *Planet. Space Sci., 58*,
2265 1434–1441, doi:10.1016/j.pss.2010.06.008.
2266 Sundberg, T., S. A. Boardsen, J. A. Slavin, L. G. Blomberg, J. A. Cumnock, S. C.
2267 Solomon, B. J. Anderson, and H. Korth (2011), Reconstruction of propagating
2268 Kelvin-Helmholtz vortices at Mercury's magnetopause, *Planet. Space Sci., 59*,
2269 2051–2057.
2270 Sundberg, T., S. A. Boardsen, J. A. Slavin, B. J. Anderson, H. Korth, T. H.
2271 Zurbuchen, J. M. Raines, and S. C. Solomon (2012), MESSENGER orbital
2272 observations of large-amplitude Kelvin-Helmholtz waves at Mercury's
2273 magnetopause, *J. Geophys. Res., 117*, A04216, doi:10.1029/2011JA017268.
2274 Trávníček, P., P. Hellinger, and D. Schriver (2007), Structure of Mercury's
2275 magnetosphere for different pressure of the solar wind: Three dimensional hybrid
2276 simulations, *Geophys. Res. Lett.*, *34*, 5104, doi: 10.1029/2006GL028518.
2277 Trávníček, P., et al. (2010), Mercury's magnetosphere-solar wind interaction for
2278 northward and southward interplanetary magnetic field: Hybrid simulation results,
2279 *Icarus*, *209*, doi: 10.1016/j.icarus.2010.01.008.
2280 Vervack, R. J., W. E. McClintock, R. M. Killen, A. L. Sprague, B. J. Anderson, M. H.
2281 Burger, E. T. Bradley, N. Mouawad, S. C. Solomon, and N. R. Izenberg (2010),
2282 Mercury's complex exosphere: Results from MESSENGER's third flyby, *Science,*
2283 *329*, 672–675, doi:10.1126/science.1188572.

Vervack, R. J., W. E. McClintock, R. M. Killen, A. L. Sprague, M. H. Burger, A. W. Merkel, and M. Sarantos (2011), MESSENGER searches for less abundant or weakly emitting species in Mercury's Exosphere, AGU Fall Meeting Abstracts A2.

Vilas, F., C. R. Chapman, and M. S. Mathews (1988), *Mercury*, Univ. Arizona Press, Tucson, AZ.

Wang, Y.-C., and W.-H. Ip (2011), Source dependency of exospheric sodium on Mercury, *Icarus, 216*, 387–402, doi:10.1016/j.icarus.2011.09.023.

Wang, Y.-C., J. Mueller, U. Motschmann, and W.-H. Ip (2010), A hybrid simulation of Mercury's magnetosphere for the MESSENGER encounters in year 2008, *Icarus, 209*, 10.1016/j.icarus.2010.05.020.

Wang, Y. X., F. Ohuchi, and P. H. Holloway (1984), Mechanisms of electron stimulated desorption from soda-silica glass surfaces, *J. Vac. Sci. Technol. A*, *2(2)*, 732–737, doi:10.1116/1.572560.

Winglee, R. M., E. Harnett, and A. Kidder (2009), Relative timing of substorm processes as derived from multifluid/multiscale simulations: Internally driven substorms, *J. Geophys. Res., 114*, A09213, doi:10.1029/2008JA013750.

Winslow, R. M., C. L. Johnson, B. J. Anderson, H. Korth, J. A. Slavin, M. E. Purucker, and S. C. Solomon (2012), Observations of Mercury's northern cusp region with MESSENGER's Magnetometer, *Geophys. Res. Lett.*, *39*, L08112, doi:10.1029/2012GL051472.

Winslow, R. M., B. J. Anderson, C. L. Johnson, J. A. Slavin, H. Korth, M. E. Purucker, D. N. Baker, and S. C. Solomon (2013), Mercury's magnetopause and bow shock from MESSENGER Magnetometer observations, *J. Geophys. Res., 118*, 2213–2227, doi:10.1002/jgra.50237.

Winslow, R. M., et al. (2014), Mercury's surface magnetic field determined from proton-reflection magnetometry, *Geophys. Res. Lett., 41*, 4463–4470, doi:10.1002/2014GL060258.

Wurz, P., and L. Blomberg (2001), Particle populations in Mercury's magnetosphere, *Planet. Space Sci., 49*, 1643–1653.

Wurz, P., and H. Lammer (2003), Monte-Carlo simulation of Mercury's exosphere, *Icarus, 164*, 1–13.

Wurz, P., J. A. Whitby, U. Rohner, J. A. Martín-Fernández, H. Lammer, and C. Kolb (2010), Self-consistent modelling of Mercury's exosphere by sputtering, micro-meteorite impact and photon-stimulated desorption, *Planet. Space Sci., 58*, 1599–1616.

Wurz, P., U. Rohner, J. A. Whitby, C. Kolb, H. Lammer, P. Dobnikar, and J. A. Martín-Fernández (2007), The Lunar exosphere: The sputtering contribution, *Icarus, 191*, 486–496, doi:10.1016/j.icarus.2007.04.034.

Yagi, M., K. Seki, Y. Matsumoto, D. C. Delcourt, and F. Leblanc (2010), Formation of a sodium ring in Mercury's magnetosphere, *Journ. Geophys. Res., 115*, A10, doi:10.1029/2009JA015226.

Yakshinksiy, B. V., and T. E. Madey (1999), Photon-stimulated desorption as a substantial source of sodium in the lunar atmosphere, *Nature, 400*, 642.

Yakshinskiy, B. V. and T. E. Madey (2005), Temperature-dependent DIET of alkalis from SiO_2 films: Comparison with a lunar sample, *Surf. Sci., 593*, 202–209.

Yakshinskiy, B. V., and T. E. Madey (2004), Photon-stimulated desorption of Na from a lunar sample: temperature-dependent effects, *Icarus, 168*, 53–59.

Yakshinskiy, B. V., T. E. Madey, and V. N. Ageev (2000), Thermal desorption of sodium atoms from thin SiO2 films, *Surf. Rev. Lett., 7*, 75–87.

2333 Yau, A. W., A. Howarth, W. K. Peterson, and T. Abe (2012), Transport of thermal-
2334 energy ionospheric oxygen (O^+) ions between the ionosphere and the plasma sheet
2335 and ring current at quiet times preceding magnetic storms, *J. Geophys. Res., 117*,
2336 doi:10.1029/2012JA017803.
2337 Zurbuchen, T. H., et al. (2011), MESSENGER observations of the spatial distribution
2338 of planetary ions near Mercury, *Science, 333*, 1862.
2339 Zurbuchen, T. H., J. M. Raines, G. Gloeckler, S. M. Krimigis, J. A. Slavin, P. L.
2340 Koehn, R. M. Killen, A. L. Sprague, R. L. McNutt Jr., and S. C. Solomon (2008),
2341 MESSENGER observations of the composition of Mercury's ionized exosphere
2342 and plasma environment, *Science, 321*, 90–92, doi:10.1126/science.1159314.
2343 Zwan, B. J., and R. A. Wolf (1976), Depletion of solar wind plasma near a planetary
2344 boundary, *J. Geophys. Res*., *81*, 1636–1648.